HZDR-073

FUNDAMENTALS OF ION-SOLID INTERACTION

A Compact Introduction

Wolfhard Möller

Wissenschaftlich-Technische Berichte
HZDR-073 · ISSN 2191-8708

WISSENSCHAFTLICH-
TECHNISCHE BERICHTE

HZDR
HELMHOLTZ
ZENTRUM DRESDEN
ROSSENDORF

Wissenschaftlich-Technische Berichte
HZDR-073

Wolfhard Möller

FUNDAMENTALS OF ION-SOLID INTERACTION

A Compact Introduction

HZDR

HELMHOLTZ
ZENTRUM DRESDEN
ROSSENDORF

Druckausgabe: ISSN 2191-8708

Elektronische Ausgabe: ISSN 2191-8716

https://www.hzdr.de/publications/Publ-24296

urn:nbn:de:bsz:d120-qucosa-214354

2017

Herausgegeben vom

Helmholtz-Zentrum Dresden - Rossendorf

Bautzner Landstraße 400

01328 Dresden

Germany

Fundamentals of Ion-Solid Interaction

A Compact Introduction

Wolfhard Möller

Institute of Ion Beam Physics and Materials Research
Helmholtz-Zentrum Dresden-Rossendorf

Contents

1 Introduction

Since Rutherford's[1] famous paper which first described the scattering of α–particles in matter, the field of ion-solid interaction has matured by now during one entire century. First theoretical concepts addressing particle penetration of solids were given by Thomson[2] and Bohr[3,4]. Quantum theory entered the field in treatments of ion stopping by Born[5] and Bethe[6]. Still on classical grounds, transport theory was first introduced in a paper on multiple scattering by Bothe[7]. The discovery of nuclear fission launched theoretical studies by Bohr[8,9] on the scattering and stopping of fission products. A further milestone in the understanding of particle penetration phenomena is the 1948 paper by Bohr[10]. On this basis, the theoretical understanding was enhanced in the early 1960's in particular by a series of papers by Lindhard[11-13]. Simultaneously, an increasing amount of experimental studies on ion stopping and scattering were launched in connection with the development of ion acceleration devices and corresponding equipment for particle detection. During this period, also first computer simulation studies came up[14,15] which later proved to be an utmost efficient tool for the description of collisional phenomena in ion-solid interaction. The relevance for numerous applications became evident, such as for the compositional and structural analysis of thin films and near-surface layers, for semiconductor technology, and nuclear fission and fusion technology. This caused increasing interest not only in the penetration and the scattering of the impinging ions, but also in the modification of the irradiated material due to ion implantation[16], radiation damage[17-19] and surface erosion by sputtering[20]. Consequently, ion-solid interaction established around 1970 internationally as a quickly expanding field at the intersection of solid-state physics and nuclear physics.

Numerous reviews and textbooks are available which cover the fundamentals of ion-solid interaction. Torrens[21] reviewed the knowledge about interatomic potentials as of 1972. An early lecture series by Sigmund[22-24] gives an overview of transport theory for ion ranges, radiation damage and sputtering. More recent books by the same author[25,26] review energy loss theory. Sputtering and related phenomena are extensively covered in a series of books edited by Behrisch et al.[27-30]. A textbook by Eckstein[31] focuses on the computer simulation of particle irradiation phenomena. This issue is also particularly addressed in a book edited by Smith[32]. A compact and comprehensive overview of most aspects of ion-solid interaction and their applications has been written by Nastasi et al.[33]. A recent collection of expert contributions edited by Sigmund[34,35] addresses in particular modern aspects of ion-surface interaction, such as involving very high ion energies with applications in biomedicine, and the ion-induced formation and control of nanostructures. For new topics of recent interest, a volume edited by Bernas[36] is also recommended.

In view of this broad and well-collected information, it cannot be the purpose of the present report to re-formulate the general fundamentals of ion-solid interactions or any special aspects in detail. In the context of the present short introduction, it is rather intended to provide a compact display of the essential knowledge which is valuable for any user of fast ion methods and technologies, for a convenient application of the most suitable formalisms and/or computer assistance.

The present report has been derived from a lecture given at Technische Universität Dresden and is based on textbook knowledge, individual publications and own work by the author before the year 2012. It concentrates on collisional fundamentals, addressing only short-time phenomena during the slowing down of the incident ions and the generated fast atoms of the target material, whereas thermal and chemical effects acting on longer time scales, such as post-irradiation diffusion and phase formation, are not included. Further, the manifold materials applications of ion irradiation and implantation with their often specific aspects are not covered, nor important more recent developments such as refinements in theory, applications to soft matter and biological tissue, specific aspects of the ion irradiation of nanostructures, the self-organisation of nanostructures under ion irradiation, the role of ion-surface interaction in thin film deposition, or the interaction of highly charged ions with solids.

Thus, the present report is conceived as a compact source of information which might be helpful in particular for students and newcomers using fast ion tools in research and application.

2 Binary elastic collisions

2.1 Classical treatment of binary collisions

Fast ions traversing a solid may collide with the atomic nuclei ("nuclear collisions") or the electrons ("electronic collisions") of the solid. Somewhat misleading, nuclear collisions are often called "elastic" although they might be accompanied by energy transfer in the system of electrons as we will see below, and electronic collisions are often called "inelastic" as they imply ionization or excitation events.

For both nuclear and electronic collisions, the most elementary approach is the binary elastic interaction of two point charges as sketched in Fig. 1. In the laboratory system (LS), a zero velocity of the target particle is assumed as any thermal velocity is small compared to the ion energy range of interest (» 1 eV). After the collision, the projectile and the recoil particle are characterized by asymptotic scattering angles Θ and Φ, respectively. As the collision does not affect the total momentum of the system, the kinematics are determined in the centre-of-mass system (CMS) with the deflection angle ϑ. In the CMS, the two-body system can be reduced to the kinematics of a single particle with the reduced mass

$$\mu = \frac{m_1 m_2}{m_1 + m_2} \tag{1}$$

where m_1 and m_2 denote the masses of the moving projectile and the target particle, respectively.

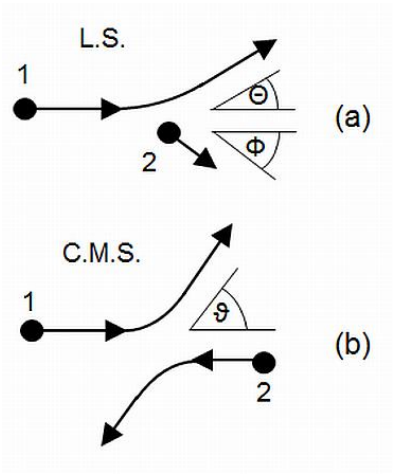

Fig. 1. Elastic scattering in the laboratory system (a) and the centre-of-mass system (b). The moving charged particle is indexed by 1, the target particle by 2

Momentum conservation leads to the transformation relations between the laboratory and CMS scattering angles

$$\tan\Theta = \frac{\sin\vartheta}{\frac{m_1}{m_2} + \cos\vartheta} \tag{2}$$

and

$$\Phi = \frac{\pi - \vartheta}{2} \tag{3}$$

and the reverse transformation

$$\vartheta = \Theta + \arcsin\left(\frac{m_1}{m_2}\sin\Theta\right) \tag{4}$$

The relative kinetic energy which is conserved in the CMS system is given by

$$E_c = \frac{m_2}{m_1 + m_2} E \tag{5}$$

where E denotes the LS kinetic energy of the projectile. The LS energy being transferred to the target ("recoil") particle is given by

$$T = \gamma E \sin^2 \frac{\vartheta}{2} \tag{6}$$

with the energy transfer factor

$$\gamma = \frac{4 m_1 m_2}{(m_1 + m_2)^2} \tag{7}$$

From this, the LS energy of the projectile after the collision results as

$$E' = E - T = E\left(1 - \gamma \sin^2 \frac{\vartheta}{2}\right) \tag{8}$$

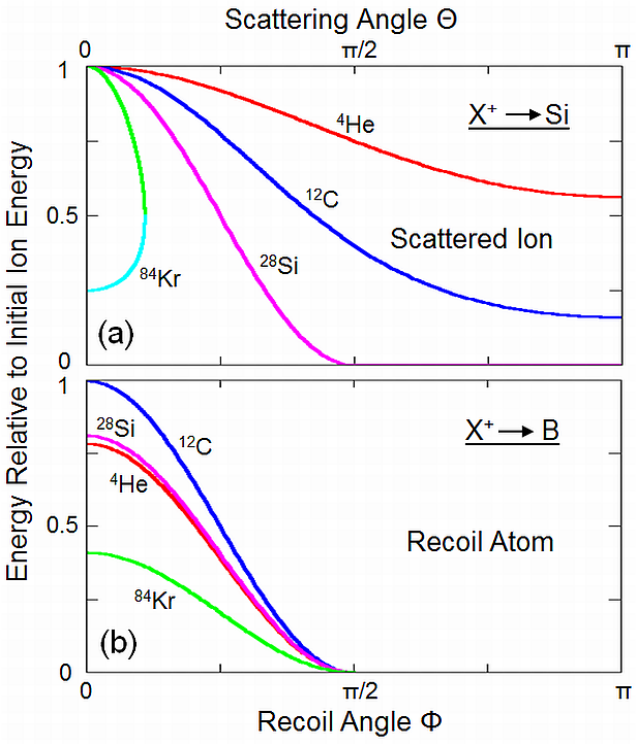

Fig. 2. Energies of the collision partners versus the scattering angles in the laboratory system after binary elastic collision events with different species of projectiles, for projectiles scattered from a silicon atom (a) and for boron recoil atoms (b)

or after transformation into the LS as

$$E' = \left(\frac{m_1}{m_1 + m_2}\right)^2 E\left(\cos\Theta \pm \sqrt{\left(\frac{m_2}{m_1}\right)^2 - \sin^2\Theta}\right)^2 \tag{9}$$

Eqs. (4) and (9) indicate the existence of a maximum LS scattering angle in case of $m_1 \geq m_2$. In this case, both signs are valid in eq. (9), and two different LS energies exist for any permitted LS scattering angle. Fig. 2 shows the relative energies of the scattered ion and the recoil atoms for collisions of different ions with a silicon atom and a boron atom, respectively.

As indicated in Fig. 3 for a classical scattering trajectory in the CMS system, the scattering angle decreases at increasing impact parameter p. The corresponding relation is represented by the so-called "classical trajectory integral"

$$\vartheta = \pi - 2p\int_0^{R_{min}^{-1}} \frac{d\left(\frac{1}{R}\right)}{\sqrt{1 - \frac{V(R)}{E_c} - \frac{p^2}{R^2}}} \tag{10}$$

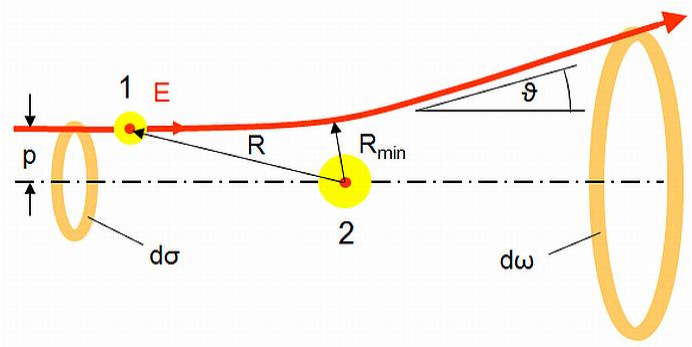

Fig. 3. Classical scattering trajectory and the definition of the differential scattering cross section (see text for explanation)

for any spherically symmetric interaction potential $V(R)$ which depends on the distance of the collision partners R. The root of the denominator determines the minimum distance of approach, R_{min}. Projectiles which enter an annulus of differential area dσare scattered into a differential solid angle $d\omega$ (see Fig. 3), from which, at known $\vartheta(p)$ relation, the differential cross section of the scattering process is given by

$$\frac{d\sigma}{d\omega} = \left|\frac{2\pi p dp}{2\pi \sin\vartheta d\vartheta}\right| = \frac{p}{\sin\vartheta}\frac{dp}{d\vartheta} \tag{11}$$

The differential cross section in the laboratory system is obtained by transformation according to eq. (4) as

$$\frac{d\sigma}{d\Omega} = \frac{d\sigma}{d\omega}\frac{\left(\left(\frac{m_1}{m_2} + \cos\vartheta\right)^2 + \sin^2\vartheta\right)^{\frac{3}{2}}}{1 + \frac{m_1}{m_2}\cos\vartheta} \tag{12}$$

As an example, we choose the Coulomb interaction potential between two charged particles with the charge numbers Q_1 and Q_2, which is given by (e and ε_0 denoting the elementary charge and the vacuum electric permittivity, respectively)

$$V(R) = \frac{Q_1 Q_2 e^2}{4\pi\varepsilon_0 R} \tag{13}$$

for the evaluation of the trajectory integral (eq.(10)), which yields

$$\tan\frac{\vartheta}{2} = \frac{b}{2p} \tag{14}$$

with the so-called "collision diameter"

$$b = \frac{Q_1 Q_2 e^2}{4\pi\varepsilon_0 E_c} \tag{15}$$

which represents the distance of minimum approach during a central collision of particles of equal polarity. Combining eqs. (11), (14) and (15) yields the Rutherford scattering cross section

$$\left(\frac{d\sigma}{d\omega}\right)_R = \frac{1}{16}\left(\frac{Q_1 Q_2 e^2}{4\pi\varepsilon_0}\right)^2 \frac{1}{E_c^2} \frac{1}{\sin^4\frac{\vartheta}{2}} \tag{16}$$

which scales with the inverse square of the projectile energy and decreases strongly towards backscattering angles.

Already the cylindrical symmetry of the scattering problem (see Fig. 3) strongly favours larger impact parameters and thereby smaller scattering angles. In case of Rutherford scattering, this is even strongly enhanced by the angular dependence of the cross sections. Thus, when considering a beam of projectiles, the vast amount of collisions will scatter into forward angles. Consequently, it is helpful to look for a low-angle simplification of the scattering formalism. This can be achieved using the so-called "momentum" approximation[11], in which the small-angle trajectory of the projectile is approximated by a straight line (see Fig. 4). During the scattering event, the projectile moving along the z direction experiences a force pulse, the time integral of which leads to a small momentum transfer Δp_y in y direction. The resulting scattering angle (in the CMS) is then given by the ratio of the transverse and longitudinal momenta, with the decrease of the latter being neglected due to the small energy transfer at low scattering angle.

$$\vartheta = \frac{\Delta p_y}{\sqrt{2\mu E_c}} = -\frac{1}{2E_c}\int_{-\infty}^{+\infty} \frac{\partial}{\partial p} V\left(\sqrt{z^2 + p^2}\right) dz \tag{17}$$

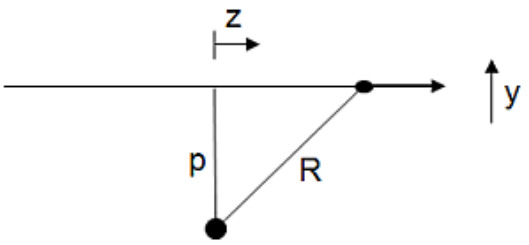

Fig. 4. Binary collision at small scattering angles in the momentum approximation

Eq. (2) reads in low-angle approximation

$$\Theta = \frac{m_2}{m_1 + m_2}\vartheta \tag{18}$$

from which a simple scattering formula is obtained according to

$$\Theta = -\frac{1}{2E}\int_{-\infty}^{+\infty}\frac{\partial}{\partial p}V\left(\sqrt{z^2 + p^2}\right)dz \tag{19}$$

Eq. (19) is directly valid in the LS so that the above CMS-LS transformations become obsolete. Thereby, in particular the treatment of sequential and multiple scattering phenomena becomes considerable simplified. For the Coulomb potential, eq. (19) yields in consistence with the low-angle approximation of eq. (14)

$$\vartheta = \frac{b}{p} \tag{20}$$

2.2 Validity of the classical treatment

For a Coulomb potential, Bohr[10] has given a simple criterion for the validity range of the classical trajectory model according to the condition

$$\kappa = \frac{2|Q_1 Q_2|e^2}{4\pi\varepsilon_0\hbar\upsilon} = 2|Q_1 Q_2|\frac{\upsilon_0}{\upsilon} > 1 \tag{21}$$

where $\hbar$ denotes Planck's constant, υ the projectile velocity and υ_0 the electron velocity of the first Bohr orbit. At the first glance, the criterion (21) is in contrast to general perception. For the scattering of wave packets at objects, a classical beam treatment is feasible when the wavelength is small compared to the size of the object, i.e. in the limit of large projectile velocity. However, for the present case of atomic collisions, the collision diameter may be regarded as the object size, which scales with $1/\upsilon^2$, thus inverting the velocity dependence of the criterion for classical treatment.

It should be noted that eq. (21) neglects atomic screening (see sect. 3). Further, the charge number of an ion moving in a solid is not necessarily equal to its atomic number (see subsection 4.3.1). Thus, only rough estimates can be expected when evaluating eq. (21) with the atomic numbers of the collision partners. Doing so, nuclear collisions between moving ions and atomic nuclei in a solid can be treated classically up to energies between ~100 keV/amu and many GeV/amu for the lightest and heaviest combinations of collision partner, respectively, which entirely covers the parameter range of ion beam technology applications. However, quantum-mechanical treatment becomes often necessary for collisions with electrons, with a lower energy limit between 100 keV/amu for hydrogen ions and several 100 MeV/amu for very heavy ions.

2.3 Quantum-mechanical scattering

In the quantum-mechanical picture, the scattering of a plane matter wave representing the projectile is described by the transition of the scattering system from an initial state $|i\rangle$ to a final state $|f\rangle$. In first Born approximation, the differential cross section reads

$$\frac{d\sigma_{if}}{d\omega} = \mu^2\left(\frac{2\pi}{\hbar}\right)^4 \frac{\upsilon_f}{\upsilon_i}\left|\langle f|V|i\rangle\right|^2 \tag{22}$$

where υ_i and υ_f denote the velocities of the ingoing and outgoing matter waves, respectively. For elastic scattering in a spherically symmetric potential, the result becomes

$$\frac{d\sigma}{d\omega} = \frac{\mu^2 \lambda\!\!\!^{-2}}{\hbar^4}\frac{1}{\sin^2\frac{\vartheta}{2}}\left|\int_0^\infty V(R)\sin\left(\frac{2}{\lambda\!\!\!^{-}}R\sin\frac{\vartheta}{2}\right)RdR\right|^2 \tag{23}$$

with $\lambda\!\!\!^{-} = \hbar/(m_1\upsilon)$ denoting the matter wavelength of the projectile divided by 2π.

3 Nuclear interaction in a screened Coulomb potential

So far, we have treated the interaction of point charges associated with a pure Coulomb potential. This is only valid at sufficiently high velocities and low impact parameters, when the moving ion is deprived of all its electrons (see subsection 4.3.1) and penetrates the cloud of the target electrons before it is scattered by the nucleus. In the general case of ion scattering at atomic nuclei, the screening of the Coulomb potential by the electrons of both the ion and the target atom has to be taken into account. As the electron systems will be dynamically altered along the trajectory during scattering, a full quantum-mechanical treatment would be extremely laborious. Therefore, the treatment of energetic atomic collision has been largely based on statistical models.

3.1 Statistical models of the atom

Before turning to the interaction of two atoms, we will first consider the statistical description[37-39] of a single atom with atomic number *Z*. A spherically symmetric screened Coulomb potential resulting from the statistical model of the atom is conveniently written as

$$V(r) = \frac{Ze^2}{4\pi\varepsilon_0 r}\varphi\left(\frac{r}{a}\right) \tag{24}$$

where *r* is the radial distance from the atomic nucleus, *a* a screening parameter and φ a screening function which describes the deviation from the Coulomb potential. Consequently, $\varphi(r=0)=1$ holds at the position of the nucleus, and $\varphi(r\to\infty)=\varphi'(r\to\infty)=0$ at large distances, where the charge of the nucleus is fully screened.

The Thomas-Fermi [37,38] potential of the atom is based on quantum statistics of the electrons, from which a relation between the local electron density, $n_e(r)$, and the electrostatic potential $\phi(r)$ is established by a variation calculus which minimizes the sum of kinetic and potential energy. On the other hand, n_e and ϕ have to self-consistently fulfill the electrostatic Poisson equation. From this procedure, the Thomas-Fermi screening function results as numerical solution of the differential equation

$$\frac{d^2\varphi_{TF}(\xi)}{d\xi^2} = \frac{\varphi_{TF}(\xi)^{\frac{3}{2}}}{\sqrt{\xi}} \tag{25}$$

with the above boundary conditions, and the screening radius as

$$a_{TF} = 0.8853 \frac{a_0}{Z^{1/3}} \tag{26}$$

with a_0 denoting the radius of the first Bohr orbit in the hydrogen atom. The screening function is often approximated by a sum of exponentials. For the Thomas-Fermi function, an example is the Molière[40] function according to

$$\varphi_M(\xi) = 0.35e^{-0.3\xi} + 0.55e^{-0.2\xi} + 0.1e^{-6\xi} \tag{27}$$

with $\xi = r/a$. Eq. (27) holds with good precision for $0 \le \xi \le 5$. According to eq. (26), the screening distance is normally in the order of 10^{-2} nm, so that eq. (27) is only valid for the inner volume of an atom in a solid, with a typical radius of about 0.3 nm.

Using a different calculus for the energy minimization in the statistical model of the atom, Lenz[41] and Jensen[42] arrived at an alternative screening function, given by

$$\varphi_{LJ}(\xi) = \left(1 + \xi + 0.3344\xi^2 + 0.0485\xi^3 + 0.002647\xi^4\right)e^{-\xi} \tag{28}$$

with $\xi = \sqrt{9.67\, r/a}$.

3.2 Interatomic potentials

At known potentials of the individual atoms, the interaction potential of the two-atom system can be obtained in an approximate way by a linear superposition of the electronic densities of the individual atoms[41,42], which neglects any distortion of the electronic systems during the interaction. Statistical approximations of quantum-mechanical correlation and exchange in the electronic system can be included. Numerical solutions for each individual ion-target combination are required.

Alternatively and with the aim to produce a simple universal diatomic potential, which approximately describes all ion-target combinations, Lindhard et al.[11] have chosen the so-called "similarity" approach. The screened Coulomb potential formalism of the individual atom is transferred to the interaction of two atoms via

$$V(R) = \frac{Z_1 Z_2 e^2}{4\pi\varepsilon_0 R} \varphi\left(\frac{R}{a}\right) \tag{29}$$

where *R* denotes the internuclear distance as in sect. 1, Z_1 and Z_2 the atomic numbers of the collision partners, and *a* the screening radius with the ansatz (corresponding to the Thomas-Fermi potential)

$$a_L = 0.8853 \frac{a_0}{\sqrt{Z_1^{2/3} + Z_2^{2/3}}} \tag{30}$$

It is obvious that this potential is a good approximation when the atomic numbers of the collision partners are widely different, $Z_1 \ll Z_2$ or vice versa, as it approaches the interaction of a heavy atom and a point charge, which is described by the single-atom potential, eqs. (24) and (26). For the other extreme, $Z_1 = Z_2$, the authors performed selected individual numerical calculations using the linear superposition of electronic densities as mentioned above, and found the results being in reasonable agreement with eqs. (29) and (30), with deviations in the 10% regime only.

In a more rigorous treatment of the diatomic interaction, Firsov[43,44] also found eq. (29) to be a good universal approximation. However, the screening radius was chosen as

$$a_F = 0.8853 \frac{a_0}{\left(\sqrt{Z_1} + \sqrt{Z_2}\right)^{2/3}} \tag{31}$$

Within the screened Coulomb formalism, a better confidence in a universal potential has been achieved by performing a larger variety of individual numerical calculations based on the superposition principle, and fitting an appropriate screening function to the results. Rather than from the above statistical models, results from full quantum-mechanical calculations were inserted for the atomic electron densities[45], including solid-state charge distributions[46]. The presently widely accepted average interatomic potential for the interaction of fast atoms with solids, has been derived from such numerical calculations for 522 ion-target combinations. The resulting so-called "universal" potential by Ziegler, Biersack and Littmark[47], which will be denoted as "ZBL" potential in the following, is given by the screening function

$$\begin{aligned} \varphi_U(\xi) = 0.1818\, e^{-3.2\xi} + 0.5099\, e^{-0.9423\xi} \\ + 0.2802\, e^{-0.4028\xi} + 0.02817\, e^{-0.2016\xi} \end{aligned} \tag{32}$$

with the normalized internuclear distance $\xi = R/a_U$ and the screening radius

$$a_U = 0.8853 \frac{a_0}{Z_1^{0.23} + Z_2^{0.23}} \tag{33}$$

Fig. 5 compares the different screening functions addressed above, and demonstrates the excellent fit of the ZBL potential to the results of the individual calculations involving quantum-mechanical atomic charge distributions. The maximum reduced radius of 3 corresponds to a typical atomic diameter in a solid. Thus, the Thomas-Fermi function would introduce significant errors in particular for low-angle scattering.

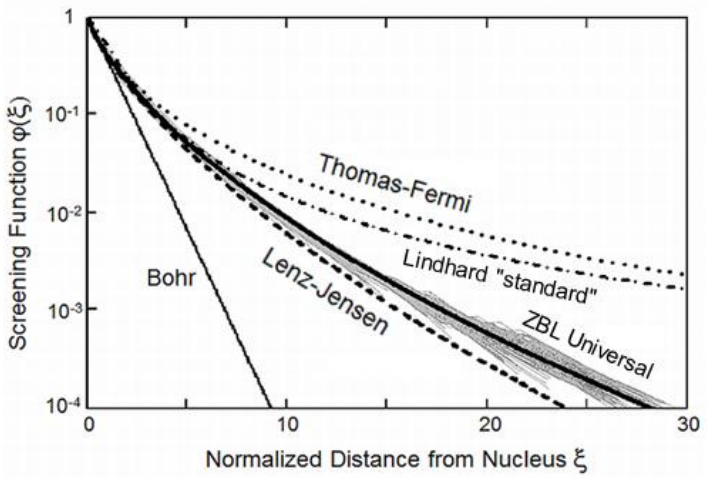

Fig. 5. Screening functions vs. internuclear distance according to eqs. (25), (28), (32) and (35). The Bohr screening function is the single exponential $\exp(-\xi)$. The shaded area indicates individual results from 522 ion-target combination which form the basis for the "universal" potential (see text). (After ref.[47])

For completeness, two additional approximate screening functions shall be mentioned which have employed for simplified treatments in binary collision theory. The power law approximation [11]

$$\varphi_U(\xi) = \frac{k_s}{s}\, \xi^{1-s} \tag{34}$$

corresponds to $V(R) \propto R^{-s}$. The parameters *s* and k_s can be obtained from fitting to any, e.g. of the above, screening functions in a certain range of the normalized screening radius, with variations from $s \approx 1$ to $s \approx 5$ in the overall range of interest.

Mainly for use in connection with ion channeling (see sect. 5), Lindhard[48] has introduced the so-called "standard" potential

$$\varphi_S(\xi) = 1 - \frac{\xi}{\sqrt{\xi^2 + 3}} \tag{35}$$

which is a reasonable approximation to the Thomas-Fermi screening function in particular for larger impact parameters.

3.3 Scattering Cross Section

For any of the above interatomic potentials, the differential scattering cross section can now be obtained using eq. (10). For the calculation of an approximate universal scattering function, Lindhard et al.[11] made use of the low-angle momentum approximation (see sect. 2.1). For a screened Coulomb potential, eq. (17) can be analytically evaluated with the result

$$\vartheta = \frac{b}{p} g\left(\frac{p}{a}\right) \tag{36}$$

with the function *g* to be calculated for any given screening function φ as

$$g(\xi) = \int_0^{\pi/2} \cos\eta \left[\varphi\left(\frac{\xi}{\cos\eta}\right) - \frac{\xi}{\cos\eta} \varphi'\left(\frac{\xi}{\cos\eta}\right) \right] d\eta \tag{37}$$

A convenient dimensionless "reduced" energy is introduced according to

$$\varepsilon = \frac{a}{b} = \frac{4\pi\varepsilon_0 a}{Z_1 Z_2 e^2} E_c = \frac{4\pi\varepsilon_0 a}{Z_1 Z_2 e^2} \frac{m_2}{m_1 + m_2} E \tag{38}$$

According to eq. (36),

$$\varepsilon \cdot \vartheta = \frac{a}{p} g\left(\frac{p}{a}\right) \tag{39}$$

so that the product of reduced energy and scattering angle depends only on a normalized impact parameter. Further, it varies significantly less than the individual variables ε and ϑ since, at given impact parameter, the scattering angle decreases at increasing energy. In this view, the low-angle approximation is extrapolated to larger scattering angles via

$$\varepsilon \cdot \vartheta \Rightarrow 2\varepsilon \sin\frac{\vartheta}{2} \tag{40}$$

The wide-angle extrapolation works surprisingly well. Compared to numerical integration of the trajectory integral, eq. (10), typical deviations are in the order of 10% or less. Defining now a reduced scattering variable

$$t^{1/2} = \varepsilon \sin\frac{\vartheta}{2} \tag{41}$$

and combining with eqs. (39) and (40), the impact parameter *p(t)* can be calculated numerically as the inverse function, from which the differential scattering cross section $d\sigma = d(\pi p^2)$ is obtained. Lindhard et al.[11] write the result as

$$\frac{d\sigma}{dt} = \pi a^2 \frac{f\left(t^{1/2}\right)}{2t^{3/2}} \tag{42}$$

The universal scattering function *f* can be evaluated for any given screening function. With $\varphi = 1$, the result becomes for the pure Coulomb potential

$$f_R\left(t^{1/2}\right) = \frac{1}{2t^{1/2}} \tag{43}$$

Using eq. (41), the reduced scattering variable *t* can be transformed into the scattering angle, from which the differential cross section in non-reduced units is obtained according to eq. (42). Inserting eq. (43) reproduces exactly the Rutherford cross section of eq. (16). This demonstrates that the large-angle extrapolation of eq. (40) is exactly valid for all angles in the limit of high energy.

In the power-law approximation (see eq. (34)), the universal scattering function results as

$$f_s\left(t^{1/2}\right) = \lambda_s t^{1/2-1/s} \tag{44}$$

with

$$\lambda_s = \frac{2}{s}\left(\frac{k_s \gamma_s}{2}\right)^{2/s} \tag{45}$$

and

$$\gamma_s = \frac{1}{2} B\left(\frac{1}{2}, \frac{s+1}{2}\right) \tag{46}$$

with *B* denoting the beta function.

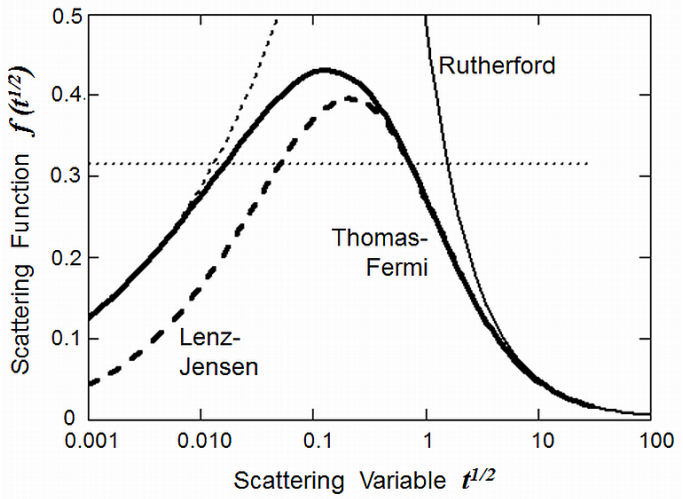

Fig. 6. Lindhard's scattering function (see eq. (42)) versus the reduced scattering variable (eq. (41)) for different interatomic potentials, including a power-law approximation to the interatomic potential (see eq. (34); thin dotted line) with s = 2 and k_s = 0.8. The thin dashed line represents a low-energy power-law fit according to $f\left(t^{1/2}\right) = 1.43\left(t^{1/2}\right)^{0.35}$

Fig. 6 compares the universal scattering functions for different interaction potentials. Above $t^{1/2} \approx 10$, screening can be neglected and Rutherford scattering becomes valid. The power-law approximation with $s = 2$ results in a constant scattering function, with yielding a rough estimate for medium scattering variables. For better Winterbon et al.[49] recommend $s = 3; 2; 1$ in the reduced energy ranges $\varepsilon \le 0.2$; $0.08 \le \varepsilon \le 2$; $\varepsilon \ge 10$, respectively, with respective parameters $\lambda_s = 1.309; 0.327; 0.5$ for Thomas-Fermi screening.

Still for the power-law approximation, the transformation of eq. (44) via eqs. (6) and (41) yields

$$\frac{d\sigma(E)}{dT} = C_s \frac{1}{E^{1/s} T^{1+1/s}} \tag{47}$$

with the constant

$$C_s = \frac{\pi}{2} \lambda_s a_L^2 \left(\frac{2 Z_1 Z_2 e^2}{4\pi\varepsilon_0 a_L} \right)^{2/s} \left(\frac{m_1}{m_2} \right)^{1/s} \tag{48}$$

A comparison of scattering cross sections with experimental data is shown in Fig. 7[50]. As for the individually calculated screening functions (see Fig. 5), both the more rigorously calculated values and the experimental data fall between the universal Thomas-Fermi and Lenz-Jensen predictions. The data obtained with quantum-mechanical atomic electron densities show characteristic oscillations, which are attributed to atomic shell effects. The amplitude of these "shell" oscillations, however, appears to be largely underestimated in comparison to the experimental data, and the phases are in disagreement for the low scattering variables. In the maxima of the shell oscillations, the experimental cross sections are larger than the theoretical ones by up to about 30% for the ion-target combination of Fig. 7. The ZBL potential (see eqs. (32) and (33)) has been obtained on similar grounds as the present '2 DHFS' predictions, but additionally averages over shell effects for the different ion-target combinations. Thus, similar errors might be expected as observed here, when deriving scattering cross section from the ZBL potential according to the classical trajectory integral as it is presently mostly practiced.

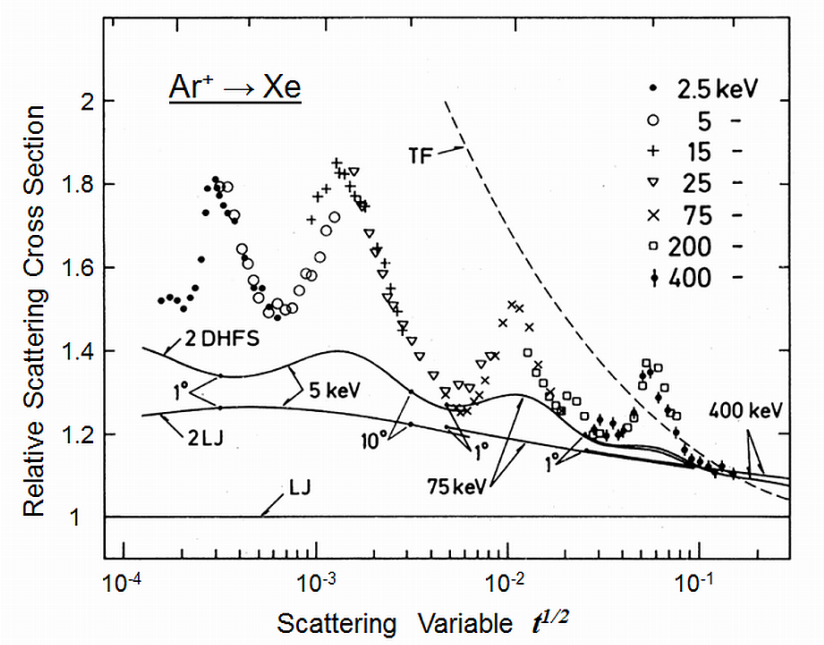

Fig. 7. Scattering cross section relative to the prediction of the universal scattering formula, eq. (42), being evaluated for the Lenz-Jensen potential. The corresponding result for the Thomas-Fermi potential is denoted by 'TF'. The '2 LJ' curves result from numerical evaluations of eq. (10) with a statistical interatomic potential obtained from the superposition of two Lenz-Jensen atoms, whereas the '2 DHFS' curves have similarly been calculated from two superimposed quantum-mechanical electron density distributions. Both have been evaluated for different energies, corresponding to the experimental conditions. Experimental results are represented by the different point symbols. (after ref.[50])

4 Ion Stopping

4.1 General definitions

For any fast particle traversing matter at an energy E, the stopping force[1] is defined as the energy loss per pathlength s according to

$$B(E) = -\frac{dE}{ds} \tag{49}$$

As the areal density of target atoms within the traversed sheet of matter determines the energy loss rather than the thickness itself, it is adequate to define the so-called stopping cross section as

$$S(E) = -\frac{dE}{nds} \tag{50}$$

where n denotes the atomic density of the material.

Stopping is a statistical process involving collisions with electrons and atomic cores. The differential probability per unit pathlength for a collision with an energy transfer T is given by $dp(T) = nd\sigma(T)$, corresponding to an energy loss $nTd\sigma(T)$ of the ion. Integration over all possible energy transfers yields the general expression

$$S(E) = \int T d\sigma(E,T) \tag{51}$$

In the description of ion stopping, it is common to separate the stopping due to the interaction with electrons from the stopping due to the scattering in the screened Coulomb field of the nuclei according to

$$S(E) = S_e(E) + S_n(E) \tag{52}$$

where S_e and S_n represent the "electronic" and the "nuclear" stopping cross section, respectively. A priori, the simple linear superposition of eq. (52) is not obvious. Correlations between electronic and nuclear collisions must be anticipated in particular at lower impact parameters. According to the Pauli principle, the electronic system of the "quasimolecule" rearranges when the nuclei approach each other to inner-shell distances, so that energy will be transferred without a direct collision with an electron. However, lower impact parameters occur relatively rarely as discussed above. On the other hand, distant collisions are characterized by the interaction with outer shell or Fermi gas electrons, where the nuclear interaction becomes small due to atomic screening. Although these considerations are in favor of the separation ansatz, the final justification will be given by the results to be shown later (see sect. 4.4), in particular by the dependence of S_e and S_n on the ion energy.

4.2 Nuclear Stopping

Nuclear stopping results from the energy transfers during binary elastic collisions as described in sect. 3. It can be conveniently described by means of the Lindhard universal scattering formal-

[1] Formerly, the stopping force has been denoted as "stopping power", which is dimensionally incorrect (see ref.[51]).

ism (see sect. 3.3), if, in addition to the reduced energy according to eq. (38), a reduced path-length is introduced as[12]

$$\rho = \pi a^2 n \gamma \cdot s \tag{53}$$

where γ is the energy transfer factor of eq. (7). With the definitions of sect. 3.3 and eq. (6), eq. (51) leads directly to the result[12]

$$\left(-\frac{d\varepsilon}{d\rho}\right)_n = \frac{1}{\varepsilon}\int_0^{\varepsilon} f\left(t^{1/2}\right) dt^{1/2} \tag{54}$$

For the results of the numerical evaluation, different fitting formulas have been given by different authors, such as by Matsunami et al.[52] for Thomas-Fermi screening according to

$$\left(-\frac{d\varepsilon}{d\rho}\right)_n = \frac{3.441\sqrt{\varepsilon}\ln(\varepsilon+2.718)}{1+6.355\sqrt{\varepsilon}+\varepsilon\left(6.882\sqrt{\varepsilon}-1.708\right)} \tag{55}$$

and by Ziegler et al.[47] for the ZBL potential according to

$$\left(-\frac{d\varepsilon}{d\rho}\right)_n = \frac{0.5\ln(1+1.2288\varepsilon)}{\varepsilon+0.1728\sqrt{\varepsilon}+0.0008\,\varepsilon^{0.1504}} \tag{56}$$

As seen from Fig. 8, the differences for the different screening functions are small due to the integration over the scattering function.

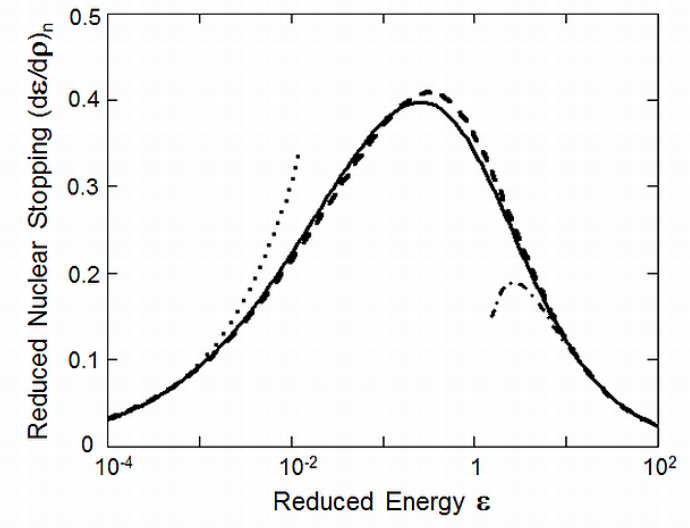

Fig. 8. Universal energy dependence of nuclear stopping in terms of reduced energy and pathlength, from fit formulas according to Matsunami et al.[52] (dashed line) and Ziegler et al.[47] (solid line) (see eqs. (53) and (54), respectively). Low-energy (dotted line) and high-energy (dashed-dotted line) approximations are given by $3.02\sqrt{\varepsilon}$ and $0.515\,ln(\varepsilon)/\varepsilon$, respectively

In the power-law approximation, the integration of eq. (51) with $T_{max} = \gamma E$ as upper integration limit yields

$$S_n(E) = \frac{C_s \gamma^{1-1/s}}{1-1/s} E^{1-2/s} \tag{57}$$

Extracting only the dependence on the ion energy and the ion and target masses using eq. (48), we obtain

$$S_n(E) \propto m_2^{1-2/s}\left(\frac{m_1}{m_1+m_2}\right)^{2-2/s}\left(\frac{E}{m_1}\right)^{1-2/s} \tag{58}$$

The middle term is independent on m_1 at sufficiently high energy with $s \to 1$ (see sect. 3.3), and also for $m_1 \approx m_2$ as well as for $m_1 >> m_2$. In these cases and for a given target material, nuclear stopping depends on the velocity of the projectile.

4.3 Electronic Stopping

4.3.1 Charge State of an Ion Moving in a Solid

Through a variety of atomic processes, the interaction of the electronic systems of the moving ion and the target atoms may result in a transfer of electrons from or to the ion. There have been numerous treatments of these charge exchange phenomena (see, e.g. refs.[9,10,53-57]). Here, we will only mention the most simple concepts as well as recipes for practical use.

The charge exchange leads to fluctuations of the charge state of an individual ion during its passage through matter. When entering the surface, the actual mean or "effective" charge at a given energy, Z_1^{eff}, is typically established within a few nm as a balance between average electron capture and loss. In a simple statistical picture, electron capture is efficient if there is sufficient time for the target electrons to accommodate to the electron system of the ion. Assuming the target electrons to be at rest in the LS, their velocity relative to the ion is equal to the ion velocity. Then, a so-called "adiabatic" transition can take place provided the ion velocity is smaller than the average velocity of the electrons in the atomic system of the ion. In the statistical model of the atom, the latter is given by $\upsilon_0 Z_1^{2/3}$. Consequently, Bohr[10] has written the effective charge as

$$Z_1^{eff} \approx Z_1 \frac{\upsilon}{\upsilon_0 Z_1^{2/3}} = \frac{\upsilon}{\upsilon_0} Z_1^{1/3} \tag{59}$$

At higher ion velocity, electron loss by collisions with the target electrons dominates, so that in the limit of high energy the ion will be deprived of all electrons. For a simple estimate for all velocities, eq. (59) can then be extrapolated according to

$$Z_1^{eff} = Z_1 \left(1 - \exp\left(-\frac{\upsilon}{\upsilon_0} Z_1^{-2/3} \right) \right) \tag{60}$$

Both experimental and more elaborate theoretical studies have broadly confirmed that the effective charge is determined by the ion velocity, but also an additional dependence on the target electron density. For practical use, different semi-empirical fit formulas have been proposed, cf. refs.[58-60], which allow a predictions of the effective charge with a precision down to a few %.

4.3.2 Low-Velocity Electronic Stopping

In the limit of low ion velocity at $\upsilon << \upsilon_0 Z_1^{2/3}$, the ion moving in the solid approaches a neutral atom (see eq. (60)). Following the picture given by Fermi and Teller[61] for $\upsilon << \upsilon_f$, where υ_f denotes the Fermi velocity

$$\upsilon_f = \frac{\hbar}{m_e} \left(3\pi^2 n_e \right)^{1/3} \tag{61}$$

(m_e denoting the mass of the electron), the ion is slowed down by momentum transfer due to scattering at the target electrons. In the frame of the moving ion as indicated in Fig. 9, only scat-

tering processes with a final momentum outside the target Fermi sphere are allowed since the Fermi sphere is completely occupied. The corresponding velocity space volume is approximately $4\pi v_f^2 v$. The density of contributing electrons with a velocity close to the Fermi velocity is $n_e' \approx 3n_e v/v_f$. As the electrons impinge the ion from the forward half space, the gas-kinetic expression $j_e' = n_e' v_f/4$ is roughly appropriate for the effective electron flux "seen" by the ion. In accordance with the definition of the stopping force (see sect. 4.1), the stopping cross section can be written as

$$S_e = -\frac{1}{n}\frac{dp}{dt} = \frac{1}{n}\dot{R}_s \Delta p \tag{62}$$

where p denotes the momentum of the ion, $\dot{R}_s$ the number of scattering events per unit of time, and Δp the average momentum transfer per scattering event. The latter can be approximated by $\Delta p \approx m_e v_f$ which is half of the maximum momentum transfer. With $\dot{R}_s = \sigma j_e'$ for a scattering cross section σ and $n_e = nZ_2$, putting everything together results in

$$S_e(v) \approx m_e Z_2 v v_f \sigma(v_f) \tag{63}$$

with the important result that low-energy electronic stopping is proportional to the ion velocity.

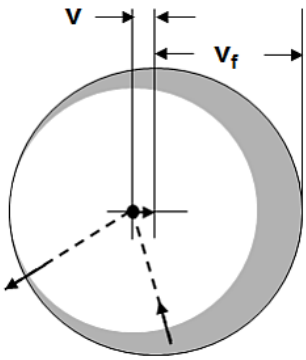

Fig. 9. Scattering of an electron from the Fermi sphere of the target electron gas at an ion moving at a velocity v being small compared to the Fermi velocity v_f. The outer circle denotes the target Fermi sphere, which is slightly shifted with respect to the moving ion. Only scattering events are allowed with a final state outside the Fermi sphere, i.e. for electrons originating from the shaded volume, as indicated by the dashed trajectory of a representative electron

A more rigorous treatment of the scattering geometry shows that eq. (63) holds exactly if the so-called "transport" cross section

$$\sigma_{tr}(v) = \int_0^{\pi} (1-\cos\vartheta)\frac{d\sigma}{d\omega}(v)\, d\omega \tag{64}$$

is inserted. The evaluation of the differential cross section is rather complex. Taking into account radially varying partial electron densities of the collision partners, Lindhard and Scharff [62] obtained

$$S_e(v) = \frac{8\pi e^2 a_0}{4\pi\varepsilon_0}\frac{Z_1^{7/6} Z_2}{\left(Z_1^{2/3} + Z_2^{2/3}\right)^{3/2}}\frac{v}{v_0} \tag{65}$$

In view of the scaling with the velocity, the low-energy stopping cross section as function of ion energy is often written as

$$S_e(E) = k_e\sqrt{E} \tag{66}$$

with a constant k_e which depends on the collision partners.

Eqs. (65) and (66) describe a nonlocal average energy loss. For, e.g., the purpose of computer simulation it is also interesting to calculate the electronic energy transfer during a nuclear collision and its dependence on the impact parameter. The model of Firsov[63] considers the interpenetration of the electron clouds of the collision partners (see Fig. 10). In the CMS frame, electrons are mutually crossing the intersecting plane, and, as the relative velocity is small compared to the Fermi velocities, adiabatically accommodate to the dynamic diatomic configuration. For a free electron gas and a Thomas-Fermi interaction potential, the dependence of the local electronic energy transfer on the impact parameter results as

$$T_e(\upsilon, p) = \frac{0.35}{a_0} \frac{(Z_1 + Z_2)^{5/3} \hbar \upsilon}{\left(1 + 0.16 (Z_1 + Z_2)^{1/3} \frac{p}{a_0}\right)^5} \tag{67}$$

which strongly decreases at increasing impact parameter. The integration according to eq. (51) yields[64]

$$S_e(\upsilon) = 5.15 \cdot 10^{-15} (Z_1 + Z_2) \frac{\upsilon}{\upsilon_0} \; eVcm^2 \tag{68}$$

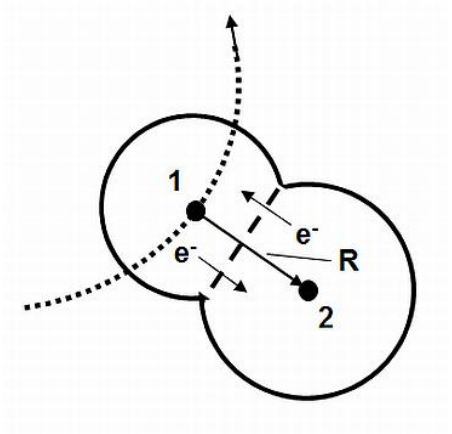

Fig. 10. Electronic energy loss in the Firsov[63] picture. Electrons are transferred between the ion (1) and the target atom (2) and accommodate during the scattering process at varying distance R between the collision partners

For the energy transfer as function of the impact parameter, an alternative semi-empirical expression has been proposed by Oen and Robinson[65] reading

$$T_e(E, p) = \frac{c_1^2}{2\pi a^2} \exp\left(-\frac{c_1}{a} R_{\min}(p)\right) k_e \sqrt{E} \tag{69}$$

where c_1 denotes the decay constant of the leading term of the exponential series approximation of the employed screening function (see eqs. (27) and (32)), and R_{min} the distance of closest approach (see Fig. 3). This function is often being used in computer simulations. Its integration over the impact parameter yields eq. (66) with good precision.

Fig. 11 compares the predictions of eqs. (65) and (68) with experimental data obtained by the transmission of a large variety of ions through thin carbon foils[64]. In average, the Lindhard-Scharff result fits the data very well, whereas the Firsov one slightly overestimates. However, again (see Fig. 7) the data show pronounced shell oscillations which cannot be described by the universal formulas, with significant deviations by factor of up to ~2 for the present data set. This indicates the necessity to employ individual data sets from, e.g., experiments or semiempirical tabulations when precise data are needed (see sect. 4.5).

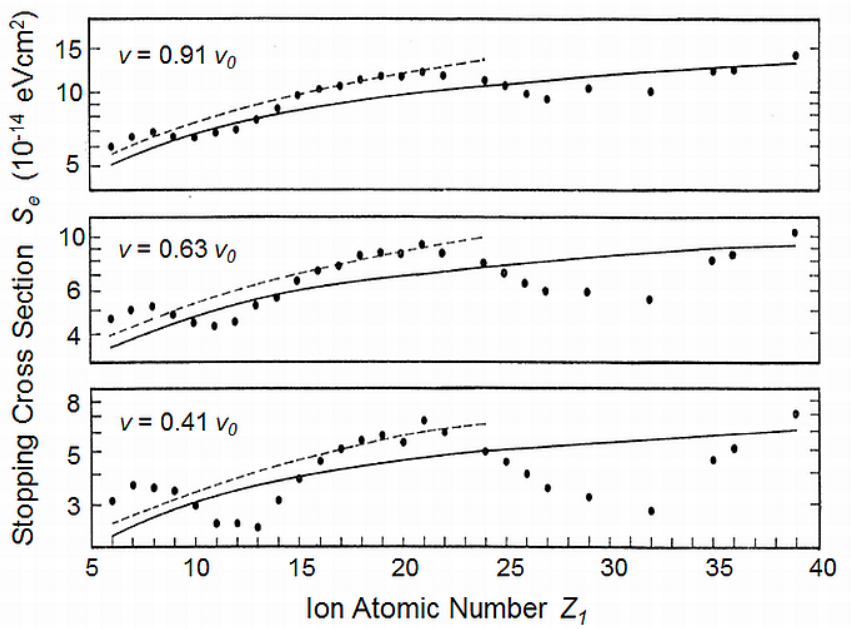

Fig. 11. Low-energy electronic stopping cross sections of different ion species at different velocities in carbon, from experiments (dots) and the theoretical predictions by Lindhard and Scharff (solid lines, eq. (65)) and Firsov (dashed lines, eq. (68)). Velocities are given in terms of the velocity of the first Bohr orbit. The experiments cover the energy range of 0.2...1.5 MeV. (after ref.[64])

4.3.3 High-Velocity Electronic Stopping

Different concepts of the theoretical description of electronic stopping at high ion velocities (i.e. $\upsilon >> \upsilon_0 Z_1^{2/3}$) have been developed by numerous authors. A comprehensive review is given in Sigmund's books[25,26]. Here, we only briefly address the most important models, disregarding any details.

The early model of Bohr[3,4] is naturally based on classical mechanics. For the Coulomb interaction of the ion with a single target electron, the electron is considered as free and, relative to the fast ion, to be at rest before the collision. Then, the binary collision formalism of sect. 2.1 can be applied. For $m_2 = m_e << m_1$, eq. (6) in combination with eq. (14) yields for the energy transfer

$$T(p) = \frac{m_1}{m_e} E \frac{b^2}{p^2 + \frac{b^2}{4}} \tag{70}$$

which is inserted into eq. (51). With the density of electrons $n_e = nZ_2$ this results in

$$S_e(\upsilon) = \frac{2Z_1^2 Z_2 e^4}{(4\pi\varepsilon_0)^2 m_e \upsilon^2} \int_0^{p_{\max}} \frac{2\pi p dp}{p^2 + \frac{b^2}{4}} \tag{71}$$

Apparently, the integral diverges for a maximum impact parameter $p_{\max} \to \infty$. A finite maximum impact parameter can be estimated from the picture of the so- called "adiabatic cutoff". Assuming a characteristic time τ of the collision, the electrons of a target atom contribute to the energy transfer only if their mean orbital frequency ω is smaller than $2\pi/\tau$. Otherwise, they would adiabatically accommodate to the dynamic diatomic configuration, similarly as described in subsection 4.3.1. Using the momentum approximation (see Fig. 4 and eq. (17)), the character-

istic collision time can be estimated from the transverse momentum transfer and its associated force integral, $\Delta p_y = \int F_y dt \approx F(z=0)\cdot\tau$, with the result

$$\tau \approx \frac{4p}{\upsilon} \tag{72}$$

so that the integration in eq. (71) becomes limited to

$$p_{\max} \approx \frac{\upsilon}{4}\frac{2\pi}{\omega} \approx \frac{\upsilon}{\omega} \tag{73}$$

This results in the classical Bohr formula of electronic stopping

$$S_e(\upsilon) = \frac{4\pi e^4}{(4\pi\varepsilon_0)^2}\frac{Z_1^2 Z_2}{m_e\upsilon^2}\ln\left(\frac{4\pi\varepsilon_0}{Z_1 e^2}\frac{m_e\upsilon^3}{\omega}\right) \tag{74}$$

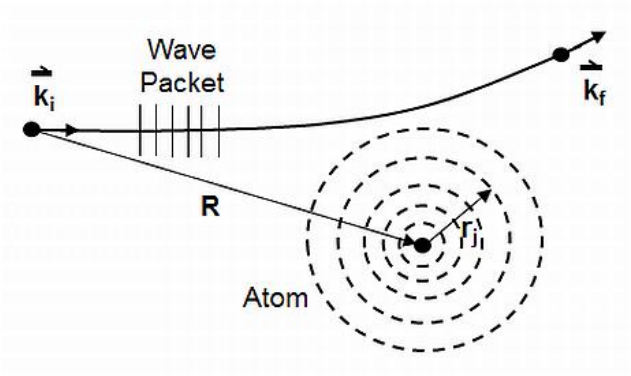

Fig. 12. Quantum-mechanical treatment of high-velocity electronic stopping (schematic) with the internuclear distance *R*, the target atom with different electron orbitals and distances r_j of the electrons from the nucleus, and the wave vectors $\vec{k}_i$ and $\vec{k}_f$ for the incoming and outgoing plane waves, respectively, representing the ion

As estimated from the Bohr criterion (see sect. 2.2), the classical treatment of electronic stopping is not appropriate towards high ion energies. A quantum-mechanical description was first given by Bethe[6] (see also the review by Fano[66]). As sketched in Fig. 12, the scattering process is described by a transition of states of the ion-atom system with an initial state

$$|i\rangle = |\nu_i\rangle(2\pi)^{-3/2}\exp\left(-i\vec{k}_i\vec{R}\right) \tag{75}$$

which is composed of the initial state $|\nu_i\rangle$ of the atom and a plane wave with wave vector $\vec{k}_i$ for the ingoing ion, and a corresponding final state described in the same way. With ε_i and ε_f denoting the initial and final total energies of the atoms, respectively, the stopping cross section is in analogy to eq. (51)

$$S_e = \sum_f \int \frac{d\sigma_{if}}{d\omega}(\varepsilon_f - \varepsilon_i)d\omega \tag{76}$$

where the summation extends over all possible final states of the atom. These may be purely atomic states after electronic excitation or combinations with plane electron waves after ionization. For the differential cross section, the first Born approximation, eq. (22), is inserted with the reduced mass $\mu = m_e$ and the interaction potential

$$V(\vec{R},\vec{r}_1,\ldots,\vec{r}_{Z_2}) = \frac{Z_1 e^2}{4\pi\varepsilon_0}\left(\sum_{j=1}^{Z_2}\frac{1}{\left|\vec{R}-\vec{r}_j\right|} - \frac{Z_2}{R}\right) \tag{77}$$

which describes the Coulomb interaction of the ion with the target nucleus and its individual electrons.

With the momentum transfer vector $\vec{q} = \vec{k}_i - \vec{k}_f$, eqs. (22), (76) and (77) result in

$$S_e = \frac{8\pi e^4 Z_1^2}{(4\pi\varepsilon_0)^2 \hbar \upsilon^2} \sum_f (\varepsilon_f - \varepsilon_i) \int_{q_{min}}^{q_{max}} \frac{dq}{q^3} \left| \langle \nu_f | \sum_{j=1}^{Z_2} \exp(i\vec{q}\vec{r}_j) | \nu_i \rangle \right|^2 \qquad (78)$$

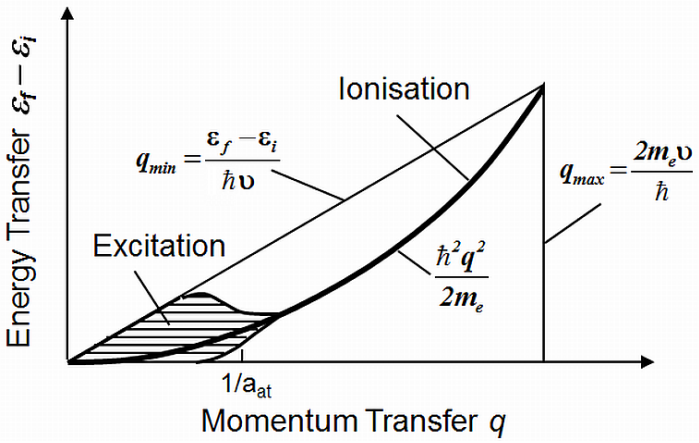

Fig. 13. Regimes of contributions to high-energy electronic stopping resulting from the quantum-mechanical treatment. The different quantities are explained in the text.

From energy conservation, the minimum and maximum energy transfers for a given final state result as $q_{\min} = (\varepsilon_f - \varepsilon_i)/\hbar\upsilon$ and $q_{\max} = 2m_e\upsilon/\hbar$, respectively. The results of the detailed quantum-mechanical evaluation can only be summarized here. As a consequence of the first Born approximation, only the state of one electron of the atom can be altered. The evaluation of eq. (78) naturally demonstrates two regimes of momentum transfer as depicted in Fig. 13. Momentum transfers larger than the inverse of a characteristic atomic radius a_{at} result in an outgoing plane wave for the final state of the electron, which describes an ionization event. At small momentum transfers, different final states may result corresponding to different levels of electronic excitation. Both regimes are separately evaluated, yielding the Bethe formula

$$S_e(\upsilon) = \frac{4\pi e^4}{(4\pi\varepsilon_0)^2} \frac{Z_1^2 Z_2}{m_e \upsilon^2} \ln\left(\frac{2m_e\upsilon^2}{I}\right) \qquad (79)$$

with the so-called "mean ionization potential" I given by

$$\ln I = \sum_f f_{if} \ln(\varepsilon_f - \varepsilon_i) \qquad (80)$$

where f_{if} denote the dipole oscillator strengths of the atom. Eq. (80) cannot be readily evaluated. According to Bloch (see ref. [66]), the mean ionization potential is expected to scale with the atomic number Z_2 of the target material. A good approximation is $I \approx 10eV \cdot Z_2$ except for the lightest target materials, which has been derived from the comparison with experimental data. With this respect, the Bethe formula must be regarded as semi-empirical.

It should be noted that the leading term with the strong energy dependence ($\propto E^{-1}$) is identical in both the classical and the quantum-mechanical result, whereas the logarithmic terms vary slowly with the energy and differ only slightly in the energy dependence. Fig. 14 shows an evaluation of both results for two widely different ion-target combinations, in comparison to semi-empirical data. The results of both formulas are in rather good agreement with the experimental data over a wide range of energies and ion-target combinations and match the high-energy limit

perfectly, although the classical description should not be valid at all in the light-ion case. For the heavy Ge ion (Fig. 14(b)), the classical trajectory regime extends to GeV energies. Indeed, the classical prediction appears to be better here at intermediate energies. On the other hand, the Bethe formula gives an excellent fit for the hydrogen data (Fig. 14(a)) in almost the entire quantum-mechanical regime. This is in accordance with the anticipation that charge transfer should only play a minor role for the lightest ions. In contrast, the predictions for the heavy ion overestimate the stopping at intermediate energies, which might indicate charge transfer effects, and the predictions might be improved by inserting an effective charge of the ion (see subsection 4.3.1) into the stopping formulas rather than the charge number Z_1 of the naked ion. This will enter the definition of semi-empirical data collections which will be discussed in sect. 4.5 below.

As an alternative to the above "atomic" pictures of high-velocity atomic stopping, Lindhard and Winther[67,68] have formulated a "dielectric" continuum description. The interaction of moving ion with the electron gas of the solid induces dipoles. Due to the retardation of the interaction, these result in a net dipole field $\vec{E}_{ind}$ at the position of the ion which points in backward direction. Then, the stopping force becomes

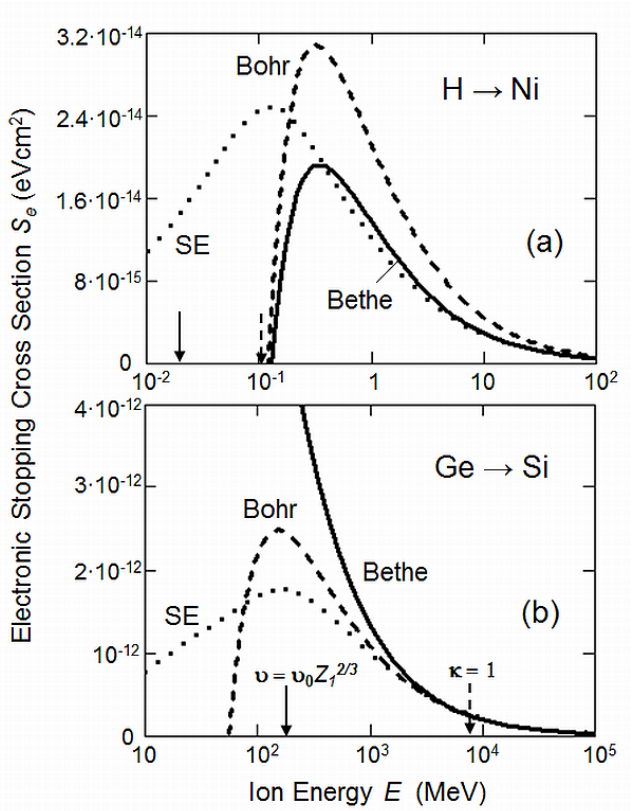

Fig. 14. Electronic stopping for two different ion-target combinations (a,b) according to Bethe (solid lines, eq. (79)) evaluated with $I = 10\ eV \cdot Z_2$ (see text), and according to Bohr (dashed lines, eq. (74)), correspondingly evaluated with $\omega = 10\ eV \cdot Z_2/\hbar$. The predictions are compared to semi-empirical data (dotted lines) obtained from SRIM 2011[69]. The full arrows indicate the energy below which electron attachment becomes effective according to eq. (59), and the broken arrows denote the transition from classical to quantum-mechanical scattering (see eq. (21))

$$-\frac{dE}{ds} = \frac{Z_1 e}{\upsilon}\vec{E}_{ind}\cdot\vec{\upsilon} \tag{81}$$

The evaluation yields

$$S_e(\upsilon) = \frac{4\pi e^4}{(4\pi\varepsilon_0)^2}\frac{Z_1^2 Z_2}{m_e\upsilon^2}\int\frac{dk}{k}\int d\omega\left(-\frac{2}{\pi\omega_0^2}\omega\,\mathrm{Im}\left(\frac{1}{\varepsilon^l(k,\omega)}-1\right)\right) \tag{82}$$

where

$$\omega_0 = \sqrt{\frac{nZ_2e^2}{\varepsilon_0 m_e}} \tag{83}$$

denotes the plasma frequency of the electron gas and $\varepsilon^l(k,\omega)$ its longitudinal polarizability as function of the wave vector k and the frequency ω. Notably, the leading term of eq. (82) is identical to the ones of eqs. (74) and (79). The polarizability can be calculated from first order perturbation theory resulting in

$$\varepsilon^l(k,\omega) = 1 + \frac{2m_e^2\omega_0^2}{\hbar^2 k^2} \sum_n \frac{f(E_n)}{N_n} \left[\frac{1}{k^2 + 2\vec{k}\vec{k}_n - \frac{2m_e}{\hbar}(\omega + i\delta)} + \frac{1}{k^2 - 2\vec{k}\vec{k}_n + \frac{2m_e}{\hbar}(\omega - i\delta)} \right] \tag{84}$$

where the "local electron gas" summation extends over n subshells in momentum space with N_n electrons each and the energies and wave vectors E_n and $\vec{k}_n$, respectively.

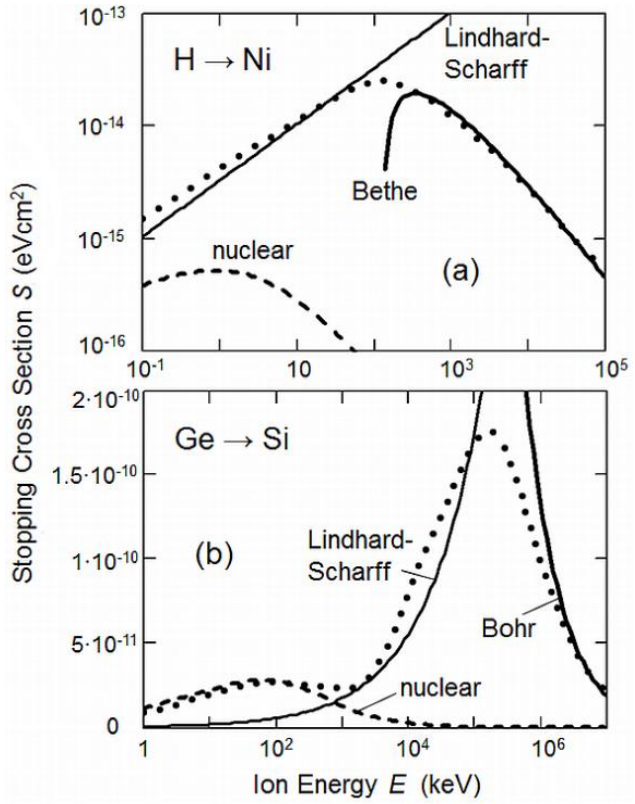

Fig. 15. Theoretical predictions of stopping for a light ion (a) and a medium-mass ion in a lighter substance (b), for high-energy electronic stopping (thick solid lines) according to Bethe (eq. (79)) and Bohr (eq. (74)) (see Fig. 14), for low-energy electronic stopping (thin solid lines) according to Lindhard and Scharff (eq. (65)), and for nuclear stopping (dashed lines) from the Matsunami fit formula (eq. (55)). The dotted lines show semi-empirical data of the total (nuclear+electronic) stopping obtained from SRIM 2011[69]. Note the double-logarithmic presentation in (a)

4.4 Total Stopping Cross Section

For the ion-target combinations chosen for Fig. 14, Fig. 15 summarizes the results of sects. 4.3.1-3. In the light ion case, the contribution of nuclear stopping to the total stopping (see eqs. (52)) is almost negligible except for energies far below 1 keV. In contrast, it is dominant for heavy ions in the keV to MeV range. In both cases, there is a clear separation of the energy regimes where electronic vs. nuclear stopping, and vice versa, dominates. This justifies the separate treatment of electronic and nuclear stopping a posteriori. However, some uncertainty of the concept could

be expected in the rather narrow energy regimes where nuclear stopping and electronic stopping are of similar magnitude.

In detail, the Lindhard-Scharff prediction of electronic stopping works well in case of H in Ni (note that the semi-empirical data of Fig. 15 represent the sum of nuclear and electronic stopping), whereas it underestimates the stopping of Ge in Si. This is in accordance with Fig. 11 where Ge ($Z_1 = 32$) is found at the minimum of the Z_1 oscillations. Nuclear stopping appears to be well described by the universal nuclear stopping integral, eq. (54).

4.5 Semi-empirical Stopping Data

Although the theoretical predictions described in sects. 4.2 and 4.3 are in reasonable agreement with experimental findings in their individual ranges of applicability, they are not sufficiently reliable for precise calculations of, e.g., ion ranges, which are essential for certain applications, as in particular for the development and production in microelectronics. Consequently, stopping data collections have been composed from experimental data. As experimental data of stopping often suffer from systematic errors, the predictions given above can form a guideline to find the best fits to different experimental data sets for specific ion-target combinations and energy ranges.

Earlier collections of stopping data and semi-empirical fits have been published by, e.g., Northcliffe[54], and in a series of books by Andersen and Ziegler[70], Ziegler[71] and Littmark and Ziegler[72]. The data contained in the latter volumes form the basis of the data sets which are available with the SRIM software package[69]. As the latter can be regarded as the present-day standard source of stopping data, the procedures to generate the data[47] will be briefly described in the following.

From the quantum-mechanical and dielectric descriptions of high-velocity electronic stopping (see subsection 4.3.3), the atomic number of the ion enters the stopping cross section only via Z_1^2 in the leading terms of eqs. (79) and (82), respectively. This suggests a scaling of the velocity-dependent electronic stopping S_e of all ions with the electronic stopping $S_{e,H}$ of protons, for which a fairly broad database exists, according to

$$\frac{S_e(Z_1, \upsilon, Z_2)}{S_{e,H}(\upsilon, Z_2)} = \frac{\left(Z_1^{eff}(\upsilon, Z_2)\right)^2}{\left(Z_H^{eff}(\upsilon, Z_2)\right)^2} \tag{85}$$

where effective charges have been inserted according to the concept described in subsection 4.3.1. (It should be noted that the effective charge of the proton has no physical meaning, but is merely part of a fitting concept). In order to obtain a semi-empirical set of proton stopping data, Ziegler et al.[47] evaluated Lindhard's dielectric stopping theory (eq. (82)) with realistic local electron densities from quantum-mechanical Hartree-Fock-Slater calculations[73] or with more precise specific electron densities where available. (It should be noted that the dielectric theory describes the velocity-dependence reasonably well even at velocities below the stopping power maximum.) The theoretical results for different target atoms were fitted to experimental proton stopping power data sets, which formally results in the effective proton charges $Z_H^{eff}(\upsilon, Z_2)$. For target elements with little or no experimental information, interpolation procedures were used. The heavy-ion effective charge was calculated according to the theory of Brandt and Kitagawa[57], from which the authors delineated a universal fitting algorithm which gives more precise results than the simple equation (58). The low-velocity electronic stopping is taken as $S_e(\upsilon) \sim \upsilon^{\alpha}$ with $\alpha = 1$ according to the findings described in subsection 4.3.2, unless experimental data indicate that a different exponent is more appropriate. Finally, the nuclear stopping is taken from the universal fitting formula given in eq. (56).

These semi-empirical stopping data sets are generally in good agreement with the experimental data. (It should be noted that the experimental data often scatter significantly even for

identical ion-target combinations.) It is difficult to rate an all-over accuracy, but an average of $\pm 5\%$ should be a reasonable estimate for most cases. The specific accuracy for a given ion-target combination depends on the velocity range and the quantity and quality of the corresponding experimental database. However, there are also significant deviations in specific cases (see subsection 4.6.2).

The described semi-empirical stopping data are available through the SRIM freeware[69] and have continuously been updated by Ziegler et al. With a convenient user interface, the electronic and nuclear stopping data can be quickly obtained for all ion energies and ion-target combinations.

4.6 Scaling and Additivity Rules

4.6.1 Isotope Scaling

Let us first consider different isotopes of an incident ion species. As seen from eqs. (65), (74), (79) and (82), electronic stopping scales with the velocity of the projectile without a further explicit dependence on its mass. As discussed in sect. 4.2, this holds also for nuclear stopping (see eq. (58)) except for low-energy light ions. For light ions, however, the contribution of nuclear stopping is minor anyway (see, e.g., Fig. 15(a)). Thus, the stopping cross sections of isotopes are identical at identical velocity. Consequently, at known stopping data $S_1(E_1)$ for an isotope 1 with mass $m_{1,1}$, the stopping of an isotope 2 with mass $m_{1,2}$ in the same substance and at energy E_2 is obtained from

$$S_2(E_2) = S_1\left(\frac{m_{1,1}}{m_{1,2}} E_2\right) \tag{86}$$

4.6.2 Reciprocity

At low velocities $\upsilon < \upsilon_0$ where the projectile is essentially neutral and remains neutral after a collision with a neutral target atom, the electronic energy transfer by excitation only depends on the relative motion of the collision partners. Therefore, the stopping cross section must be identical if the projectile and the target atom are interchanged[74]. This is directly evident in the Firsov picture of low-energy electronic stopping and reflected in eqs. (67) and (68) with the symmetry in Z_1 and Z_2. Also the Lindhard-Scharff formula (eq. (65)) is essentially reciprocal, if a factor $Z_1^{1/6}$ is neglected which depends only weakly on Z_1. Thus,

$$S_e(\upsilon, 1 \to 2) = S_e(\upsilon, 2 \to 1) \tag{87}$$

in the low-velocity regime. Sigmund[74] has verified this relation for numerous pairs for which stopping data are available. He also points out that some predictions from SRIM[69] are in clear contradiction to reciprocity, with individual unrealistically high stopping data for heavy ions. Thus, when extracting such data from SRIM as recommended above, it might be helpful to check for consistence with the reciprocal system, and employ corresponding light-ion data in connection with eq. (87) where applicable.

The treatment of nuclear stopping is entirely symmetric in Z_1 and Z_2 (see sects. 3.3 and 4.2). However, there is an asymmetry in the masses as, e.g., seen from eq. (58), with the resulting reciprocity relation

$$m_2 S_n(\upsilon, 1 \to 2) = m_1 S_n(\upsilon, 2 \to 1) \tag{88}$$

4.6.3 Stopping in Compounds

To first approximation, the stopping in a compound material is obtained by simply adding the contributions from the atomic constituents. For a compound with the atomic fractions q_i of the constituents with $\sum_i q_i = 1$, Bragg's rule[75] reads

$$S_C(E) = \sum_i q_i S_i(E) \tag{89}$$

where S_C and S_i denote the stopping cross sections of the compound and the pure elements which form its constituents, respectively. Eq. (89) neglects any chemical interaction. Nevertheless, deviations from Bragg's rule, as far as reported from experiments, rarely exceed 20-30%. The SRIM package[69] also uses Bragg's rule. However, also deviations are implemented as far as they are known from experiments or can be extrapolated in a proper way.

5 Ion Channeling

For the treatment of stopping in the previous section, it was implicitly assumed that the atoms of the solid are randomly arranged. However, most materials exhibit a crystalline structure. Extremes are artificial large-size monocrystals such as being used in microelectronics, but also, e.g., standard metallic or ceramic materials mostly consist of single-crystalline grains with widely varying sizes. Thus, it is mandatory to consider the potential influence of crystallinity on the passage of ions through matter.

If an ion enters a crystalline solid, pronounced effects of crystallinity may be expected only for selected conditions of incidence, as shown in Fig. 16. Due to low-impact parameter nuclear collisions in the first atomic layers, the incidence at arbitrary angles will mostly generate trajectories which are similar to those in random media. However, an ion incident along a low-index crystal direction and entering close to the centre of the channel which is formed by the atomic rows surrounding it, will undergo only small-angle scattering events so that it will maintain its direction with only smooth oscillations around the centre of the channel.

After first corresponding experimental evidence in the early 1960's[76,77], Lindhard[48] has formulated a theoretical basis for ion channeling. Intensive investigations of the effect during the subsequent decade are documented in the textbook edited by Morgan[78]. A compact overview on the fundamentals of ion channeling is also given in the book by Feldman, Mayer and Picraux[79], which is mainly devoted to the application of ion channeling in materials characterization.

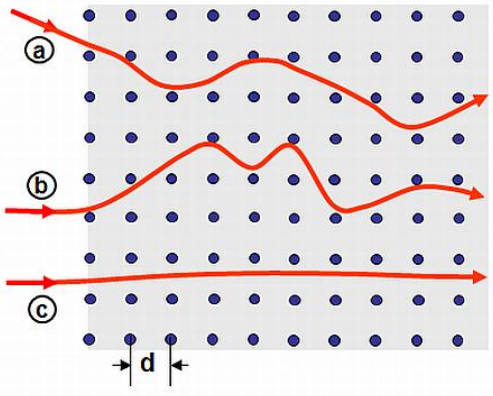

Fig. 16. Trajectories of ions entering a crystalline solid (schematic): (a) Random trajectory of an ion entering at a large angle with respect to a low-indexed crystal direction; (b) random trajectory of an ion entering in the low-indexed direction, but hitting a surface atom; (c) channeled trajectory of an ion entering in the low-indexed direction close to the center of the channel. *d* denotes the distance of the atoms in the atomic strings surrounding the channel

5.1 Critical Conditions

The channeling trajectory (see Fig. 16(c)) is no longer determined by the scattering at individual atoms, but by the scattering from the strings of atoms which surround the channel. As the deviation of the ion flight direction from the direction of the channel is small, the ion trajectory close to a string can be approximated by the coplanar situation of Fig. 17, where the ion trajectory is only described by the radial distance *r* from the string which extends into the *z* direction. The ion is then considered to be channeled if its minimum distance r_{min} to the strings remains larger than a critical value, below which large-angle collisions would occur kicking the ion out and steering it into a random direction.

Similar to the electrostatic potential of a charged wire, the radial interaction potential between the ion and the string is given by

$$U(r) = \frac{1}{d}\int_{-\infty}^{\infty} V\left(\sqrt{z^2 + r^2}\right) dz \tag{90}$$

where d denotes the distance of the atoms along the string and V the binary interaction potential as described in sects. 2.2 and 2.3. For a screened Coulomb potential according to eq. (29), the string potential result

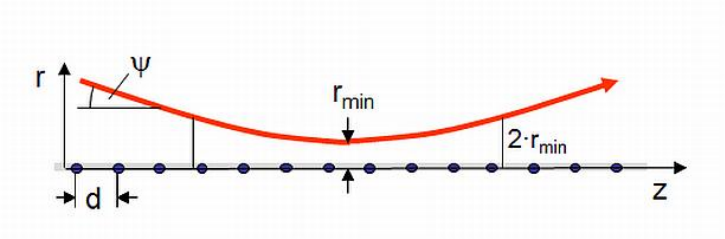

Fig. 17. Channeled ion scattered from a string of atoms surrounding the channel, with a distance r_{min} of minimum approach. The average string charge is indicated by the shaded area. ψ denotes the angle of the trajectory at large distance from the string (corresponding to the direction of an incident ion).

The positions of the ion at the twofold distance of minimum define a characteristic length of the scattering process

$$U(r) = \frac{Z_1 Z_2 e^2}{4\pi\varepsilon_0 d}\,\xi\left(\frac{r}{a}\right) \tag{91}$$

with the screening distance a as in sect. 3.2 and the formal equivalent to the screening function

$$\xi(y) = 2\int_0^{\infty} \frac{\varphi(\zeta)d\zeta}{\sqrt{\zeta^2 - y^2}} \tag{92}$$

Inserting the "standard" potential (eq. (35)) results in

$$\xi(y) = \ln\left(1 + \frac{3}{y^2}\right) \tag{93}$$

Neglecting energy loss and decoupling the motion in the transverse plane from the axial motion, the latter being essentially unaffected, the total energy of the transverse motion is

$$E_{\perp} = U(r) + E(\varphi(r))^2 \tag{94}$$

where φ denotes the (small) angle of the trajectory with respect to the string direction. With the angle ψ at large distance from the string, which can be identified with the angle of incidence when the ion enters the channel, energy conservation requires

$$U(r_{\min}) = E\psi^2 \tag{95}$$

Quite arbitrarily, a characteristic length l_c of the scattering process is defined by the distances $2r_{\min}$ of the ion trajectory from the string, and as a condition for channeling it is required that the characteristic distance along the string contains at least two atoms. With $r_{\min} \approx \psi\, l_c/2$ at small angles, the condition is

$$r_{\min}(\psi) > \psi d \tag{96}$$

Putting eqs. (91), (93), (95) and (96) together, the criterion for channeling becomes

$$\psi < \frac{\psi_a}{\sqrt{2}} \sqrt{\ln\left(1+3\left(\frac{a}{d\psi}\right)^2\right)} \tag{97}$$

with Lindhard's characteristic angle of axial channeling

$$\psi_a = \sqrt{\frac{2Z_1 Z_2 e^2}{4\pi\varepsilon_0 dE}} \tag{98}$$

The approximate analytical solution of the implicit formula (97) for $\psi_L < a/d$ results in the critical angle of channeling at a given energy

$$\psi_{c1} = \psi_a \sqrt{\ln\left(\frac{\sqrt{3}a}{d\psi_a}\right)} \tag{99}$$

This is valid in the limit of high energy. At $\psi_L \approx a/d$, a good estimate is $\psi_{c1} = \psi_a$. In the opposite low-energy regime, the critical angle becomes

$$\psi_{c2} = \sqrt[4]{\frac{3}{2}} \sqrt{\frac{a}{d}\psi_a} \tag{100}$$

Although the basic idea leading to these criteria appears to be somewhat intuitive (see above), they are found in rather good agreement with experimental results and can well be used for practical applications. More precise data can be obtained by computer simulation[78].

The above picture assumes an idealized rigid chain of atoms. In reality, thermal vibrations have to be taken into account. Typically, already around room temperature the thermal vibration amplitude becomes comparable to the distance of minimum approach at the critical angle, as defined above. Thus, a good approximation for the critical angle can be obtained when replacing ψd in eq. (96) by the mean thermal vibration amplitude r_{th}, which results in the critical angle

$$\psi_{c,th} = \frac{\psi_a}{\sqrt{2}} \sqrt{\ln\left(1+3\left(\frac{a}{r_{th}}\right)^2\right)} \tag{101}$$

Channeling cannot only occur along channels between atomic strings in low-indexed crystalline direction, but also between the lattice planes of a crystal. The critical condition for planar channeling can be derived in full analogy to the above, so that only the results will be given here. The continuum potential $Y(y)$, where *y* denotes the distance from the plane, is now obtained by averaging over the plane according to

$$Y(y) = \frac{1}{\bar{d}^2} \int V\left(\sqrt{x^2 + y^2 + z^2}\right) dx dz \tag{102}$$

where $\bar{d}$ denotes the average distance of the atoms in the plane given by

$$\bar{d} = \frac{1}{\sqrt{n d_p}} \tag{103}$$

with the interplanar distance d_p. Again with the standard screening function, the potential of the plane becomes

$$Y(y) = \frac{2\pi Z_1 Z_2 e^2}{4\pi\varepsilon_0 \bar{d}^2} \left(\sqrt{y^2 + 3a^2} - y\right) \tag{104}$$

Again, a characteristic angle of planar channeling can be defined according to

$$\psi_p = \sqrt{\frac{2 Z_1 Z_2 e^2}{4\pi\varepsilon_0 \bar{d} E}} \tag{105}$$

with the high-energy critical angle resulting as

$$\psi_{c1} \approx \psi_p \sqrt{\frac{\sqrt{3}a}{\bar{d}}} \tag{106}$$

With the order-of-magnitude estimate $\bar{d} \approx 10a$ it becomes evident that the critical angles for planar channeling are smaller than the ones for axial channeling by a factor of ~3. An estimate of the critical angle at elevated temperature can again be obtained by inserting the average (linear) thermal vibration amplitude $r_{th}/\sqrt{2}$ into the relation corresponding to eq. (97). The result is

$$\psi_{c,th} = \psi_p \sqrt{\pi \left(\sqrt{\frac{r_{th}^2}{2} + 3a^2} - \frac{r_{th}}{\sqrt{2}} \right)} \tag{107}$$

5.2 Trajectories and Flux Distributions

For axial channeling, the simplified picture of an ion trajectory shown in Fig. 16(c) is misleading in the sense that the special situation of so-called “hyperchanneling” is indicated, when the ion remains in the same channel during its passage through the crystal (see Fig. 18(b)). This is only realized at very small transverse energy when, e.g., the ion enters the channel very close to its centre. In the general case, ions which fulfill the channeling condition may possess a broad range of transversal energies which allows them to overcome the potential minima in the areas of the multistring potential between adjacent strings, i.e. they may frequently jump between adjacent channels. This results in a random trajectory in the transverse plane as indicated in Fig. 18(a), with areas $\pi r_{\min}^2$ around the strings not being accessible at a given transversal energy according to

eq. (95). Thus, in the case of axial channeling, the probability to find the ion in the non-forbidden zone of the transversal plane is uniform.

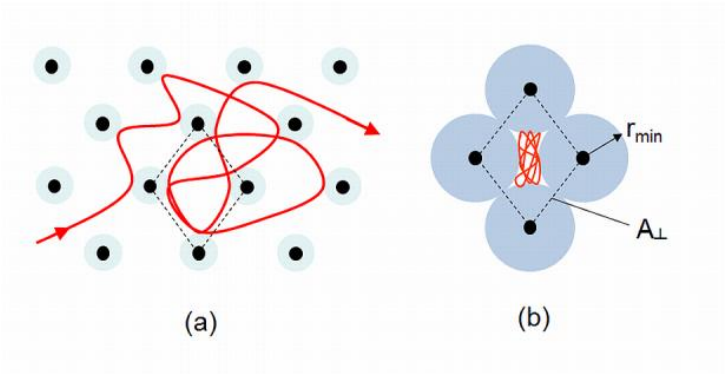

Fig. 18. Ion trajectories under standard channeling (a) and hyperchanneling (b) conditions, projected onto the transverse plane. The dashed rhombs indicate the channel area $A_\perp$. The shaded circles represent the forbidden zones of radius r_{min} according the transversal energy of the ion (see eq. (95))

Fig. 19(a) schematically displays ion trajectories from a beam which hits the crystal in a channel direction. Due to the interaction with the heading atoms of the strings, individual ions are initially deflected depending on their lateral position at the entrance, and thus receive different transversal energies and oscillation amplitudes. Due to its random lateral motion, each ion contributes a constant probability distribution to the total ion flux distribution in the channel, as indicated in Fig. 19 (b).

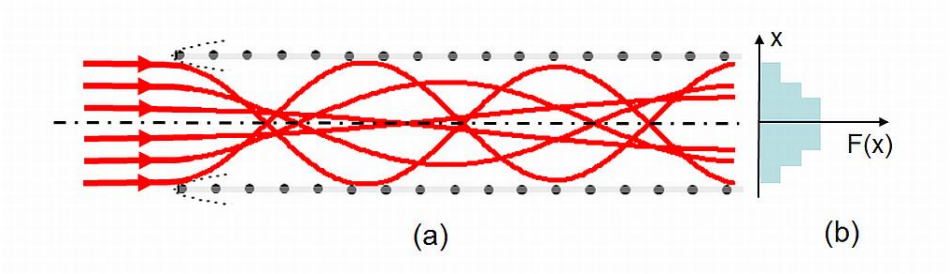

Fig. 19. (a) Idealized axial channeling trajectories of ions which enter the crystal parallel to the direction of the channel in the plane spanned by two strings, and (b) their contributions to the ion flux distribution across the channel. The dotted contours indicate the shadow cones around the heading atoms of the strings, which cannot be entered at a given energy

For an approximate analytical treatment, the cross section of the channel is replaced by a circle of radius $r_\perp$ and equal area $\pi r_\perp^2 = A_\perp$ (see Fig. 20). The flux distribution at a radius r is composed from trajectories with radial amplitudes r' between r and $r_\perp$. Each trajectory with amplitude r' spreads out over an area $\pi r'^2$ in the lateral plane, so that its contribution at r is proportional to $(\pi r'^2)^{-1}$. Thus, the radial flux distribution becomes

$$F_a(r) \propto \int_r^{r_\perp} \frac{2\pi r' dr'}{\pi r'^2} = 2\ln\frac{r_\perp}{r} \tag{108}$$

and with the correct normalization

$$F_a(r) = \frac{1}{\pi r_\perp^2} \ln\left(\frac{r_\perp}{r}\right)^2 \tag{109}$$

which exhibits a pronounced maximum at the center of the channel.

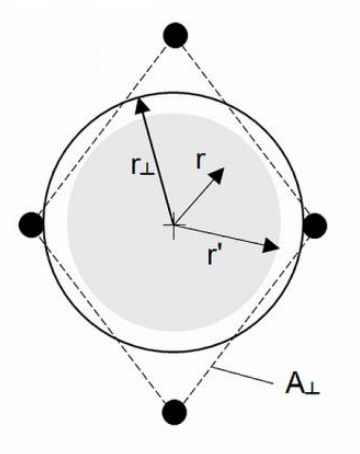

Fig. 20. Simplified channel geometry for the analytical description of the flux distribution of axial channeling. The cross-sectional contour of the channel is replaced by a circle of equal area with radius $r_\perp$. The grey circle represents the area which is occupied by an ion trajectory with radial amplitude r'

For planar channeling, there are well-defined periodic oscillations of the trajectories without any randomization. (Fig. 19 may also be applied to planar channeling when being understood as a cross section normal to the guiding planes and in the plane of the ion trajectories.) Considering an ion with an amplitude x' of its trajectory, the probability to find it at a distance x from the midplane between the two guiding planes is given by the harmonic expression $\left(x'^2 - x^2\right)^{-1/2}$. Therefore, the flux distribution for planar channeling results as

$$F_p(x) \propto \int_x^{d_p/2} \frac{dx'}{\sqrt{x'^2 - x^2}} = ar\cosh\frac{d_p}{2x} \tag{110}$$

and again with the correct normalization

$$F_p(x) = \frac{2}{\pi d_p} ar\cosh\frac{d_p}{2x} \tag{111}$$

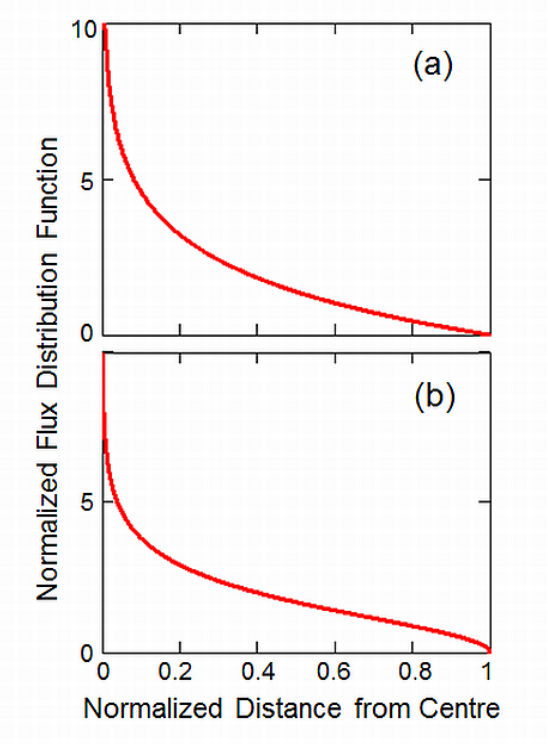

Fig. 21. Ion flux distributions for axial channeling (a) and planar channeling (b), for a beam incident along the channel direction or the planes, respectively, from eqs. (109) and (111), respectively. The respective abscissas represent the distance from the channel axis divided by $r_\perp$ (see Fig. 20), and the distance from the midplane divided by $d_p/2$. For comparability, the distribution functions have been multiplied by $\pi r_\perp^2$ and $2d_p$, respectively

Fig. 21 displays the above results. Although the distributions for axial vs. planar channeling are not directly comparable due to the different geometries, the width around the centre appears to be smaller for planar channeling. This is qualitatively consistent with the smaller critical angle of planar channeling (see sect. 5.1).

5.3 Dechanneling

In an ideal crystal with a rigid lattice, a channeled ion will never leave the channeling direction. Thus, dechanneling requires deviations from the ideal lattice, which may arise from thermal vibrations or from lattice defects, as indicated in Fig. 22.

An initially channeled ion with conditions of incidence close to the critical conditions (see sect. 5.1) approaches the atomic strings (or planes) closely, so that target atoms being displaced from their mean position by thermal vibrations might cause a large angle collision and thereby scattering into a random direction. The fraction of the non-channeled ions then increases with increasing penetration depth through the crystal. Alternatively, dechanneling may occur at crystal defects such as self-interstitials, interstitial impurities, dislocation lines or other stacking fault configurations.

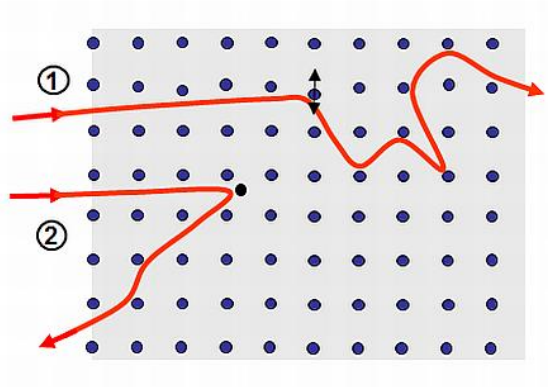

Fig. 22. Examples of dechanneling (schematic): (1) transition from a channeling trajectory to a random trajectory due to thermal vibration of the lattice; (2) dechanneling at an interstitial atom and backscattering

Due to the principle of reversibility of the trajectory, any dechanneled ion will not be able to re-enter a channel unless being scattered again from a displaced atom.

5.4 Stopping under Channeling Conditions

A significant reduction of nuclear stopping is immediately expected, as only small-angle collisions occur with insignificant nuclear energy transfers. On the other hand, any strong influence of channeling on the electronic stopping is less obvious. In particular under axial channeling conditions where the relative time of residence close to the atomic strings is small (see sect. 5.2), the ions mainly meet interstitial electrons with a density different from average, which may result in modified electronic stopping. In the binary collision approach to low-energy electronic stopping, the electronic energy transfer is predicted to strongly decrease at increasing impact parameter (see eq. (67)), which would result in a reduced electronic stopping of channeled ions. However, these effects depend strongly on the specific material and the specific irradiation conditions.

As an example, Fig. 23 shows the stopping force of two different ions in Si under channeling conditions versus the random values, as obtained from transmission measurements through crystalline Si films with submicrometer thickness[80]. In the present range of MeV energies, electronic stopping entirely dominates. The results for axial and planar channeling fall closely together, and are lower than the random values by 20…30% (For axial channeling, it should be noted that the <100> channel, which has been chosen here for experimental reasons, is less open than the <110> in the diamond lattice.) A reduction of stopping of this magnitude is typical for

the channeling in the electronic stopping regime along axes or planes with the lowest Miller indices.

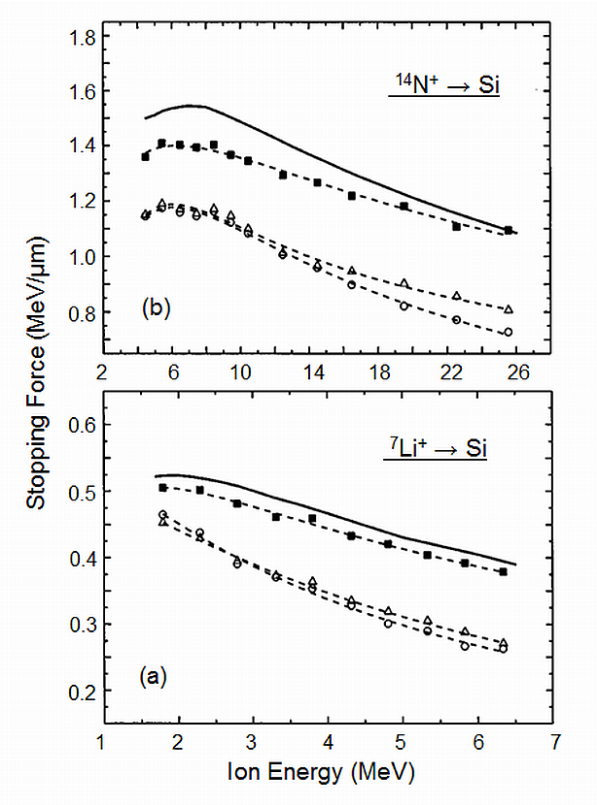

Fig. 23. Stopping force of MeV lithium (a) and nitrogen (b) ions in a silicon single crystal in random direction (full squares) and for channeling along the <100> axis (open circles) and the {110} plane (open triangles). The solid lines show the predictions from SRIM[69] (1995 version). The dashed lines represent analytical fitting curves. (After ref.[80])

6 Computer Simulation of Ion-Solid Interaction

Already during the early stage of the field of ion-solid interaction, it has been realized that ion penetration and associated phenomena can profitably be addressed by computer simulations[14,81,82], into which the elementary processes of scattering and energy loss as described in the previous sections can be entered. Overviews have been given by Eckstein[31] and Smith[32]. There are two basically different approaches which are partly complementary and which differ in their typical areas of application as well as in the corresponding computational effort, which will be described below.

6.1 Binary Collision Approximation

6.1.1 Code Description

In the binary collision approximation (BCA), the motion of a fast atom moving in a solid is described by a sequence of asymptotic trajectories between binary collisions (see Fig. 24). The binary collisions are normally treated as elastic, with the kinematics and interaction potentials as described in sects. 2 and 3, thus mimicking the nuclear scattering and stopping. Electronic stopping can either be applied nonlocally along the free paths λ_c, mostly being taken from semi-empirical data collections (see sect. 4.5), or locally according to eqs. (67) or (69).

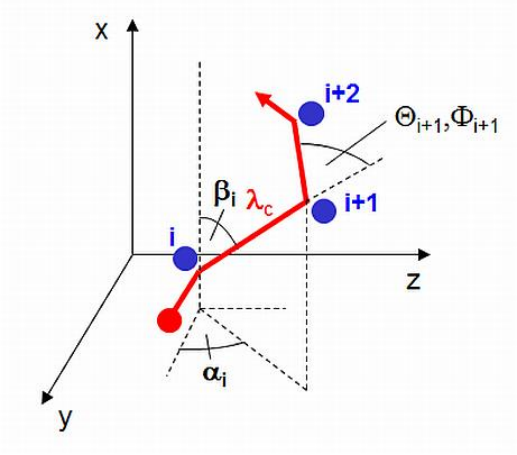

Fig. 24. Sequence of collisions of a moving atom (red) with target atoms (blue) denoted by *i...i+2* in the binary collision approximation, with intermediate free pathlengths λ_c. With the *x* coordinate directed along the inward surface normal, α and β denote the azimuthal and polar angles of motion, respectively, and Φ and Θ the azimuthal and polar deflection angles, respectively, in the laboratory system (Φ is not explicitly shown)

BCA codes have been developed for random or amorphous substances[83-88] as well as for crystalline targets[15,89-91]. However, crystalline codes can also be used for the simulation in polycrystalline and random media by rotation of the crystal for each incident ion or for each new collision[15]. Often, BCA codes have been termed "Monte Carlo" simulation due to the random character of some of the internal variables. However, in a crystalline code with a fixed lattice, only the conditions of ion incidence can be chosen randomly. From that on, the entire trajectory is deterministic due to the fixed position of the target atoms (unless thermal vibrations are admitted). The free pathlength between the subsequent collisions is chosen randomly for random media, whereas the position of the target atoms is chosen randomly for both random and amorphous media.

For the interaction of fast atoms with an amorphous substance, TRIM (TRansport of Ions in Matter)[47,69,88,85] is the most widely spread and used BCA code. Therefore, we will refer in the following particularly to the TRIM model. The amorphous substance is modeled by a fixed free pathlength equal to the mean distance of the atoms in the solid according to

$$\lambda_c = n^{-1/3} \tag{112}$$

A detailed schematic of the collision geometry is shown in Fig. 25.

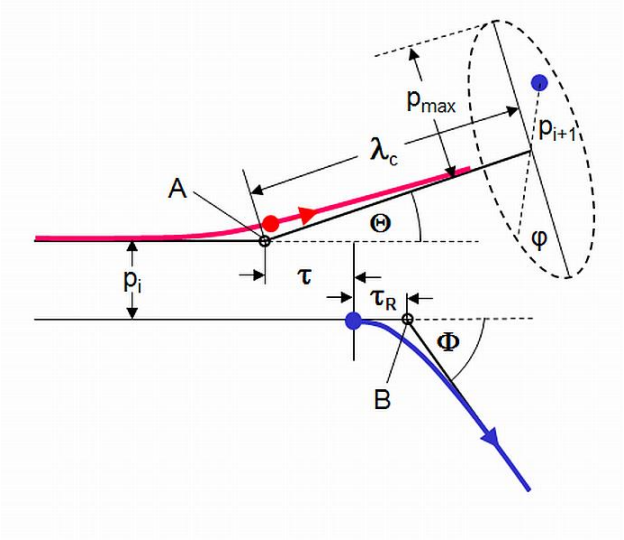

Fig. 25. Details of projectile (red) and recoil atom (blue) trajectories in the binary collisions, and selection of next target atom (upper right). For explanation, see text. For points A and B, see section 6.1.3

The asymptotic trajectories define the so-called "time integral" τ by the distance of the intersection of the asymptotic trajectories from the scattering plane. Similarly, a time integral τ_R is defined for the recoil atom. TRIM uses the time integrals from the hard-sphere approximation, reading

$$\tau = p \tan \frac{\vartheta}{2} \tag{113}$$

with ϑ denoting the scattering angle in the center-of-mass system, and

$$\tau_R = 0 \tag{114}$$

Each new collision partner is chosen within a circle around the asymptotic trajectory with the maximum impact parameter $p_{\max}$ as its radius. The choice

$$p_{\max} = \sqrt{\frac{\lambda_c}{\pi n}} \tag{115}$$

defines a cylinder of length λ_c which contains one target atom in average, so that one collision takes place per atom of the substance. (However, it should be noted that some versions of the TRIM family[92,93] allow additional "soft" collisions with larger impact parameters in outer annular regions.) The actual impact parameter is then chosen randomly from a random number $r_p \in [0,1]$ according to

$$p = p_{\max} \sqrt{r_p} \tag{116}$$

A second random number r_φ selects the azimuth within the impact parameter circle as

$$\varphi = 2\pi r_\varphi \tag{117}$$

which defines also the azimuthal deflection angle of the subsequent collision. The polar deflection angle is related to the impact parameter by the classical trajectory integral, eq. (10). However, its solution for each new collision would require excessive computational effort. One way out is the calculation and tabulation of the scattering function $\vartheta(p)$ for all occuring projectile-target combinations at the beginning of the simulation run, so that the data for each collision can be obtained from table lookup and interpolation[84,87]. Instead, TRIM uses an analytical approximation ("Magic")[47,85] with specific parameters for the chosen screening function, which reproduces the results of the exact integration of eq. (10) very well. In standard TRIM[47,69], the ZBL screening function (eqs. (32) and (33)) is employed.

Nonlocal electronic energy loss is treated according to

$$T_{e,nl} = nS_e(\lambda_c - \tau) \tag{118}$$

Alternatively, local electronic energy loss $T_{e,l}$ can be employed at sufficiently low energy. TRIM uses the Oen-Robinson formula (eq.(69)), again with parameters which are specific to a given screening function[31]. Often, also a combination of nonlocal and local electronic energy loss is defined, such as the equipartition $T_e = 0.5(T_{e,nl} + T_{e,l})$.

The "state" of a moving atom directly after a collision *i* (see Fig. 24) is described by the space coordinates (x_i, y_i, z_i) at the deflection point, the directional angles (α_i, β_i) and the energy E_i. The simulated sequence of collisions then consists of a geometrical translation with an operator *TS*

$$(x_{i+1}, y_{i+1}, z_{i+1}) = TS(\lambda_c, \tau, \alpha_i, \beta_i) \bullet (x_i, y_i, z_i) \tag{119}$$

and a re-direction with an angular transformation operator *TA*

$$(\alpha_{i+1}, \beta_{i+1}) = TA(\Theta, \varphi) \bullet (\alpha_i, \beta_i) \tag{120}$$

For brevity, the explicit expressions for *TS* and *TA* are not given here. With the nuclear energy transfer from eq. (6), the energy is reduced according to

$$E_{i+1} = E_i - T - T_e \tag{121}$$

As any incident projectile, also any recoil atom which is generated by a nuclear collision can be traced in this way. The initial position of the recoil is given by (see Fig. 24)

$$(x_0, y_0, z_0) = TSR(\lambda_c, \varphi, \alpha_i, \beta_i) \bullet (x_i, y_i, z_i) \tag{122}$$

and its initial directional angle by

$$(\alpha_0, \beta_0) = TAR(\Phi, \varphi) \bullet (\alpha_i, \beta_i) \tag{123}$$

with corresponding operators *TSR* and *TAR*, respectively, again without their explicit expressions here. The initial energy of the recoil is

$$E_0 = T - U_b \tag{124}$$

with a "bulk binding" energy U_b. This implies that a recoil is only generated at $T > U_b$.

The trajectories of any incident projectile or recoil atom can then be traced until they meet a surface, or the energy falls below a predefined "cutoff" energy E_{co} which defines the endpoint of a specific trajectory. Fig. 26 shows an example of ion and recoil trajectories which have been generated by TRIM[69].

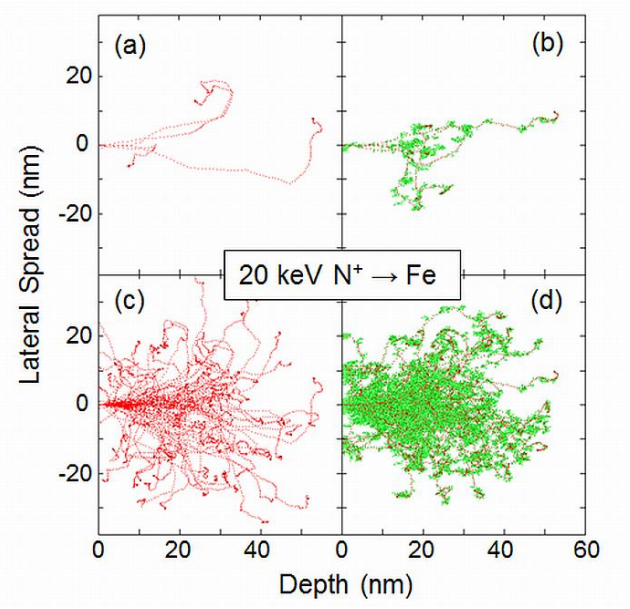

Fig. 26. Ion and recoils trajectory simulations using TRIM[69] for 20 keV nitrogen ions incident on iron: Ions only (a,c) and ion plus recoil (b,d) trajectories, for 5 (a,b) and 100 (c,d) incident ions. The three-dimensional trajectories are projected onto a plane. The pairs (a,b) and (c,d) are from different runs each with different ion trajectories

6.1.2 Input Parameters

As described above, the cutoff energy E_{co} and the bulk binding energy U_b have to be predefined for each specific application of the BCA simulation. The choice of the bulk binding energy is not

obvious[31]. Standard TRIM[47,69] uses a few eV as default parameter for different materials, reflecting the enthalpies of vacancy formation. Applications of other codes prefer $U_b = 0$ in the absence of better knowledge[65,92,93]. The cutoff energy should be chosen as large as possible in order to limit the computation time, but small enough to exclude any influence on the results. Additional energy parameters will be addressed in sections 9-11.

In addition to the energy parameters, the local versus nonlocal description of the electronic stopping (see above) can be regarded as a free parameter. There is also some freedom in the choice of the screening function. These possible variations of the input parameters may be of significant influence on the results. In particular for low energy, where nuclear stopping is important, the definition of electronic stopping is ambiguous, and the choice of the energy parameters becomes more influential. Depending on the problem, the results of the simulations may vary significantly with the choice of these parameters. Thus, the predictive power of BCA simulations relies on agreed sets of input data which have proven to be useful in comparison with experimental data, rather than on well-defined parameters which are known *a priori*.

6.1.3 Range of Validity

Towards high particle energy, there is no physical limit to the validity range of BCA simulations (provided that suitable nuclear interaction potentials are employed). A practical limitation results from the increasing computational effort due the large number of collisions along high-energy trajectories. However, as nuclear stopping and angular deflections become small at sufficiently high energy, this can be counteracted by algorithms which replace frequent collisions by rare effective ones, such as in standard TRIM[47,69].

Towards low energy, the range of validity is determined by the breakdown of the binary collision approximation when many-body interaction becomes significant. A quantitative criterion can be developed from the requirement that the BCA distance of minimum approach of the collision partners must be smaller than the nearest-neighbor distance in the solid[15,31]. A measure of the former is the distance between points A and B in Fig. 25, which increases at decreasing energy. The evaluation for a suitable screened Coulomb potential results in a critical energy around 20 eV as a rough average for different projectile-target combinations. A similar magnitude results from the criterion that the flight time of the projectile along the nearest-neighbor distance should be shorter than the inverse of the lattice vibration frequency, meaning that the projectile interacts only once with a vibrating lattice atom. This corresponds to the criterion that the projectile velocity should be larger than the sound velocity of the material. In summary, the binary collision approximation becomes definitively questionable at energies below ~10 eV.

It should be noted here that the analytical modeling of ion-solid interaction inherently implies the binary collision approximation as well. Thus, the above discussion of the validity range identically applies to analytical theory.

6.1.4 Dynamic Simulation

Basic codes using the binary collision approximation, such as standard TRIM[47,69] and MARLOWE[15] for amorphous and crystalline materials, respectively, represent static simulations in the sense that the irradiated substance is not affected by the ion bombardment. Thus, they describe the limit of zero irradiation fluence, not covering, e.g., the accumulation of implanted species or ion-induced damage, the target erosion by collisional emission of atoms from the surface, or stoichiometric alterations of multicomponent substances due to collisional relocation of atoms.

Several extensions of BCA codes which allow the simulation of the dynamic development of the stoichiometry[93-98] or damage[86,99-101] versus ion fluence have been described in literature. While damage accumulation will be addressed in a later section (10.3), the algorithm of

TRIDYN[93,102,103], which is applicable to one-dimensional surface erosion and/or deposition, and the in-depth dynamic development of the elemental composition, will be described in the following.

Realistic broad-beam irradiations with significant compositional modification require ion fluences of typically 10^{16} ions/cm^2 or higher, so that a realistic ion-by-ion simulation would exceed even the present-day computer capabilities by far. Therefore, each projectile in the simulation (so-called pseudoprojectile) is chosen to represent a certain increment of ion fluence (typically 10^{12} ions/cm^2 or larger) according to

$$\Delta\Phi = \frac{\Phi_{tot}}{M_{tot}} \tag{125}$$

where M_{tot} denotes the total number of pseudoprojectiles by which an irradiation with a real fluence Φ_{tot} is simulated.

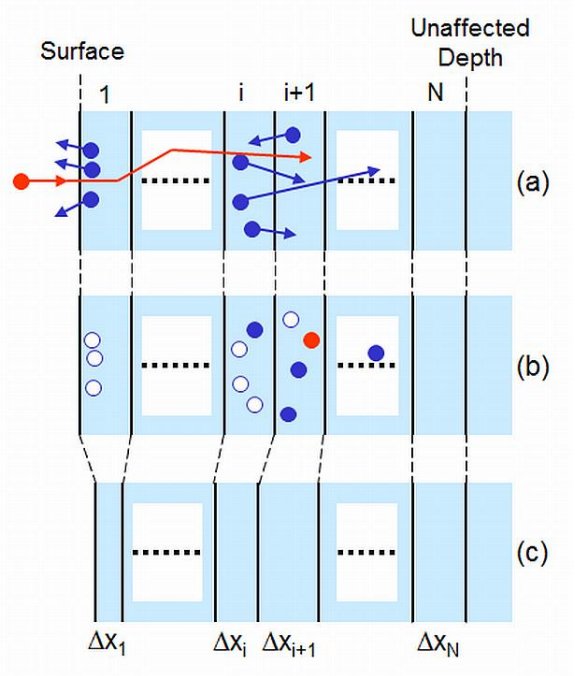

Fig. 27. Scheme of dynamic relaxation in TRIDYN[93,94]. (a) Initially, the target substance is subdivided into slabs of equal thickness. The incident projectile transfers energy to target atoms which are set in motion. (b) The projectile has been implanted, and target atoms have been transported to other slabs or emitted from the surface, leaving vacant sites behind. (c) According to the resulting under- or over-densities, the thickness of the slabs is allowed to relax to be ready for the subsequent incoming ions. The slabs are indexed by 1...*N*, their thicknesses are denoted by Δx

As shown in Fig. 27, the target substance is initially subdivided into N slabs of equal thickness Δx_0, extending to a depth which is not affected by the irradiation. Each slab is allowed to contain N_a different atomic species, including one or more species of the incoming beam, with fractional compositions q_{ij} $(i = 1..N; j = 1..N_a)$ so that $\sum_{i,j} q_{ij} = 1$. The total atomic density in each slab, n_i, is given by

$$\frac{1}{n_i} = \sum_j \frac{q_{ij}}{n_{j0}} \tag{126}$$

where the partial atomic densities n_{j0}, which are entered as input parameters, are the inverse of the fixed atomic volumes of the species j. Eq. (126) neglects any chemical interaction between the different species which would lead to a nonlinear superposition of the atomic volumes.

The simulation of the history of the pseudoprojectile including generated recoils (Fig. 27(a)) may result in the implantation of the pseudoprojectile, the emission of pseudoatoms from the surface, and their relocation in the bulk (Fig. 27(b)). Each added or removed pseudoatom repre-

sents a change $\Delta\nu_{ij}$ of the local areal density of the respective species *j* in slab *i* according to the normalization factor of eq. (125). The new areal densities are then calculated from the old ones by

$$\nu_{ij} = q_{ij} n_i \Delta x_i + \Delta\nu_{ij} \tag{127}$$

At constant atomic volumes, the thickness the slabs is then relaxed (see Fig. 27(c)) according to

$$\Delta x_i = \sum_j \frac{\nu_{ij}}{n_{j0}} \tag{128}$$

to be ready for the incidence of the subsequent pseudoprojectile with modified fractional compositions

$$q_{ij} = \frac{\nu_{ij}}{\sum_k \nu_{ik}} \tag{129}$$

By this procedure, certain slabs may become very thin or excessively thick. These are added to a neighboring slab or split into to two slabs of half thickness, respectively. In TRIDYN, the criterion for slab combination or splitting is $0.5\Delta x_0 < \Delta x_i < 1.5\Delta x_0$.

The procedure of BCA simulation and relaxation is repeated for the chosen total number M_{tot} of pseudoprojectiles. For a given total fluence (see eq. (125)), the number of pseudoprojectiles has to be chosen sufficiently large in order to obtain a sufficient statistical quality of the result. At an excessively small total number of pseudoprojectiles, the number of added or removed atoms per pseudoprojectile in certain slabs may even exceed the total number of atoms in that slab, which has to be avoided. As a rule of experience, the number of atoms in any slab should not change by more than about 5% per pseudoprojectile throughout the whole run in order to avoid artefacts.

6.2 Molecular Dynamics Simulations

In molecular dynamics (MD) simulations (often also denoted as classical dynamics simulations) of ion-solid interaction[14,31,32,104-106], the Newtonian equations of motions of a many-body system are solved in time steps for an ensemble of atoms representing the solid (see Fig. 28). Compared to BCA simulations, there is a number of obvious advantages. Many-body interaction is generically included, so that there is no low-energy limitation. Consequently, incident projectiles and recoil atoms can be traced until they are thermalized with the solid. With the choice of a realistic interaction potential, even their final interstitial or substitutional position can be modeled. Advanced interaction potentials may take into account three-body forces and thereby directed bonds in covalent solids. Further, any dynamic alteration of the cell due to ion implantation or atomic relocation can easily be accounted for.

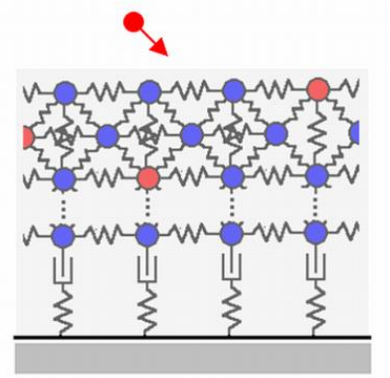

Fig. 28. Schematic representation of a molecular dynamics computational cell, with elastic forces between the atoms and frictional coupling at the bulk boundary being indicated. The incident ion (arrow) may be integrated into the solid after slowing down

However, the comparatively large computational effort sets limits to the practical applicability of MD simulations. In practice, there is an upper limit to the accessible particle energies in order to avoid excessively large computational cells. The limited computational speed also imposes a limitation of the time between the incidence of subsequent ions for the modeling of realistic ion fluences, so that often unrealistically short equilibration times for each single ion with its associated recoil atoms must be accepted.

6.2.1 Numerical integration

Different algorithms have been developed for the simultaneous integration of the equations of motion[31,32]. As a common example, the Verlet[107] algorithm is presented here. The position vectors $\vec{r}_i$ of the atoms of the computational cell at the $(n+1)^{\text{th}}$ time step of the simulation result from the ones at the n^{th} time step as

$$\vec{r}_i^{(n+1)} = \vec{r}_i^{(n)} + \vec{\upsilon}_i^{(n)} \Delta t^{(n)} + \frac{1}{2} \vec{a}_i^{(n)} \left(\Delta t^{(n)}\right)^2 \tag{130}$$

where $\Delta t^{(n)}$ denotes the duration of the n^{th} time step, and $\vec{\upsilon}_i$ and $\vec{a}_i$ the velocities and accelerations of the atoms, respectively. The propagation relation of the velocities is

$$\vec{\upsilon}_i^{(n)} = \vec{\upsilon}_i^{(n-1)} + \frac{1}{2} \left(\vec{a}_i^{(n)} + \vec{a}_i^{(n-1)}\right) \Delta t^{(n)} \tag{131}$$

The accelerations are given by the forces $\vec{F}_i$ resulting from the interaction with the neighboring atoms according to

$$\vec{a}_i^{(n)} = \frac{\vec{F}_i^{(n)}}{m_i} = -\frac{1}{m_i} \vec{\nabla} V_i\left(\vec{r}_i^{(n)}\right) \tag{132}$$

where V_i represents the interaction potential between atom i and the surrounding atoms. The Verlet algorithm is precise in second order of the time step. Typical time step durations are a few fs.

In order to save computer time at a given cell size, higher-order algorithms can be employed which allow larger time steps due to better precision. Variable time steps can be optimized using different empirical recipes, such as, e.g., in ref.[108]. As a further standard procedure for the reduction of computer time, neighbor lists are defined for sufficiently short-ranged potentials, thus reducing the number of interaction terms in eq. (132) significantly.

Depending on the problem, the number of atoms in the computational cell and the computing power, the simulation for each incident ion or primary recoil can presently be run for a total physical time up to about 10…100 ns and for a maximum number of atoms in the cell of the order of $10^{7\ldots8}$.

6.2.2 Interaction potentials

The application of MD simulations down to thermal energies of the moving atoms requires the definition of interaction potentials which are consistent with the atomic binding in the solid. In particular and in contrast to the potentials described in sect. 3, these potentials must have an attractive regime at intermediate atomic separation, which, e.g., defines the equilibrium interatomic distance. For an efficient use in the MD simulations, the interaction potential should be implemented analytically. Correspondingly, numerous simple and more elaborate functionals have been proposed. Generally, such functionals exhibit parameters which are optimized to fit a set of properties of the investigated specific system, such as the dimer bond lengths, the elastic

and thermophysical properties, or the enthalpies of fusion or point defect formation. Mostly only a subset of these properties is satisfactorily reproduced, so that the optimum potential parameterization depends on the purpose of a specific simulation even for the same monoatomic or compound material.

Here, we will explicitly address a few of the most commonly used functionals for the solid-state potential. If only binary central forces between the atoms are considered, the potential of atom *i* reads

$$V_i(\vec{r}_i) = \sum_{j \neq i} V_{ij}\left(\left|\vec{r}_i - \vec{r}_j\right|\right) \tag{133}$$

with the pair potentials V_{ij} of interactions with the surrounding atoms. An example of a simple pair potential between two atoms at an internuclear distance R is the Lennard-Jones potential[109]

$$V(R) = 4\varepsilon\left[\left(\frac{\sigma}{R}\right)^{12} - \left(\frac{\sigma}{R}\right)^{6}\right] \tag{134}$$

with parameters ε (representing the minimum of the potential function) and σ (defining the equilibrium dimer distance). An example is plotted in Fig. 29(a).

Whereas the Lennard-Jones potential or the similarly simple Morse[110] potential have been employed in particular in early MD simulations for metals, numerous more advanced functionals have been developed. For system with mainly metallic binding, the so-called embedded-atom model (EAM)[111,112] is often employed. Any atom in the solid can be regarded as being embedded in the electron gas formed by the valence electrons of the other atoms. The potential is then written as ($R_{ij} = \left|\vec{r}_i - \vec{r}_j\right|$)

$$V_i(\vec{r}_i) = -f_e\left(n_e(\vec{r}_i)\right) + \sum_{j \neq i} \phi_{ij}\left(R_{ij}\right) \tag{135}$$

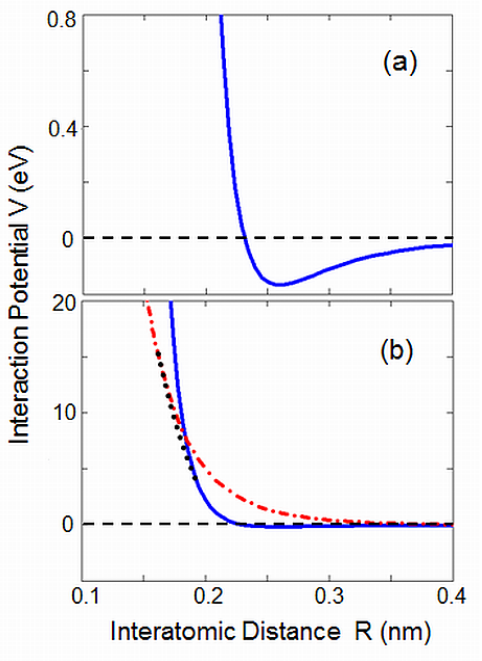

Fig. 29. Simple pair potential function for molecular dynamics simulations. (a) Lennard-Jones potential for Cu-Cu interaction (eq. (134)); (b) the Lennard-Jones potential (solid line) compared to the Cu-Cu screened Coulomb potential (dashed-dotted line) with the "universal" screening function (eqs. (29), (32) and (33)). An interpolating spline function is indicated by the dotted line. The Lennard-Jones parameters for Cu are $\varepsilon = 0.167$ eV and $\sigma = 0.2315$ nm

where f_e denotes a universal embedding function (given numerically) which depends on the local electron density n_e, and ϕ a short-range central pair potential taking into account the inter-

action with the direct neighbors. The local electron density is superimposed from the atomic electron densities n_e^{at} of all atoms, i.e.

$$n_e(\vec{r}_i) = \sum_{j \neq i} n_{e,j}^{at}(R_{ij}) \tag{136}$$

which are obtained from, e.g., quantum-mechanical Hartree-Fock calculations. The pair potential is defined as a Coulomb potential

$$\phi_{ij}(R_{ij}) = \frac{Z_i Z_j^{eff}(R_{ij}) e^2}{4\pi\varepsilon_0 R_{ij}} \tag{137}$$

with effective charges Z^{eff} of the surrounding atoms written as

$$Z_j^{eff}(R_{ij}) = Z_j^0 \left(1 + \beta R_{ij}^{\nu}\right) e^{-\alpha R_{ij}} \tag{138}$$

with Z^0 as the number of valence electrons and parameters α, β and ν. For the embedding function, also the Finnis-Sinclair[113] tight-binding relation $f_e(n_e) \propto \sqrt{n_e}$ can be employed[114] which results in a different parametrization.

Whereas the EAM potential has become a standard for a large variety of metals and intermetallic compounds, the construction of interaction potentials for covalent or ionic systems is considerably more laborious, so that those are only available for selected systems. A corresponding class of parameterized potentials comprises the so-called "bond-order" potentials, which additionally incorporate three-body terms. Then, the potential is given by

$$V_i(\vec{r}_i) = \sum_{j \neq i} V_{ij}(R_{ij}) + \frac{1}{2} \sum_{j \neq i} \sum_{i \neq k \neq j} V_{ijk}(\vec{r}_i, \vec{r}_j, \vec{r}_k) \tag{139}$$

An example is the Stillinger-Weber[115] potential which has been developed originally for silicon. In analogy to eq. (134), the two-body term is written as

$$V_{ij}(R_{ij}) = \varepsilon f_2\left(\frac{R_{ij}}{\sigma}\right) \tag{140}$$

with energy and bond length parameters ε and σ, respectively, and the functional

$$f_2(x) = \begin{cases} A\left(Bx^{-p} - x^{-q}\right) \exp\left(\dfrac{1}{x-a}\right), & x < a \\ 0 \quad else \end{cases} \tag{141}$$

with parameters *A*, *B*, *p* and *q* again in analogy to the Lennard-Jones potential, and an additional cutoff parameter *a*. Similarly, for the three-body term

$$V_{ijk}(\vec{r}_i, \vec{r}_j, \vec{r}_k) = \varepsilon f_3\left(\frac{\vec{r}_i}{\sigma}, \frac{\vec{r}_j}{\sigma}, \frac{\vec{r}_k}{\sigma}\right) \tag{142}$$

with

$$f_3(\vec{x}_i, \vec{x}_j, \vec{x}_k) = h(x_{ij}, x_{ik}, \theta_{ijk}) + h(x_{ij}, x_{jk}, \theta_{jik}) + h(x_{ik}, x_{jk}, \theta_{kij}) \tag{143}$$

where $x_{ij} = \left|\vec{x}_i - \vec{x}_j\right|$, and with θ_{ijk} denoting the angle subtended by the reduced distance vectors $\left(\vec{x}_j - \vec{x}_i\right)$ and $\left(\vec{x}_k - \vec{x}_i\right)$, and

$$h\left(x_{ij}, x_{ik,}\theta_{ijk}\right) = \begin{cases} \lambda\left(\cos\theta_{ijk} - \cos\theta_0\right)^2 \exp\left(\dfrac{\gamma}{x_{ij} - a} + \dfrac{\gamma}{x_{ik} - a}\right), \\ \qquad x_{ij} < a \quad and \quad x_{ik} < a \\ 0 \qquad else \end{cases} \tag{144}$$

where θ_0 denotes the bond angle in the ideal crystal. Thus, eq. (144) optimizes the bond angles. The exponential terms in eqs. (141) and (144) provide a smooth exponential decrease so that the interaction potential vanishes at the cutoff distance *a*.

Other commonly used bond-order potentials have been formulated by Tersoff[116-118] (originally for Si, C, Ge and SiC) and Brenner[119] for carbon including hydrogen-carbon interaction. Numerous modifications and extensions are available, in particular to treat compounds (see, e.g., ref.[120] and references therein). Further, special potentials have been developed for systems where long-range Coulomb forces and charge transfer between the atoms are important, such as in oxides (see. e.g., refs.[121,122]).

The interaction potentials described above are valid for the dynamics in the solid at moderate kinetic energy, being adjusted, as mentioned above, to the properties of the solid close to thermal equilibrium. Thus, they do not cover the interaction of energetic atoms as described by the screened Coulomb potentials of sect. 3.2. This is demonstrated in Fig. 29(b) for the model case of a Cu dimer. For this case, the Lennard-Jones potential becomes clearly too hard above a relative energy of $\sim$10 eV, so that a smooth transition between the solid-state potential and the screened Coulomb potential has to be accomplished in order to cover the entire energy range for energetic ion bombardment. For this purpose, the selected solid-state potential is commonly combined with the ZBL potential (eqs. (29), (32) and (33)), using an appropriate spline fit.

6.2.3 Boundary Conditions

In order to reduce the computational effort of MD simulations as much as possible, the number of atoms in the computational cell should be kept as small as possible. On the other hand, any significant influence of the truncation on the results has to be excluded. The choice of the size and the processing at the boundaries depend on the specific problem.

Often, periodic lateral boundary conditions are chosen, by which energetic particles, which leave the cell through a plane perpendicular through the surface, are re-entered at the opposite plane. This would be appropriate, e.g., to simulate large-area irradiation. In contrast, for the simulation of single energetic impacts, it may be preferable to use open boundaries, as periodic boundaries might introduce an artificial non-linear superposition of atomic motion.

Similar considerations apply to the bottom boundary of the cell. In addition and in particular for broad-beam incidence, the deposited heat has to be removed from the cell in order to avoid overheating far above a given substrate temperature. With periodic lateral boundary conditions, this would be accomplished only at the bottom boundary plane. A simple algorithm is to keep the bottom plane of atoms fixed, and to define a small number of bottom atomic layers where a velocity-dependent friction term is added to the equations of motion, which removes the heat during a sufficiently long equilibration time[123]. Another common method is the Berendsen[124] "thermostat" applied to a few bottom atomic layers, within which the velocities are scaled after each time step according to

$$\vec{v}_i' = \vec{v}_i \sqrt{1 + \frac{\Delta t}{\tau_T}\left(\frac{T_0}{T} - 1\right)} \tag{145}$$

where τ_T is a predefined time constant, T_0 the macroscopic temperature of the system to be modeled and T the kinetic temperature of the thermostat layer as calculated from the kinetic energies before the velocity scaling.

7 Ion Ranges and Range Distributions

7.1 Analytical Treatment

Stopping in connection with nuclear scattering determines the trajectory of an ion in a solid, as indicated in Fig. 30. Due to the statistical character of the scattering processes, the trajectories will be widely different. By electronic and nuclear stopping, the ion is continuously slowed down, and it will finally come to rest in a material of sufficient thickness when its residual energy reaches roughly the lattice binding energy. At known stopping force, the mean total pathlength of the ion can be directly calculated from

$$\overline{R}_t(E) = \frac{1}{n}\int_0^E \frac{dE'}{S(E')} \tag{146}$$

where E now denotes the energy of incidence, and the total stopping cross section S represents the sum of electronic and nuclear stopping according to eq. (52). When nuclear stopping can be neglected (as, e.g., for light ions), and electronic stopping is proportional to the ion velocity at sufficiently low energy (see eq. (66)), the mean total pathlength becomes

$$\overline{R}_t(E) = \frac{2}{nk_e}\sqrt{E} \tag{147}$$

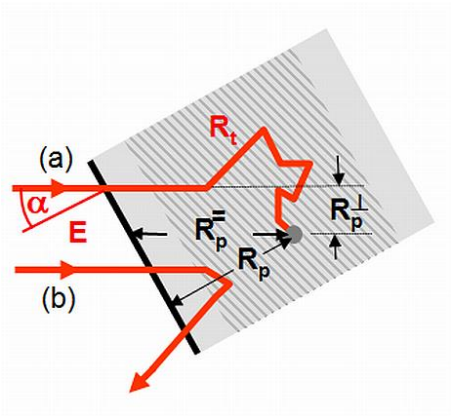

Fig. 30. Trajectory (schematic 2-dimensional projection) of an individual ion incident at an energy E and an angle α with respect to the surface normal, which comes to rest in the solid (a). The associated range definitions are the total pathlength R_t and the longitudinal, lateral and normal projected ranges, $R_p^{=}$, $R_p^{\perp}$ and R_p, respectively. During broad-beam irradiation, ions will come to rest within a subsurface sheet, which is indicated by the hashed area. The trajectory of a reflected ion is also indicated (b)

If at very high energy both nuclear stopping and the contribution of low-velocity electronic stopping to the total pathlength can be neglected, stopping scales basically with the inverse of the energy (see eqs. (74), (79) and (82)), so that $\overline{R}_t(E) \propto E^{-2}$.

When nuclear stopping dominates, only approximate analytical solutions can be obtained. For power-law scattering (see eq. (57)), the universal result reads in reduced Lindhard-Scharff units [49]

$$\bar{\rho}_t(\varepsilon) = \frac{(s-1)}{\lambda_s}\varepsilon^{2/s} \tag{148}$$

where s denotes the power-law exponent and λ_s a constant which is calculated from k_s. For an average exponent $s \approx 2$ (see Fig. 6), this results in a proportionality to the incident energy according to

$$\bar{\rho}_t(\varepsilon) = 3.06 \cdot \varepsilon \tag{149}$$

The mean depth of deposition is given by the mean "longitudinal" projected range of the ion (see Fig. 30), which can be significantly shorter than the average pathlength. However, when the influence of angular deflections by nuclear scattering is minor, the mean total pathlength can be taken as good estimate for the mean projected range. This is given in situations where (i) the ion energy is sufficiently high so that most of the slowing-down path is dominated by electronic stopping with its negligible angular deflections of the ion, or (ii) when the mass of the ion is large compared to the target mass, so that the angular deflections in nuclear scattering remain small.

In general, transport calculations have to be performed in order to determine the depth distribution of ions being implanted into a solid. Let us write the distribution of the longitudinal projected range as $f_R(x, E, \vec{\eta})$ where x denotes the depth and E and $\vec{\eta}$ the energy and direction of incidence, respectively. $f_R(x, E, \vec{\eta})\,\delta x$ gives the probability that an ion comes to rest at a depth between x and $x + \delta x$

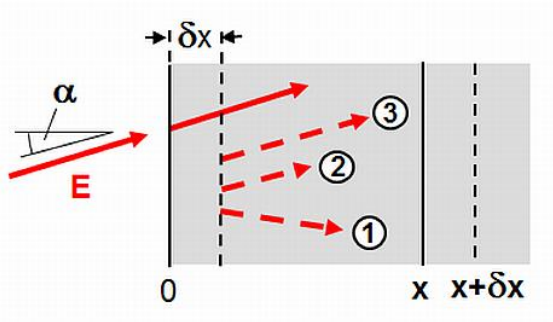

Fig. 31. Schematic of the "backward" transport formalism for the analytical calculation of projected range distributions, for an ion incident at an energy E and an angle α with respect to the surface normal. In the differential subsurface layer denoted by its thickness δx, the ion can undergo a nuclear (1) or electronic (2) collision, or it can just be transmitted (3). See text for further explanation

The differential-integral equation governing f_R [12,13,49] can be derived from the scheme displayed in Fig. 31. Consider a subsurface differential depth element δx. There are three possibilities for an ion traversing δx: (1) a nuclear collision might take place which alters the energy and the direction of the ion; (2) an electronic collision might occur which alters the energy but not the direction; (3) the ion does not undergo any collision. Then, the range distribution at $x + \delta x$ is composed from three sets of distributions with different parameters and probabilities according to (1)-(3), but taken at the depth x, as the medium, assumed to be homogeneous, can be translated by δx. This reads

$$\begin{aligned} f_R(x+\delta x, E, \vec{\eta}) = {} & \frac{n\delta x}{\cos\alpha}\int d\sigma_n(E, \vec{\eta} \to E', \vec{\eta}')\, f_R(x, E', \vec{\eta}') \\ & + \frac{nZ_2\delta x}{\cos\alpha}\int d\sigma_e(E, \vec{\eta} \to E - \Delta E, \vec{\eta})\, f_R(x, E - \Delta E, \vec{\eta}) \\ & + \left(1 - \frac{n\delta x}{\cos\alpha}\int d\sigma_n - \frac{nZ_2\delta x}{\cos\alpha}\int d\sigma_e\right) f_R(x, E, \vec{\eta}) \end{aligned} \tag{150}$$

with the nuclear and electronic differential scattering cross sections $d\sigma_n$ and $d\sigma_e$, respectively, the electronic energy transfer ΔE, and the angle of incidence α with respect to the surface nor-

mal. Expanding the left-hand side in x and the last term of the second line in E, which allows to introduce the electronic stopping cross section according to eq. (51), results in the Boltzmann-type transport equation

$$\begin{aligned}\frac{1}{\cos\alpha}\frac{\partial f_R}{\partial x}(x,E,\vec{\eta}) &= -nS_e(E)\frac{\partial f_R}{\partial E}(x,E,\vec{\eta}) \\ &+ n\int d\sigma_n(E,\vec{\eta}\to E',\vec{\eta}')\left(f_R(x,E',\vec{\eta}')- f_R(x,E,\vec{\eta})\right)\end{aligned} \tag{151}$$

The transport equation is solved most conveniently in an infinite medium with the ion starting at $x=0$. Then, the direction of incidence is not distinguished. The normalization condition reads

$$\int_{-\infty}^{\infty} f_R(x,E)\,dx = 1 \tag{152}$$

As an artifact of the treatment in the infinite medium, a fraction of the range distribution may extend into the negative half space due to backscattering (see Fig. 30). The probability that an incident ion becomes backscattered is denoted as the reflection coefficient r, which can be approximated by

$$r = \int_{-\infty}^{0} f_R(x,E)\,dx \tag{153}$$

This holds only approximately, as the theory allows multiple crossing of the $x=0$ plane in the infinite medium, whereas in reality a backscattered particle is lost after the first transition. This is a general problem of the analytical transport theory when being applied to a finite medium. Also the definition of the longitudinal mean projected range by

$$\overline{R}_p^{=}(E) = \int_{-\infty}^{\infty} f_R(x,E)\,x\,dx \tag{154}$$

suffers from this problem.

Different mathematical procedures have been adopted to solve eq. (151)[12,13,47,49,125,126,72,127]. Conveniently, the solution proceeds via the moments of order ν of the distribution function given by

$$f_R^{(\nu)}(E) = \int_{-\infty}^{\infty} f_R(x,E)\,x^{\nu}\,dx \tag{155}$$

The first moment is the mean range (eq. (154)) at a given energy. The second moment describes the width of the distribution. It is connected to the standard deviation $\sigma_p^{=}$ of the distribution, which is denoted as the (longitudinal) "range straggling", through

$$\left(\sigma_p^{=}(E)\right)^2 = \int_{-\infty}^{\infty} f_R(x,E)\left(x-\overline{R}_p^{=}(E)\right)^2 dx = f_R^{(2)}(E) - \left(\overline{R}_p^{=}(E)\right)^2 \tag{156}$$

Eq. (151) turns then into a system of equations for the recursive calculation of the subsequent moments.

Based on these concepts, simple expressions for the relation between the mean projected range and the mean total pathlength have been derived for special cases. For heavy ions in light substances, where the ion trajectories are comparatively straight in average, Lindhard et al.[12] derived for power-law scattering (see eq. (44)) and $m_1 >> m_2$

$$\frac{\bar{R}_p^{=}(E)}{\bar{R}_t(E)} = \left(1 + \frac{m_2}{m_1}\frac{s^2}{4(2s-1)}\right)^{-1} \approx \left(1 + \frac{m_2}{3m_1}\right)^{-1} \tag{157}$$

where the latter term holds for the exponent $s \approx 2$ in the nuclear stopping regime (see Fig. 6). For the opposite case of light ions, Schiøtt[125] obtained

$$\frac{\bar{R}_p^{=}(E)}{\bar{R}_t(E)} = \lambda(1-2\lambda); \qquad \lambda = \frac{m_1}{m_2}\frac{S_e(E)}{S_n(E)} \tag{158}$$

which requires $\lambda < 0.5$, and is restricted to an energy regime where electronic stopping dominates, i.e. $S_n < S_e$.

The full shape of the distribution function is obtained by reconstruction from the leading moments, as, e.g, using a set of a Gaussian function and its derivatives. An example for light ions has been given by Weissmann and Sigmund[126]. As shown in Fig. 32, the distributions peak at higher energies far from the surface with a negligible "overhang" to negative depth. At $\varepsilon \approx 1$, however, the negative depth fraction becomes significant, so that the prediction of the distribution near the surface becomes doubtful. For the present case, Gaussian functions resulting from the moments up to order 2 are already a very good approximation, with only minor corrections by the third moment.

Thus, for practical purposes, the range distributions can be approximated in many cases by Gaussian functions with mean values and standard variations taken from transport theory. Corresponding predictions can be conveniently obtained again from the SRIM software package[69], which contains a transport equation module[128] to calculate the mean longitudinal projected range as described above and its straggling, and in addition the straggling $\sigma_p^{\perp}$ of the lateral range distribution, the mean value of which trivially vanishes (see Fig. 30).

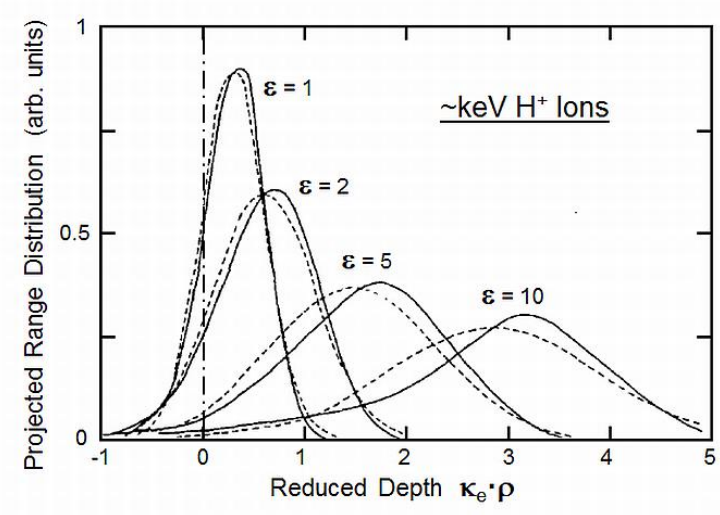

Fig. 32. Projected range distributions from analytical transport theory, for hydrogen ions in heavy targets at different energies in the keV range, denoted by the reduced energy according to eq. (38). The depth scale is given in terms of the reduced length according to eq. (53) times the constant of low-energy electronic stopping in reduced units, $(-d\epsilon/d\rho)_e = \kappa_e\sqrt{\varepsilon}$ (see eq. (66)). The dotted lines represent Gaussian distributions resulting from the first two moments of the distributions (see text), whereas the solid-line distributions include the third moment and thereby the skewness of the profiles. (After ref.[126])

For the practical situation of broad-beam implantation, the range distribution in direction normal to the surface is of interest (see Fig. 30). At normal incidence, it is identical to the longitudinal range distribution as described above. At oblique incidence, the mean range in direction of the surface normal incidence can be roughly calculated from the mean longitudinal range according to

$$\overline{R}_p(\alpha) = \overline{R}_p(\alpha = 0)\cos\alpha = \overline{R}_p^{=}\cos\alpha \tag{159}$$

Similarly, the range straggling is obtained from the longitudinal and lateral straggling as

$$\left(\sigma_p(E)\right)^2 = \left(\sigma_p^{=}(E)\right)^2 \cos^2\alpha + \left(\sigma_p^{\perp}(E)\right)^2 \sin^2\alpha \tag{160}$$

Eqs. (159) and (160) hold well if the resulting range distribution does not cut the surface significantly.

7.2 Computer Simulation

Once the basic principles and relations being established by analytical theory, it is obvious that any refinements can be better accomplished by computer simulation. For ion ranges as indicated above, the analytical theory suffers in particular from a poor description of ion scattering near the surface when ion reflection becomes significant. This, e.g, sets a limit to the applicability at glancing angles of incidence. Other complications arise, e.g., for the description of ranges in compounds, with non-planar or structured surfaces, or for inhomogeneous bulk materials such as layered structures. All such limitations can be overcome when applying computer simulation. In addition, the latter can be applied to crystalline materials, and they are more flexible with respect to the model parameters, such as the definition of electronic stopping or of the energy parameters as described in sect. 6.1.

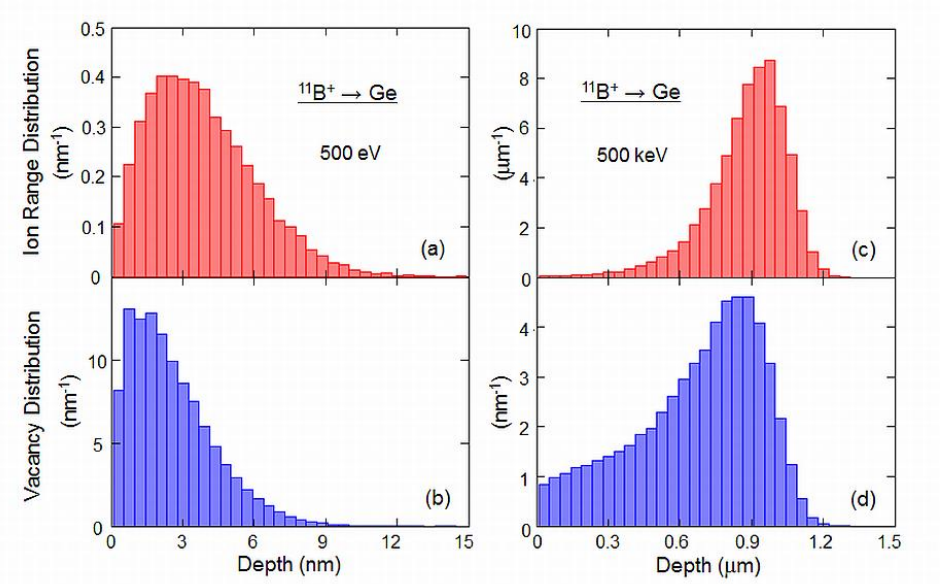

Fig. 33. Range and damage distributions for boron ions incident on germanium at normal incidence and two different energies, as simulated by TRIM[69] with 20000 ion trajectories. (a,b) 500 eV, calculated in the monolayer collision mode. The reflection coefficient is 24%. 11.5 vacancies are produced per incident ion. (c,d) 500 keV, calculated in the quick damage production mode. The reflection coefficient is negligible (<0.5%). 890 vacancies are produced per incident ion.

BCA computer simulation can be considered as a direct refinement of analytical theory in the sense that both rely on the binary collision approximation (see sect 6.1.3). Whereas analytical range theory is exclusively valid for random media, BCA computer simulations can be adjusted to treat random, amorphous and crystalline media. For the fast simulation of ion range distributions in amorphous media, the TRIM code is most widely accepted, being available with the SRIM package[47,69]. The range distributions result as the depth distributions of the endpoints of the ion trajectories as shown in Fig. 26 (a,c). Fig. 33 shows selected results obtained from TRIM for

largely different energies. At low energy of incidence, the range distribution cuts the surface with a significant fraction of reflected ions (Fig. 33(a)). In contrast, reflection becomes negligible at high energy, and a highly asymmetric distribution is obtained tailing towards the surface (Fig. 33(b)).

BCA range simulations are rather fast (the examples of Fig. 33 take a few minutes on a standard personal computer). Ranges and range distributions obtained from TRIM are generally very reliable with a precision of around 5-10% for the mean ranges. There are, however, cases where the program uses inaccurate stopping cross sections (see subsection 4. 6.2). In such rare cases, deviations from experimental data of several 10% may occur.

The description of range distributions in crystalline material turns out to be rather complicated. Even if the ion beam enters a crystal ideally along a channeling direction (see sect. 5), large-angle scattering will always occur at the heading atoms of the atomic strings or planes, which leads into random trajectories and forms a random fraction of the projected range distribution. Ions with less close encounters at the surface may enter channeling trajectories with relatively large oscillation amplitude, so that the probability of being dechannelled during the first few oscillations becomes relatively large. This will add another random fraction which, however, is displaced to a larger depth. The remaining channeling fraction may exhibit significantly enhanced pathlengths due to reduced stopping. This may, e.g., result in long tails towards the bulk and even in double-peak profiles (see, e.g., ref[129].).

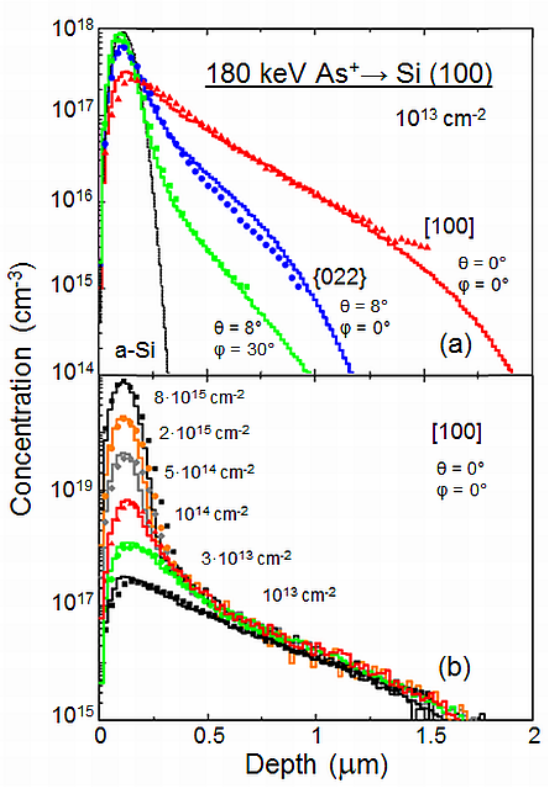

Fig. 34. Range distributions of As ions implanted into monocrystalline Si at low ion fluence (a) for different angles of incidence, and for increasing fluence (b) demonstrating the effect of damage buildup (see sect. 10.3). Experimental data (symbols) are from secondary ion mass spectrometry[131], the corresponding histograms from Crystal-TRIM[90] BCA computer simulation with a special empirical algorithm for damage buildup[101]. The data in (a) relate to different crystal orientations with respect to the direction of the ion beam; the simulated profile for amorphous Si is included for comparison. θ and φ denote the angles of wafer tilt and rotation during implantation, respectively. (After ref.[130])

In view of these complications, computer simulation is the only way to reasonably predict range distributions in crystalline material. An example is given in Fig. 34(a)[130]. The distributions predicted by Crystal-TRIM[90] are found to reproduce the experimental data very well even down to the low-concentration tails of the profiles. For comparison, the simulated profile in the amorphous material is shown. The bombardment along the axial [100] direction results in an extreme broadening of the profile with a significantly increased mean range. In order to avoid channeling, a tilt angle of ~7° with respect to the low-index direction is commonly used, which is sufficiently large compared to the critical angle of channeling (see sect. 5.1) and sufficiently far from other low-indexed axial directions. However, even with this tilt and when planar channel-

ing is avoided, the profile deviates significantly from the prediction for the amorphous material, and depends on the azimuthal rotation of the implanted wafer. A particularly long tail arises at a sample rotation angle which opens the {220} plane for channeling.

Fig. 35 shows results obtained from crystalline BCA simulations for low-energy hydrogen bombardment of Ni[132]. The profile for the amorphous medium is again significantly shallower as compared to the crystalline one. Although the ions are implanted at 10° tilt which largely avoids axial channeling, both the single-crystalline and the poly-crystalline mode of the simulation (see subsection 6.1.1) yield a double-peak structure for the undamaged material, which arises from planar channeling. This is not observed in the experiment (not shown). However, when introducing a small amount of interstitial atoms and vacancies into the crystal, the end-of-range peaks disappear and the profile broadens, and the profile for the polycrystal simulation is in excellent agreement with the experimental result. This confirms that the ions partially enter channeling trajectories by scattering at interstitial target atoms, which contributes to the broadening of the range distribution.

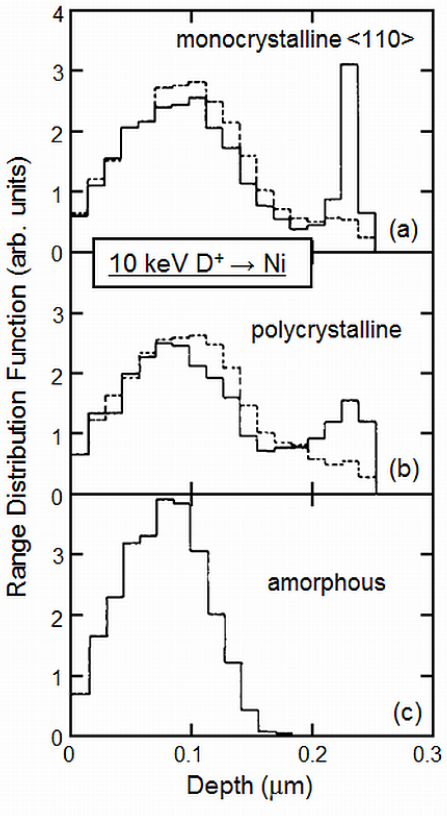

Fig. 35. Range distributions of 10 keV deuterons in nickel incident at 10° with respect to the surface normal, as generated by MARLOWE[15,82] (version 10.9) in single-crystalline (a), polycrystalline (b) and amorphous (c) mode. The single-crystalline distribution has been averaged from 10 simulations at different azimuthal angles of incidence. Solid lines relate to perfect crystals, whereas the dashed lines have been obtained for an assumed randomly distributed Frenkel pair concentration of 0.5%. (After ref.[132])

Molecular dynamics simulations have also been employed for the calculation of ion ranges. As stated in sect. 6, they do not require any definition of parameters which are necessary in BCA simulations (except for electronic stopping which is introduced in a similar way). Thus, provided the chosen interaction potential is sufficiently realistic, they should be generally more reliable, at, however, a significantly lower computational speed. In order to reduce computer time, it is sufficient to address only the primary collisions in MD range simulations, unless at very low ion energies the regime of multiple interaction is entered. Comparisons between MD and BCA[133-135] simulations for irradiation of Si with different ions at sub-keV to 50 keV energies, and a related round-robin study of energy distributions after transmission of keV ions through a few monolayers of different solids[136] reveal some differences even at energies of several 10 keV. However, they do not question the validity of the BCA simulations in this energy regime within the expected accuracy (see above). Hobler et al.[135] find at energies around 100 eV good agreement between MD simulations and suitable BCA simulations even in the details of the

three-dimensional deposition contour, as shown in Fig. 36. Partial channeling into [110] directions is clearly visible. As expected, there is a tendency of increasing deviation towards the lowest energy of 50 eV, which approaches the validity limit of the BCA simulation.

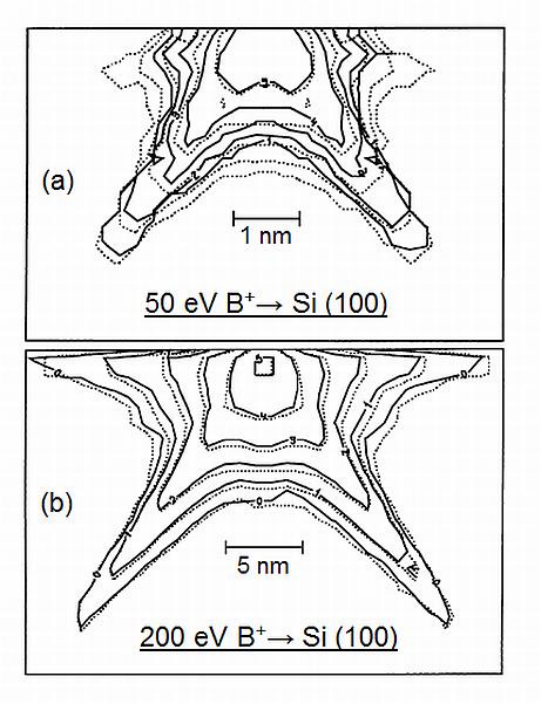

Fig. 36. Logarithmic lateral contour plot of the deposition probability of 50 eV (a) and 200 eV (b) boron ions at normal incidence onto a (100) silicon crystal. The point of incidence is the midpoint of the upper borderline of each frame. The solid and dotted lines show the results from MD and BCA simulations, respectively. (After ref.[135])

7.3 High-Fluence Ion Implantation

In the preceding sections, range distributions have been addresses which represent the probability that an incident ion comes to rest at a certain depth in a given material. For a continuous ion beam of fluence Φ, the volume concentration c_i of the implanted species grows initially according to

$$c_i(x,\Phi) = f_R(x)\cdot\Phi \tag{161}$$

This holds only for small fluences and if any density changes can be neglected. At large fluence, the simple scaling of eq. (161) would result in excessively high concentration. For many materials, the concentration is limited by the takeup ability of the host, such as by stoichiometric limits or by a maximum concentration of a gaseous species. This can be accounted for in the simple model of "local saturation", which assumes that any atom which is implanted into a region where the maximum concentration has already been reached, is immediately released from the substance. Then, the profile evolution with a maximum concentration $c_i^{\max}$ is given by

$$c_i(x,\Phi) = \begin{cases} f_R(x)\cdot\Phi, & c_i < c_i^{\max} \\ c_i^{\max} & else \end{cases} \tag{162}$$

An example is shown in Fig. 37(a). Additionally, high-fluence implantation profiles are influenced by a number of effects which cannot easily be accounted for in a simple analytical model. The presence of the implanted species influences the stopping and scattering of the incident ions so that the range profiles may be changed during the implantation. This may lead to a distortion of the implantation profiles in addition to the distortion which is caused by the relaxation of the host matrix (as, e.g. swelling due to the implanted atoms). Such mechanisms are covered by dynamic BCA computer simulation (see subsection 6.1.4). The model of local saturation can be in-

corporated into the simulation, by limiting the maximum concentration of the implanted species. A corresponding result from a TRIDYN[93,102,103] calculation is shown in Fig. 37(b). In comparison with the simple analytical approach, already the profile at the lowest fluence is broadened due to swelling. Towards the highest fluences, there are additional effects of sputtering which will be discussed in sect. 9.4.

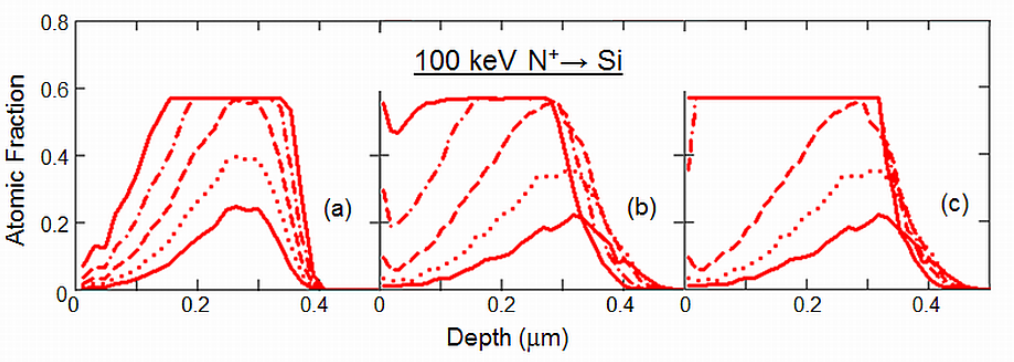

Fig. 37. Implantation profiles under local saturation, for 100 keV nitrogen implanted into silicon with a maximum atomic fraction of 0.571 corresponding to Si_3N_4. The increasing fluences are $2.5 \cdot 10^{17}$ cm^{-2} (solid line), $5 \cdot 10^{17}$ cm^{-2} (dotted line), $1 \cdot 10^{18}$ cm^{-2} (dashed line), $2 \cdot 10^{18}$ cm^{-2} (dashed-dotted line) and $4 \cdot 10^{18}$ cm^{-2} (solid line). (a) Simple scaling of the range profile according to eq. (162), with the range profile taken from TRIM[69] (version 2000-39). (b) From TRIDYN[93,103] simulations including range broadening and sputtering. The nitrogen peak at the surface is due to preferential sputtering (see sect. 9.3). (c) From TRIDYN simulations with a simple diffusion model (see text)

TRIDYN further offers a simplistic algorithm of diffusion in case of local saturation, by which excess atoms that are deposited in the saturated regions are transferred to the nearest non-saturated profile edge rather than being discarded. The result is shown in Fig. 37(c), with considerable additional broadening towards the surface for the highest fluences. The applicability of the above models depends critically on the properties of the system being under investigation.

8 Cascades and Spikes

In the previous chapters, mainly the fate of the ion impinging onto the solid surface has been considered. We will now address the response of the target atoms to the ion irradiation. The energy deposition around the ion trajectory leads to a local increase of the kinetic energy of the surrounding target atoms, which may either directly result from nuclear collisions, or indirectly from a primary energy transfer to electrons, which then couple to the lattice by electron-phonon interaction.

A schematic classification of the corresponding regimes is shown in Fig. 38. If the energy of the incident ion is primarily dissipated by nuclear interaction, a dilute collision cascade may be created (Fig. 38(a)), where binary collisions between moving atoms and atoms at rest dominate. In this “linear cascade” regime, the overall effect of the cascade results from a linear superposition of the effects of the individual recoil atoms. Thus, for energies being larger than about 10 eV (see subsection 6.1.3), the binary collision approximation can be applied in either analytical collisional theory or BCA computer simulation. In contrast, at sufficiently high energy density deposited by nuclear interaction, an ensemble may be created where most collisions take place between moving atoms (Fig. 38(b)), which results in a quick thermalization at high temperature.

Subsequently, this so-called elastic thermal spike cools down by interaction with the surrounding material according to the laws of thermal diffusion. Consequently, diffusional models are applied for the analytical description. However, also MD computer simulation is well suited for this regime.

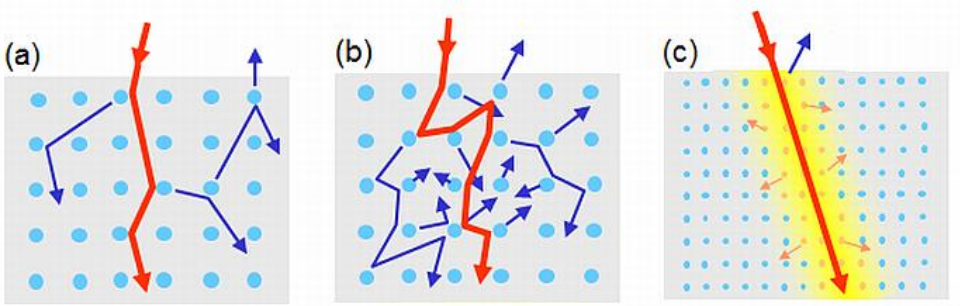

Fig. 38. Collision cascade and thermal spike regimes: (a) linear collision cascade; (b) non-linear collision cascade and associated elastic thermal spike; (c) inelastic thermal spike induced by high electronic stopping

It is important to note that also the linear cascade will develop into an elastic thermal spike. This thermalization, however, may occur at a mean energy which is below the range of interest, if, e.g., phenomena shall be described which appear only above certain energy thresholds – see sects. 9 –11).

At sufficiently high ion energy, the energy is mainly dissipated into electronic collisions which initially create a hot local electron gas (Fig. 38(c)). By electron-phonon interaction, this may partly transfer its energy to the atomic system. In this so-called inelastic thermal spike, the coupled electron and atomic ensembles dissipate their kinetic energy again according to diffusion laws.

8.1 The Linear Cascade

Depending on the incident energy and the species of the incident ion and the target atoms, there is a wide range of cascade morphologies even in the regime of the linear cascade, as schematically indicated in Fig. 39. A cascade may be comparatively dilute in the case of light ion incidence associated with small primary energy transfers, which may result in a number of small subcascades along the ion trajectory (Fig. 39(a)). Denser subcascades may be formed during high-energy heavy ion bombardment, when the low nuclear collision cross section allows only a few primary collisions with high energy transfer. In these situations, an average cascade volume for a single incident ion cannot easily be defined; however, the average over many ion trajectories results in a continuously filled average volume. In contrast, for the dense cascade depicted in Fig. 39(b), which typically occurs with similar ion and target masses in the nuclear stopping regime, similar volumes are filled by each incident ion, so that the average cascade volume is essentially defined by a single ion event.

The analytical description of the linear cascade follows similar transport concepts as described above for ion ranges (see sect. 7). An elaborate treatment is given in refs.[22-24], from which only the main assumptions and results will be reproduced here. During the dissipation of the collisional cascade in space and time, subsequent generations of recoils contain increasing numbers of moving atoms at decreasing energies, so that low-energy recoils will largely dominate the total number. As these do not remember the original direction of ion incidence, the cascade can be considered as isotropic. Then, the cascade for one incident ion can be described by a distribution function F which is defined in such a way that

$$dN(E,\vec{\eta},E_0,\vec{r}) = F(E,\vec{\eta},E_0,\vec{r})dE_0 d^3\vec{r} \tag{163}$$

describes the probability to find a cascade atom with a start energy between E_0 and $E_0 + dE_0$ in the volume element $d^3\vec{r}$ around the position vector $\vec{r}$, for an ion incident at $\vec{r} = 0$ in direction $\vec{\eta}$ (see ch. 5) and at energy *E*.

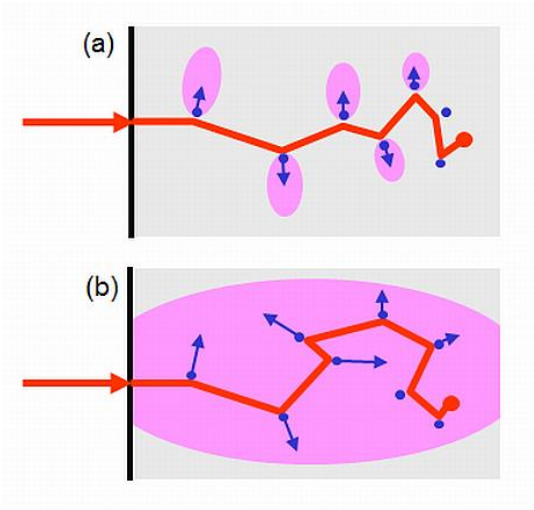

Fig. 39. Collision cascade structures resulting from a single incident ion (schematic): (a) small subcascades occuring typically at light ion irraditation; (b) dense cascade at high nuclear stopping, in particular at similar masses of the ion and the target atoms

For brevity, the transport equation governing *F* is not detailed here. Again, it can be solved for an infinite medium by the definition of moments (see eq. (155)). Obviously, *F* vanishes at cascade atom energies above the energy of ion incidence, i.e.

$$F(E,\vec{\eta},E_0,\vec{r}) = 0; \quad E_0 > E \tag{164}$$

As indicated above, high-energy recoils contribute to the cascade distribution function only to a minor extent, so that a formal extension of *F* to infinite energies E_0 will imply only a small error. Doing so for the higher moments ($\nu > 0$) of the distribution function, the space and energy variables can be separated resulting in a factorization of the cascade distribution function according to

$$F(E,\vec{\eta},E_0,\vec{r}) = CF_D(E,\vec{\eta},\vec{r})F_E(E,E_0) \tag{165}$$

where F_E, which is denoted as recoil density, represents the distribution of the start energies of the cascade atoms. The energy deposition distribution function F_D describes the spatial deposition of kinetic energy within the cascade. For reasons to be addressed in ch. 10, it is often called the "damage distribution" function. *C* is a normalization constant. Eq. (165) implies that the energy distribution is independent of the position in the cascade, which is obviously an approximation, as outer zones of the cascade volume contain less energetic recoil atoms than the zone directly around the ion trajectory.

Being finally interested in atomic relocations within the cascade, it is appropriate to consider only the energy which is dissipated into atomic motion rather than by electronic stopping. An appropriate definition of the corresponding energy distribution function can only include the energy transfer from the ion to primary recoils. Otherwise, as any primary recoil distributes its energy in subsequent nuclear collisions to higher generations of recoils, the summation of the energy transfers in all recoil generations would count energy of the same origin in a manifold way. This restriction to primary recoils, however, implies that the ranges of the recoils are small compared to the spatial extension of the cascade, which appears to be mostly justified as the ranges of the recoil atoms will be mostly significantly smaller than the range of the incident ion. Nevertheless, deviations from this rule are expected as, e.g., for similar ion and target masses, in

particular for oblique incidence with the corresponding reduction of the projected ion range. This latter situation, however, would not be realistically described by the infinite medium approximation (see ch. 7) anyway.

The volume integral of the energy distribution function

$$\nu_D(E) = \int F_D(E, \vec{\eta}, \vec{r}) d^3\vec{r} \tag{166}$$

yields the fraction $\nu_D(E)$ of the initial ion energy which is dissipated into atomic motion of the cascade atoms (rather than in electronic collisions). $\nu_D(E)$ is often denoted as "damage energy".

As most cascade atoms move at low energy where electronic stopping is small compared to nuclear stopping, the relative fraction $\nu_D(E)/E$ is generally close to unity. Quantitative predictions can be obtained from the transport equation

$$\begin{aligned} &\int d\sigma_n(E \to E-T)\left(\nu_D(E) - \nu_D(E-T) - \nu_D(T)\right) \\ &\qquad = -S_e(E)\frac{\partial \nu_D}{\partial E}(E) \end{aligned} \tag{167}$$

which is formally similar to eq. (151) without, however, the dependence on depth but containing an additional recoil term. The results of numerical solutions[137] are shown in Fig. 40 for different constants of low-energy electronic stopping. For the small recoil energies which dominate the linear cascade,

$$\nu_D(E) \approx 0.9 \cdot E \tag{168}$$

can be taken as a reasonable approximation.

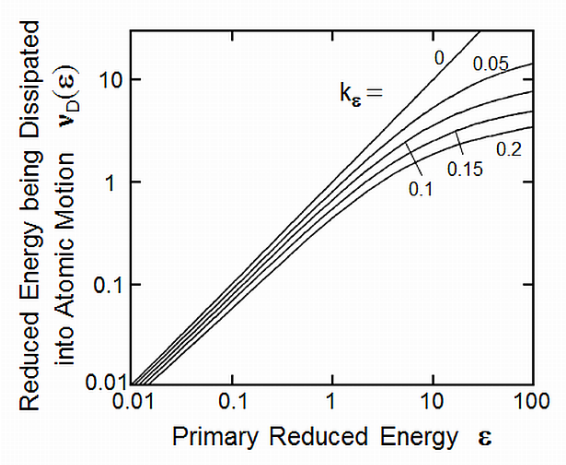

Fig. 40. Fraction of the kinetic energy of an ion or a primary recoil which is not dissipated into electronic stopping, versus the reduced primary energy. The results apply to equal ion and target masses. k_ε denotes the low-energy electronic stopping constant so that $(-d\epsilon/d\rho)_e = k_e\sqrt{\varepsilon}$ (see section 4.3.2). (After ref.[137])

The energy deposition distribution can then be calculated in analogy to the calculation of the ion range distribution. Similarly, the spatial distribution of energy being dissipated into electronic collisions can be obtained. A qualitative display of a typical result is shown in Fig. 41[138] for an ion which enters the solid surface at an energy below the maximum of electronic stopping, where, however, electronic stopping is still largely dominating (see sect. 4.3). The ion is first slowed down mainly by electronic collisions with a negligible probability of significant energy transfer in nuclear collisions. The electronic energy deposition initially decreases according to the decrease of electronic stopping at decreasing ion velocity. After about half the total range, nuclear energy transfer becomes significant, and the spatial regime of the collision cascade is entered. Before the ion comes to rest, the electronic energy deposition per unit depth increases again due to multiple scattering of the ion and the numerous small contributions from the colli-

sion cascade. The "damage" distribution peaks at lower depth than the range distribution, as the nuclear energy transfers become small towards the end of the ion range.

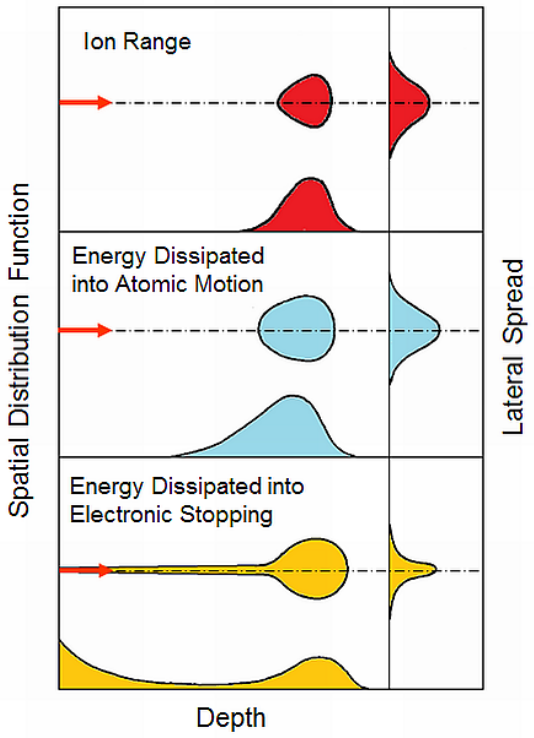

Fig. 41. Characteristic three-dimensional deposition functions of an ion at normal incidence (schematic), displayed as a contour cut (centre of the individual frames), and as a projection in the plane of incidence (bottom), and a projection onto the plane normal to the direction of incidence (right). The distributions of energy dissipated into atomic motion and dissipated by electron stopping are often denoted as "damage" and "ionization" distributions, respectively. (After ref.[138])

Again using a suitable transport equation and employing a power-law potential for the nuclear scattering cross section (eq. (47)), the recoil density F_E can be calculated analytically if electronic stopping is neglected. As one may expect, the resulting formula scales with the initial energy E. Afterwards, the neglect of electronic stopping is heuristically compensated by replacing E by $\nu_D(E)$, so that the result becomes

$$F_E(E,E_0)=\frac{s^{-1}}{\Psi(1)-\Psi(1-s^{-1})}\frac{\nu_D(E)}{E_0^2} \tag{169}$$

where s is the power-law exponent and $\Psi(\xi)=d(\ln\Gamma(\xi))/d\xi$ the derivative of the logarithm of the gamma function. Eq. (169) holds for energies $E_0 \ll E$, and thus describes the vast amount of the cascade atoms unless the energy of incidence is extremely low. Towards low energy, the appropriate power-law exponent increases to $s \gg 1$ as mentioned in sect. 3.2. For $s \to \infty$, the first term in eq. (169) equals $1/\Psi'(1)=6/\pi^2$, resulting in

$$F_E(E,E_0)=\frac{6}{\pi^2}\frac{\nu_D(E)}{E_0^2} \tag{170}$$

The recoil density cannot readily be normalized as the normalization integral diverges for $E_0 \to 0$. However, we recall that the linear cascade regime only applies to recoil energies above a certain threshold E_{th}. The applications of the linear cascade model to be discussed in chs. 9 – 11 will require the definition of a characteristic threshold energy as well, which can be formally used for normalization. If both the total cascade distribution function F and the recoil density F_E are normalized to one, the combination of eqs. (165), (166) and (170) results in

$$F\left(E,\vec{\eta},E_0,\vec{r}\right)=\frac{6}{\pi^2}\frac{F_D\left(E,\vec{\eta},\vec{r}\right)}{E_0^2} \tag{171}$$

For the computer simulation of the development of collisional cascades in the linear regime, both BCA and MD codes have been used. The example shown in Fig. 42[139] displays the temporal development of collision cascades in copper. Initially, high-energy recoils are generated which dominate the early stage of the cascade, from which atoms with lower energy evolve. With a time constant of ~50 fs, the cascade develops towards the maximum number of atoms moving with a start energy above a few eV. Due to the shorter slowing-down time of the ion, the time constant is slightly shorter at the lower ion energy. The decay time constants are between 50 fs and 100 fs. Except for some deviations in the decay phase, the results from the BCA and MD simulations are in good agreement. Although this might be partly attributed to the choice of the simulation parameters, it is surprising that the BCA simulation appears to work well down to energies of ~1 eV, which is clearly below the expected validity range of the binary collisions approximation.

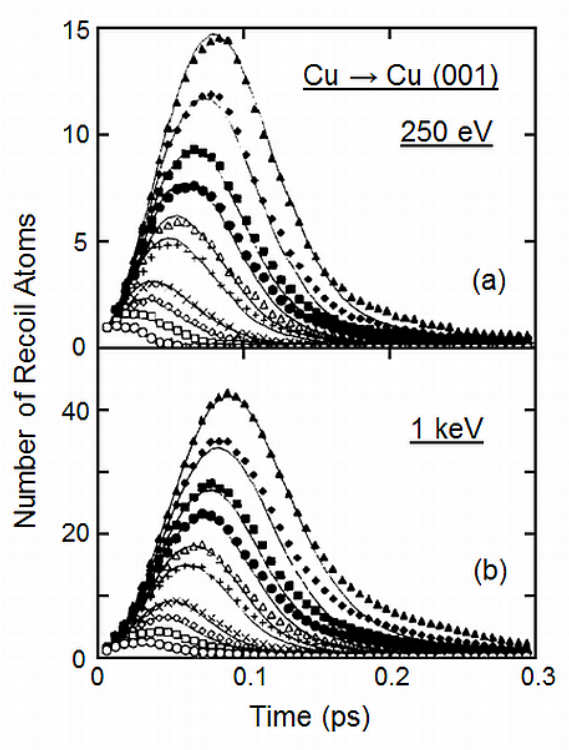

Fig. 42. Development of a collision cascade as function of time after projectile incidence, as calculated from MD (symbols) and BCA (lines) computer simulation, for self-irradiation of copper at 250 eV (a) and 1 keV (b). The results display the instantaneous number of recoils with a start energy E_0 above different threshold energies of 1 eV (full triangles), 2 eV (full diamonds), 3.5 eV (full squares), 5 eV (full circles), 7.5 eV (open triangles), 10 eV (upright crosses), 20 eV (diagonal crosses), 30 eV (open diamonds), 50 eV (open squares) and 100 eV (open circles). (After ref.[139])

8.2 Thermal Spikes

Thermal spike models describe the temporal and spatial development of a temperature field $T(r,t)$ as function of position r and time t which is induced by the energy deposition of the ion. At sufficiently high ion mass and/or energy, the ion trajectory can be approximated by a straight line, along which energy is deposited in primary collisions according to the stopping force. From this, an axially symmetric thermal spike develops for a sufficiently fast ion. Neglecting the stationary temperature of the solid before ion incidence, the initial balance of energy per unit volume along the trajectory reads with the mass density ρ and the specific thermal capacity c

$$\left|\frac{dE}{dx}\right|\delta^2(r)=\rho cT(r=0,t=0) \tag{172}$$

where $\delta^2(r)$ denotes the two-dimensional delta function.

The radial dissipation of energy is described by the equation of heat conduction in cylindrical geometry,

$$\frac{\partial}{\partial t}T(r,t)=\frac{1}{r}\frac{\partial}{\partial r}\left(r\kappa(T(r,t))\frac{\partial T(r,t)}{\partial r}\right) \tag{173}$$

where $\kappa=\lambda/\rho c$ denotes the thermal diffusivity with the thermal conductivity λ. If the thermal diffusivity is independent on temperature, the solution is with the initial condition of eq. (172)

$$T(r,t)=\left|\frac{dE}{dx}\right|\frac{1}{4\pi\lambda t}\exp\left(-\frac{r^2}{4\kappa t}\right) \tag{174}$$

8.2.1 Elastic Thermal Spike

For the consistent treatment of the elastic thermal spike, the thermal diffusivity of a gas of hot atoms can be described in terms of atomic collisions as addressed in ch. 2, which results in[140,141]

$$\kappa=\frac{C_\kappa}{n}\sqrt{\frac{kT}{\pi m_2}} \tag{175}$$

with a constant $C_\kappa=45$ nm^{-2}. Further, applying the Dulong-Petit rule $c=3k/2m_2$, the solution of (173) becomes with the abbreviation $\chi=\sqrt{k/\pi m_2}\cdot C_\kappa/n$ [141]

$$T(r,t)=\left[\left(\left|\frac{dE}{ndx}\right|\frac{1}{6\pi k\chi t}\right)^{1/3}-\frac{r^2}{12\chi t}\right]^2 \tag{176}$$

if the expression in angular brackets is positive, and 0 otherwise.

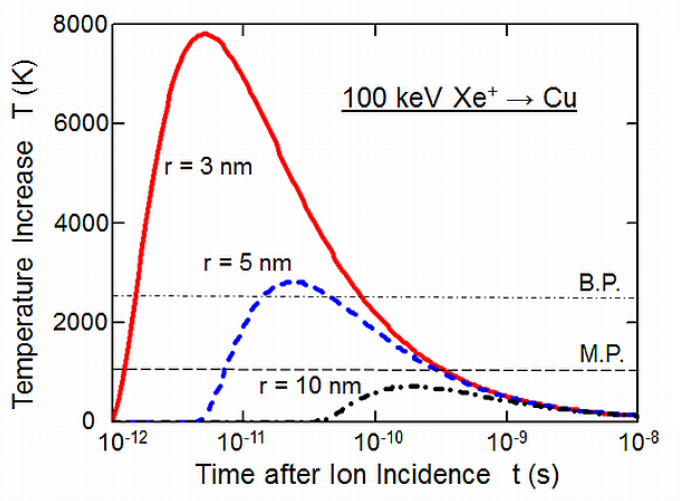

Fig. 43. Development of temperature in an elastic thermal spike at different radial distance *r* from the centre of the trajectory of a single xenon ion in copper at an energy of 100 keV, as calculated using eq. (176). The thin horizontal lines indicate the melting and boiling points of copper, respectively, which are roughly 1060 K and 2540 K above room temperature, respectively

Fig. 43 shows the result for 100 keV xenon incident on copper. At these conditions, nuclear stopping clearly dominates (by a factor of more than 10 compared to electronic stopping; the latter is not taken into account). The thermal spike expands in radial direction from the ion trajectory. At a radius of up to 5 nm, transient temperatures above the boiling point of copper are

reached, whereas at 10 nm the temperature peaks close to the melting point. The relation to the equilibrium phase transition temperatures, however, is rather questionable in view of the extremely short transients. At the radius of 3 nm, the peak temperature is close to 1 eV. However, this radius is close to the mean radius of the primary nuclear collision zone, which can be estimated from BCA computer simulation. Thus, the thermal dissipation model becomes increasingly questionable towards lower radii. At these small radii, also the time scale imposes restrictions to the validity of the model, as times close to the typical duration of thermal lattice vibrations (10^{-13}...10^{-12} s) are not meaningful in terms of heat propagation. Further, times below ~10^{-12} s conflict with the typical slowing-down time of the ions of 10^{-13}...10^{-12} s as well, as the initial energy distribution and the development of the spike are no longer separated in contrast to the assumptions of the model. Nevertheless, some confidence can be attributed to the result at intermediate time at least close to the surface, where any deviation of the cascade morphology from the idealized cylindrical geometry and the implicit neglect of the energy loss along the ion trajectory play only a minor role.

8.2.2 Inelastic Thermal Spike

In the regime of very high electronic stopping, i.e, for heavy ions at energies around the stopping force maximum, nuclear stopping and thereby the primary energy transfer from the ion to the atomic lattice can be neglected. Multiple ionization along the ion track (see Fig. 38(c)) and subsequent Auger cascades may lead to a density of high-energy electrons which is sufficiently high for thermalization in the electronic system. As this occurs on a time scale of about 10^{-15} s, the initial energy deposition is well decoupled from the subsequent transfer of energy to the lattice atoms by electron-phonon interaction and the final dissipation of the atomic motion. This is the basis of the inelastic thermal spike model developed by Toulemonde et al.[142,143] which will be described in the following.

As the ion trajectories are straight in this regime of negligible nuclear scattering, the cylindrical spike geometry as described in the previous section is appropriate. The coupled set of thermal transport equations for the electrons (with the index *e*) and the lattice atoms (with the index *a*) is written in analogy to eq. (173) as

$$n_e c_e \frac{\partial}{\partial t} T_e(r,t) = \frac{1}{r}\frac{\partial}{\partial r}\left(r\kappa_e(T_e)\frac{\partial T_e}{\partial r}\right) - g\cdot(T_e - T_a) + Q_e(r,t) \tag{177}$$

$$n c_a \frac{\partial}{\partial t} T_a(r,t) = \frac{1}{r}\frac{\partial}{\partial r}\left(r\kappa_a(T_a)\frac{\partial T_a}{\partial r}\right) + g\cdot(T_e - T_a) \tag{178}$$

Here, g describes the electron-phonon coupling and Q_e the heat source per unit length, which is supplied to the electronic subsystem. For the latter, a Gaussian pulse in time is assumed according to

$$Q_e(r,t) = C S_e(E) F_e(E,r) \exp\left(-\frac{(t-t_0)^2}{2\sigma_t}\right) \tag{179}$$

where C denotes a normalization constant such that the integration over the radial area and the time yields the electronic stopping cross section. The mean time $t_0 \approx 10^{-15} s$ describes the average time within which the ballistic electrons created by ion-electron collisions deposit their energy. The standard deviation σ_t of the pulse represents the thermal equilibration time of the electrons[144]. The radial distribution function $F_e(E,r)$ describes the energy density transferred from the ion to the ballistic electrons, and is taken from a model which has been developed for particle radiation therapy[145]. The thermophysical constants of eq. (177) are taken from

standard free-electron models. The electron-phonon coupling constant g can be replaced by the mean diffusional free pathlength $\mu_e = \sqrt{\kappa_e / g}$, which remains as a free parameter. The lattice thermophysical constants of eq. (178) are taken from known experimental data. The coupled equation system is then solved numerically.

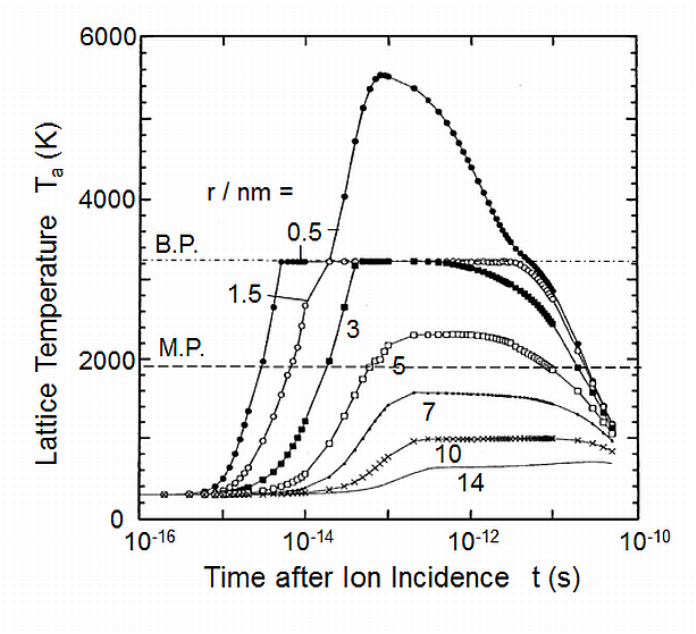

Fig. 44. Development of temperature in an inelastic thermal spike at different radial distance r around the trajectory of a single ion in α-quartz at a stopping force of 22 keV/nm, according to eqs. (177) and (178) for a mean electron diffusional pathlength μ_e = 4 nm and an initial temperature of 300 K. The thin horizontal lines indicate the melting and boiling points of 1972 K and 3223 K, respectively. (After ref.[142])

A result for the irradiation of α-SiO_2 with swift heavy ions is shown in Fig. 44[142]. The latent heats of melting and evaporation have been taken into account for the calculation of the local lattice temperature T_a versus the time after ion incidence. The temperatures calculated at times below ~10^{-13} s must be interpreted as some average kinetic energy in the spike, as thermalization in the lattice does not occur below the characteristic period of lattice vibrations. The electron mean diffusional free pathlength has been chosen to $\mu_e = 4\,\text{nm}$, which fits experimental data of amorphization track radii assuming that amorphization occurs at temperature above the melting temperature.

9 Sputtering

As schematically indicated in Fig. 38, atoms of the irradiated solid may be relocated from their original sites due to the kinetic energy gained in primary or secondary elastic knock-on processes, or in an elastic or inelastic thermal spike. This may result in an ejection from the surface if the energy of the respective atom is sufficiently large to overcome the binding energy at the surface. This is known as sputtering[27-30,146].

9.1 Linear Cascade Sputtering

9.1.1 Analytical Treatment

The analytical theory of the linear cascade (see sect. 8.1) has been rigorously applied to sputtering by Sigmund[20,147]. We recall that the analytical theory assumes an infinite medium with

an isotropic angular distribution of the cascade atoms. For the treatment of sputtering, the surface is introduced a posteriori, which induces anisotropy. In addition, as it will be detailed below, the probability that an atom is sputtered depends on the ejection angle. Therefore, the isotropic distribution over the direction of motion $\vec{\eta}_0$ of the cascade atoms is included in the cascade distribution function (see eq. (171)) which now reads

$$F(E,\vec{\eta},E_0,\vec{\eta}_0,\vec{r}) = \frac{6}{4\pi^3}\frac{F_D(E,\vec{\eta},\vec{r})}{E_0^2} \tag{180}$$

The differential number of cascade atoms, which move at a start energy E_0 into the solid angle $d\omega_0$ in direction $\vec{\eta}_0$ into the halfspace through an arbitrary plane $\vec{f}$ in the cascade volume (see Fig. 45), is then given by

$$d^5N = F(E,\vec{\eta},E_0,\vec{\eta}_0,\vec{r})\vec{\eta}_0 \cdot d\vec{f}\, dE_0 d\omega_0 dx \tag{181}$$

where x denotes the coordinate normal to the plane.

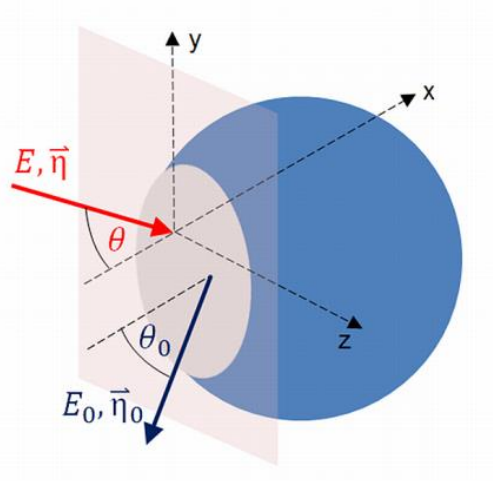

Fig. 45. Collision cascade (schematically indicated by the spherical contour) initialized by an ion at energy E and direction η with an angle θ with respect to the surface normal, and a cascade atom transmitted through a plane at x = 0, with the corresponding characteristics E_0, η_0 and θ_0

The area integral of F_D yields the 1-dimensional distribution of deposited energy as function of depth

$$f_D(E,\vec{\eta},x) = \int F_D(E,\vec{\eta},\vec{r})\left|d\vec{f}\right| \tag{182}$$

Depths larger than an escape depth at given energy, $\Delta x(E_0)$, do not contribute to sputtering. With the escape depth being sufficiently small, f_D can be assumed to be constant and is taken at the position of the plane, x = 0. Then, with the recoil directional angle θ_0 being defined by $\cos\theta_0 = \vec{\eta}_0 \cdot d\vec{f} \Big/ \left|d\vec{f}\right|$, the volume integration of eq. (180) yields the double-differential sputter yield, which represents the number of atoms per incident ion, energy interval and solid angle element which arrive at the plane, according to

$$\frac{d^2Y_s}{dE_0 d\omega_0} = \frac{6}{4\pi^3}\frac{f_D(E,\vec{\eta},0)}{E_0^2}\Delta x(E_0)\cos\theta_0 \tag{183}$$

The escape depth can be estimated from the stopping force as $\Delta x \approx E_0/(dE_0/dx)$. (It should be noted that this can also be derived from a more rigorous treatment of the stationary recoil fluxes due to an incident beam[147].) Further, in consistency with the approximation for the recoil

density, eq. (170), a power-law approximation with $s \to \infty$ is applied for the stopping cross section of the low-energy recoils (see eq. (57)), which results in

$$S_n(E_0) = \frac{\pi}{2} \lambda_0 a^2 E_0 \tag{184}$$

where $\lambda_0 \approx 24$ represents a constant and $a \approx 0.0219$ nm an appropriate universal screening radius. The damage function can be replaced by the nuclear stopping force of the incident ion, taking into account the projection onto the surface normal direction, i.e. $f_D = (dE/dx)_n / \cos\theta$ where the directional vector $\vec{\eta}$ has been replaced by the angle of incidence θ in view of the azimuthal symmetry in the random medium.

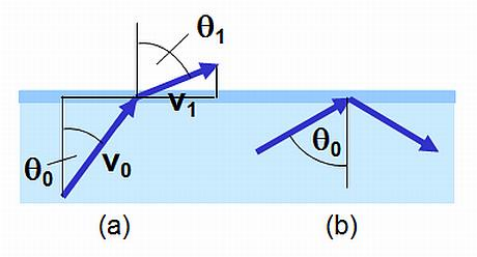

Fig. 46. Transmission (a) and backreflection (b) at a planar surface threshold for small and large subsurface recoil propagation angles θ_0 with respect to the surface normal, respectively. In (a), v_0 and v_1 denote the recoil velocities before and after transmission, respectively, and θ_1 the angle of emission

Identifying now the artificially inserted plane with a real surface, a planar surface binding model is applied with a surface binding energy U_s, which, for monoatomic materials, is identified with the heat of sublimation, which typically lies between ~2 and ~8 eV. This implies a refraction of the trajectory of any transmitted atom (see Fig. 46) with momentum conservation parallel to the surface and total energy conservation, described by

$$\begin{aligned} E_1 \cos^2\theta_1 &= E_0 \cos^2\theta_0 - U_s \\ E_1 \sin^2\theta_1 &= E_0 \sin^2\theta_0 \end{aligned} \tag{185}$$

where E_1 and θ_1 denote the energy and angle of the transmitted atom. Then, transformation of eq. (183) according to eq. (185) yields the energy-angle distribution of the sputtered atoms

$$\frac{d^2 Y_s(E,\theta)}{dE_1 d\omega_1} = \frac{3}{\pi^4} \frac{S_n(E)}{\lambda_0 a^2} \frac{E_1}{(E_1 + U_s)^3} \frac{\cos\theta_1}{\cos\theta} \tag{186}$$

which reproduces the Thompson[148] energy distribution of the sputtered atoms,

$$f_E(E_1) \propto \frac{E_1}{(E_1 + U_s)^3} \tag{187}$$

which is shown in Fig. 47. f_E is independent of the species and the energy of the incident ion. As shown by differentiation, it peaks at an energy $E_1^{\max} = U_s/2$. The mean energy of the sputtered atoms, however, is significantly higher. By averaging over an energy range extending to the energy of incidence, an upper estimate can be obtained as

$$\overline{E}_1 \approx U_s \left(2 \ln \frac{E}{U_s} - 3 \right) \tag{188}$$

which yields a mean energy of ~30 eV at an incident energy of 1 keV and a surface binding energy of 4 eV.

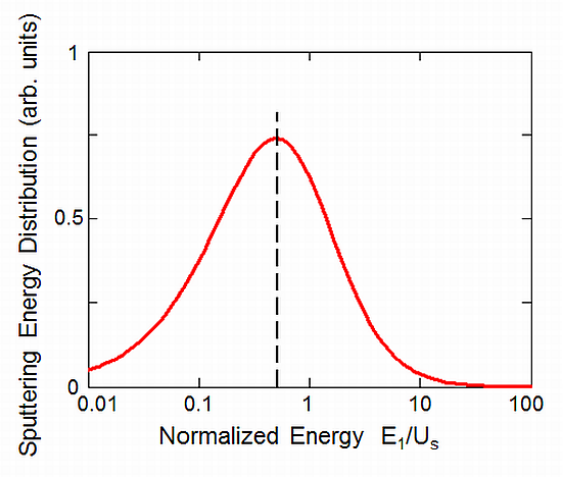

Fig. 47. Thompson energy distribution of sputtered atoms according to eq. (187). The dashed vertical line indicates the position of the maximum at $E_1 = U_s/2$

The sputtering yield, i.e. the number of sputtered atoms per incident ion, then results from integration of eq. (186) as

$$Y_s(E,\theta) = \frac{3}{2\pi^3 \lambda_0 a^2} \frac{S_n(E)}{\cos\theta} \int_0^\infty \frac{E_1 dE_1}{(E_1 + U_s)^3} \int_0^{\pi/2} \sin\theta_1 \cos\theta_1 d\theta_1 \tag{189}$$

The energy integration can be extended to infinity with only a minor error, as the integrand steeply decreases at increasing $E_1 >> U_s$.

We recall that the transport theory treatment is valid for an isotropic cascade evolution in an infinite medium with an internally starting ion. For large incident ion mass, the real cascade will mainly develop in forward direction, so that the theory overestimates the sputtering yield, whereas light ion bombardment increases the probability of momentum reversal. Still, the yield may be overestimated as the theory allows multiple transmissions of the recoil trajectories through the surface, similar to the range theory as described in sect. 7.1. Therefore, a correction factor α is applied, the theoretical calculation of which, however, is complicated and only successful for high ion-to-target mass ratios. Instead, a numerical fit obtained from comparison to experimental results is employed, which is shown in Fig. 48. Then, the final formula reads

$$Y_s(E,\theta) = \frac{3}{2\pi^3 \lambda_0 a^2} \frac{1}{U_s} \frac{S_n(E)}{\cos\theta} \alpha(m_1, m_2) \tag{190}$$

It should be noted that the $(\cos\theta)^{-1}$ dependence roughly holds at angles of incidence up to 60…70°. At larger angles, the isotropic cascade approximation becomes increasing doubtful, and ion reflection causes a decrease of the sputtering yield.

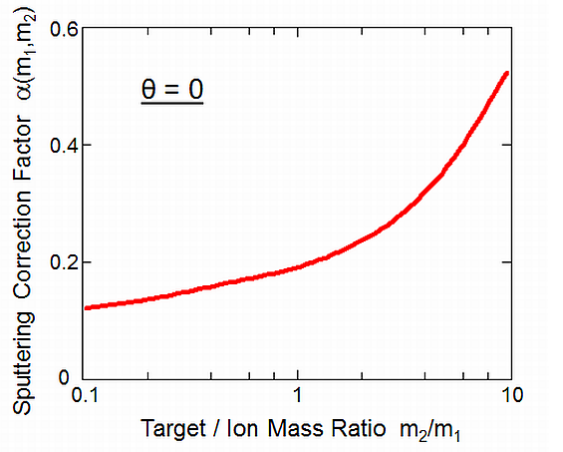

Fig. 48. Linear-cascade sputtering correction factor α (see eq. (190)), versus the target-to-ion mass ratio

An early comparison to experimental data is shown in Fig. 49 for different rare gases incident on copper[20]. Very good agreement is found between the experimental data and the prediction of eq. (190), except for the highest energy densities around the nuclear stopping power maximum for the heaviest projectile (see sect. 9.2).

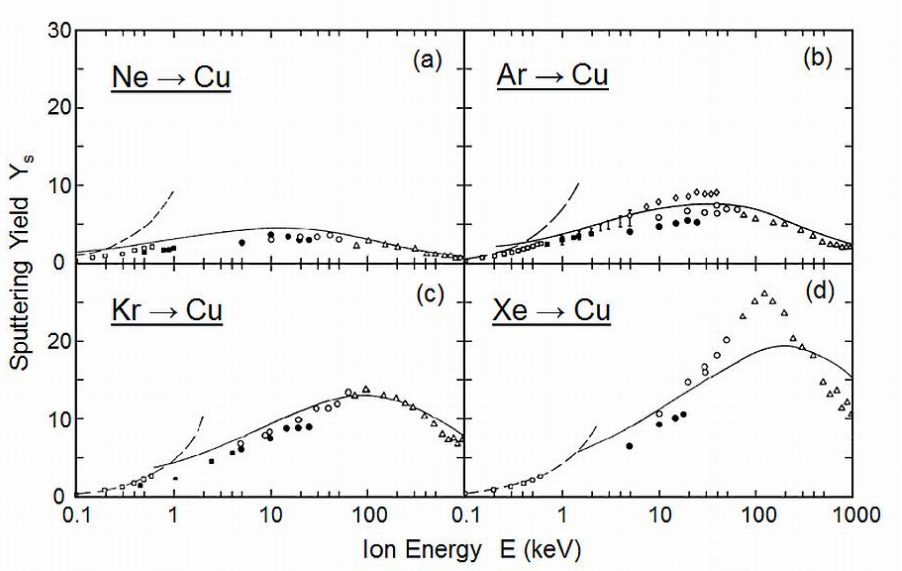

Fig. 49. (a-d) Sputtering yields vs. ion energy, for different rare gas ions onto Cu at normal incidence. The predictions of eq. (190) (solid lines) are compared to various experimental data sets. The dashed lines result from a low-energy approximation of nuclear stopping. (After ref.[20]; for the experimental data, see references therein)

As a further shortcoming of the above linear cascade theory of sputtering, the existence of a threshold incident energy has been disregarded. Sputtering requires a minimum energy transfer to a surface atom, and thus a minimum energy of the cascade atoms. This is particularly important for light incident ions associated with small energy transfers to the target atoms. For this, a simple mechanism is the backscattering of the ion at a subsurface bulk atom with only a small energy transfer due to the poor mass fit, and a subsequent collision with a surface atom which is then ejected. Assuming a backscattering angle close to 180° and a central collision with the surface atom, the latter receives an energy $E_0 = \gamma(1-\gamma)E$, so that the sputtering process requires a minimum incident ion energy

$$E_{th} = \frac{U_s}{\gamma(1-\gamma)} \tag{191}$$

However, the ion could also be backscattered by two subsequent collisions at about 90°, which would result in a larger final energy at the surface compared to one 180° collision if electronic energy loss is neglected, or by a series of small-angle scattering events with even higher final energy. The latter, however, becomes increasingly improbable, and might also be influenced by significant electronic energy loss. Thus, any well-defined threshold energy of sputtering cannot readily be given. Semiempirical formulas correcting the sputtering yield have been proposed to include threshold effects, partly based on fits to experimental results, such as the one by Bohdansky[149] (for normal incidence)

$$Y_s^{thr}(E) = Y_s(E) \cdot g\left(\frac{E}{E_{th}}\right) \tag{192}$$

with the correction function

$$g(\xi)=\left(1-\xi^{3/2}\right)(1-\xi)^2 \tag{193}$$

and a threshold energy which, in comparison to eq. (191), is formally extended to all ion-target combinations according to

$$E_{th}=\begin{cases}\dfrac{U_s}{\gamma(1-\gamma)} & if \quad \dfrac{m_1}{m_2}<0.2\\ 8U_s\left(\dfrac{m_1}{m_2}\right)^{2/5} & else\end{cases} \tag{194}$$

Fig. 50 demonstrates the effect of the sputtering threshold on the prediction of the sputtering yield. Below a few 100 eV, there is a pronounced difference from the result of eq. (190). The yield essentially vanishes at around 30 eV, which is almost one order of magnitude above the surface binding energy.

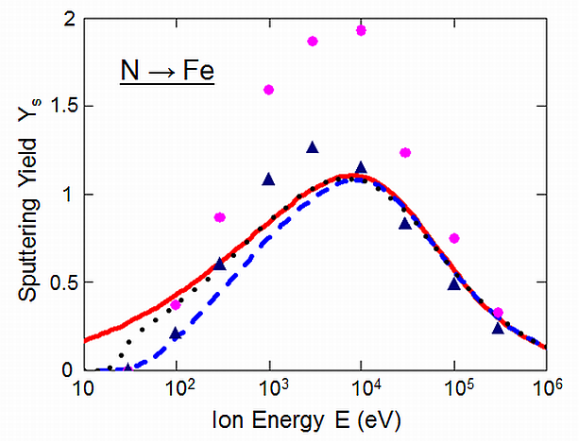

Fig. 50. Sputtering yield vs. ion energy for nitrogen incident on iron, from linear cascade theory (eq. (190), solid line), linear cascade theory including threshold energy correction according to eqs. (192)-(194) (dashed line), the fit data collection by Eckstein[150] based on BCA computer simulation (thin dotted line), and from specific BCA simulations using the 2011 versions of TRIM[69] (dots) and TRIDYN[103] (triangles)

9.1.2 Computer Simulation

It is straightforward to apply BCA computer simulation (see sect. 6.1) to linear-cascade sputtering by means of codes which trace the entire collision cascade. Mostly the planar surface binding model (eq. (185)) is employed to describe the transmission of recoil atoms through the surface, or their back-reflection into the bulk (see Fig. 46). Thus, the surface binding energy U_s enters the simulation as an additional energy parameter. However, for elemental materials, this does not introduce additional uncertainties when inserting the heats of sublimation. (The choice of the surface binding energy for alloys and compounds will be described in sect. 9.3.) A standard sputtering version for amorphous materials is TRIM.SP[92,85] which is based on early TRIM[85].

Broad data sets of energy-dependent sputtering yields have been created using BCA simulation for amorphous materials[151,152]. Recently, Eckstein[150] has compiled energy-dependent sputter yields at normal incidence, making use of a universal analytical fit formula applied to the computer generated data. The results, which span several decades as function of the ion energy for each ion-target combination, are mostly in reasonable agreement with experimental data where available, although there is some tendency that the experimental obeservation are underestimated. However, the experimental data may suffer from systematic errors, as, e.g., surface roughening during bombardment. On the other hand, there are uncertainties in the BCA simulations which are related to the choice of the parameters (see section 6.1.2), by which the obtained sputtering yields may vary by up to about 30%.

Also Fig. 50 confirms that sputter yield predictions by BCA computer simulation have to be taken with some care. For the chosen example of nitrogen incident on iron, the fit curve by Eckstein[150] largely coincides with the analytical prediction, except at low energy where threshold effects become important. In comparison, TRIM[69] with standard parameters overestimates the yield near the maximum by a factor of almost two, which is also found for other ion-target combinations. Thus, standard TRIM is not recommended for the generation of sputtering data. The data calculated by TRIDYN[103] in static mode agree with the analytical predictions within the expected accuracy, but show a shift of the maximum yield to lower energy.

At the first glance, the success the binary collision approximation, which is the basis of both analytical theory and BCA computer simulation, appears to be surprising, as the collision cascades are treated down to energies of a few eV, which is the magnitude of the surface binding energy. This is clearly below the expected range of validity of the binary collision approximation (see section 6.1.3). However, the mean energy of the sputtered atoms is in the order of some 10 eV as stated above. The mean energy of the contributing cascade atoms is even somewhat higher, thus apparently still being consistent with the lower validity limit of the binary collision approximation.

In this view, molecular dynamics simulations with their high computational efforts are not expected to be an efficient tool for the calculation of linear cascade sputtering yields, as far the sputtering of single atoms is concerned. Nevertheless, there are specific aspects where MD simulations (see refs. [154,155] and references therein) are helpful and partly indispensable. For example, the characteristic depth of origin of sputtered atoms has been established using MD simulation (see, e.g., refs.[156,157]). The vast amount of sputtered atoms (~90%) results from the two top atomic layers.

The angular distributions of atoms sputtered from single crystals are known to show characteristic patterns[158], which depend on the details of the recoil collisions near the surface. Thus, a detailed interaction potential as used in MD simulations is helpful to simulate this phenomenon. An example is given in Fig. 51[153]. In addition, it is demonstrated that the MD simulation enables the description of cluster emission, which is out of the scope of binary collision simulations. A significant difference of the ejection patterns for sputtered monomers and dimers is found.

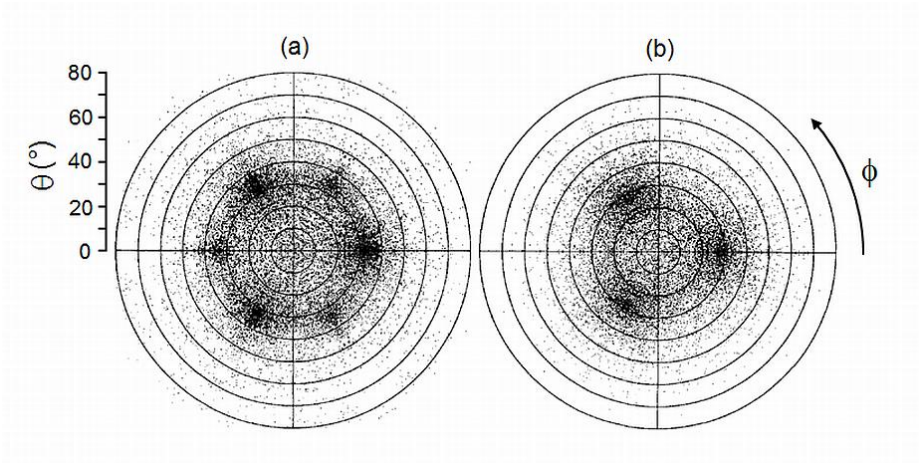

Fig. 51. Angular ejection patterns of atoms (a) and dimer clusters (b) sputtered from a Cu(111) surface under with 1 keV Ar bombardment, as obtained from molecular dynamics computer simulation. Monomers are preferentially emitted in <110> direction and, with weaker intensity, in <100> direction, whereas dimers are preferentially emitted only in <110> direction. θ and ϕ denote the polar and azimuthal angles of ejection, respectively. (After ref.[153])

9.2 Thermal Spike Sputtering

As shown above, reliable theoretical tools are available for the sputtering from the linear cascade. In contrast, there is comparably little information on thermal spike sputtering both theoretically and experimentally. In the thermal spike picture, sputtering is described by evaporation of atoms from the surface. According to Maxwell-Boltzmann statistics, the flux of evaporated atoms at a given temperature T is given by

$$j_{ev}(T) = n\sqrt{\frac{kT}{2\pi m_2}}\exp\left(-\frac{U_s}{kT}\right) \tag{195}$$

The thermal sputtering yield from a cylindrical thermal spike is then given by the integration over the surface area and over time according to

$$Y_s^{th} = \int_0^\infty dt \int_0^\infty 2\pi r dr\; j_{ev}(T(r,t)) \tag{196}$$

Linear cascade sputtering and thermal spike sputtering can be regarded as being essentially independent, as linear cascade sputtering mainly results from fast recoils in the early phase of cascade development, whereas the elastic thermal spike develops at a later stage. Thus, the yields can be linearly superimposed to obtain the total yield

$$Y_s^{tot} = Y_s + Y_s^{th} \tag{197}$$

For the simplest treatment of an elastic thermal spike with instantaneous initial energy dissipation along an ideal line (see sect. 8.2), the temperature of eq. (174) can be inserted into eq. (196). Then, the resulting sputtering would scale with the square of the nuclear stopping force, $Y_s^{th} \propto (dE/dx)_n^2$. More adequately, eq. (176) is employed. As shown by Sigmund and Claussen[141], the resulting yield scales approximately quadratically with the nuclear stopping force as well, and is thereby proportional to the square of the linear cascade yield. Their rough quantitatitive result is

$$Y_s^{th} \approx 0.06 \cdot Y_s^2 \tag{198}$$

However, this is very sensitive to the initial core temperature in the spike. If the initially deposited energy is more realistically distributed across a cylinder of finite radius (which, however, is difficult to define), the thermal sputtering yield drops significantly. Thus, eq. (198) must be considered as an upper estimate. Nevertheless, it indicates that a significant contribution of elastic thermal spike sputtering can only be expected if $Y_S \gtrsim 10$. This is in semiquantitative agreement with the observed enhancement of the heavy-ion sputtering yield at energies where the linear cascade yield is maximum (see Fig. 49(d)), so that this phenomenon is taken as an evidence for elastic thermal spike sputtering.

Further evidence for elastic thermal spike sputtering has been concluded from irradiations with heavy oligomer cluster ions[159-161]. At identical energy per incident atom, the sputtering yield per atom is significantly higher than for the respective monomer ions. E.g., a nonlinear enhancement by a factor of more than 10 has been reported[161] for Au_5 cluster ions versus Au monomer ions incident on Au.

Any effect of inelastic thermal spikes (see subsection 8.2.2) on sputtering is expected to become most evident for heavy ions at energies around the maximum of electronic stopping, where the nuclear stopping and thereby the collisional sputtering yield become extremely small. As recently reviewed by Assmann[162], the experimental data base is rather scarce. Nevertheless, sputtering yields are established which clearly exceed the linear cascade yields. The effect depends strongly on the type of materials (metals versus, e.g., oxides), which, in the picture of a

thermal spike, can partly be attributed to the widely different thermophysical properties. Generally, the yields depend on the charge state of the incident ions which is indicative of an electronic mechanism, as the relaxation to the equilibrium charge state (see subsection 4.3.1) results in an additional electronic energy deposition close to the surface.

An example for a metal is given in Fig. 52 for gold ions at energies slightly below the maximum of the electronic stopping force[162,163]. Although electronic stopping largely overweighs nuclear stopping (by a factor of about 300 in the present range of energies), the experimentally data rather follow the energy dependence of nuclear stopping, although being larger in magnitude by a factor of about 5. For comparison, the authors performed pure inelastic thermal spike calculations according to eqs. (177) and (178), with the resulting time-dependent temperature fields inserted into eq. (196). In addition, also the nuclear energy deposition was included by an additional source term in eq. (178), so that a combination of an inelastic and elastic thermal spike is being modeled. Whereas the thermal spike results alone do not give any satisfactory fit to the data, the superposition of linear cascade sputtering and inelastic plus elastic thermal spike sputtering only slightly underestimates the data and yields a similar energy dependence.

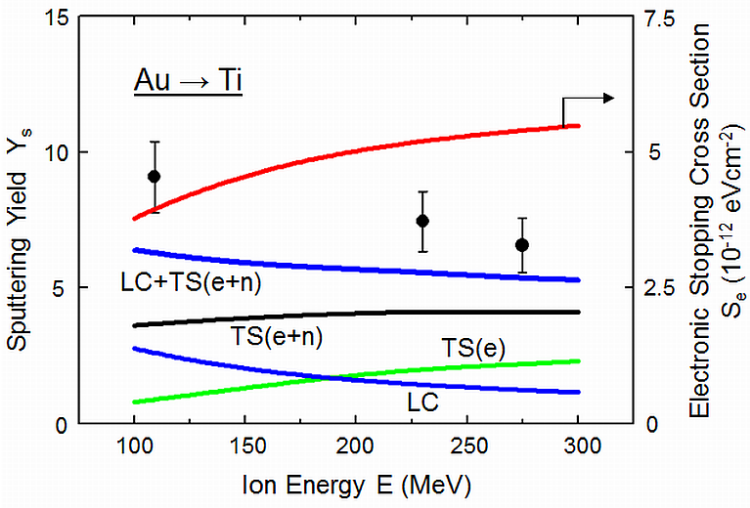

Fig. 52. Swift heavy ion sputtering for gold incident on titanium at an angle of 72° with respect to the surface normal and with the equilibrium charge state. The experimental data[162,163] are compared to the linear cascade prediction (LC - eq. (190)) and thermal spike calculation results[142,143] (eqs. (177), (178)) for purely electronic energy deposition (TS(e)) and including nuclear energy deposition (TS(e+n)), as well as to the sum of the LC and TS(e+n) predictions. The electronic stopping cross section as obtained from SRIM2011[69] is shown for comparison. (The TS(e) and TS(e+n) lines have been interpolated from the original data[162] which had only been evaluated at the experimental ion energies.)

Large sputtering yields of up to about 1000 are obtained from oxides in the regime of high electronic sputtering[164,165]. This is qualitatively consistent with the thermal spike model in view to the low thermal conductivity as compared to metals. Fig. 53 shows an example for SiO_2[162]. Good fits are obtained here with the inelastic thermal spike model, with the electron mean free diffusional pathlength as a free parameter. The latter is significantly lower in the amorphous material, which results in an increased confinement of the thermal spike.

Sputtering yields in the nuclear stopping regime which significantly exceed the predictions from linear cascade theory have been reported, e.g., for frozen gases[166]. In the electronic stopping regime, excessively high sputtering yields with values close to 10^4 have been found for ionic crystals such as LiF, which can not be explained by an inelastic thermal spike[163,164]. These phenomena have been partly attributed to a contribution of bulk excitons and/or defect migration to sputtering, but a clear general picture has not been consolidated.

For the computer simulation of sputtering in the thermal spike regime, MD simulations are the appropriate tool (see, e.g., ref.[155] and references therein). However, quantitative predic-

tions remain difficult. Due to large computational effort, most of the simulations have been performed with simple interaction potentials (such as the Lennard-Jones potential, eq. (134)), so that the results might partly not be realistic. For the same reason, only a few single events of spike development after ion incidence can typically be simulated, so that it becomes difficult to acquire statistics.

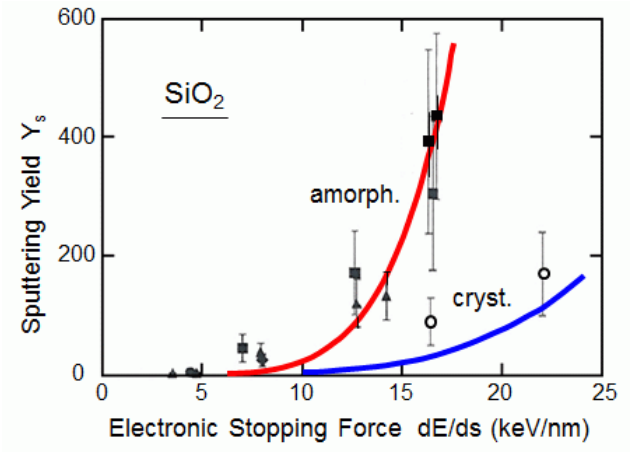

Fig. 53. Electronic sputtering of vitreous silica (full symbols) and crystalline quartz (open circles) by different swift heavy ions. The sputtering yield is shown as function of the electronic stopping force. The lines show the result of inelastic thermal spike calculations with the mean electron diffusion pathlength as free parameter. (After ref.[162])

However, also the modeling of single hit events may provide interesting new insights. This is demonstrated in Fig. 54[167] for the formation of a sputter crater under heavy-ion bombardment, as obtained from molecular dynamics simulation with an EAM potential (see subsection 6.2.2). The crater is accompanied by a rim with several piled-up atomic layers. Simultaneously, the formation of adatoms on the surface is modeled. At the energy of 100 keV, the simulated sputter yield is enhanced by a factor of 10 compared to the linear cascade prediction (by an earlier version of TRIM[69]), which confirms the role of an elastic thermal spike. Sputter craters have been found at energies down to 5 keV, where, within statistics, the sputter yield is similar to the prediction by BCA computer simulation. Quantitatively, the average observed yield of ~15 at 5 keV would also be consistent with a contribution of thermal spike sputtering according to eqs. (197) and (198). This quantitative comparison of analytical and simulated thermal spike yields, however, remains vague in view of the systematic and statistical uncertainties.

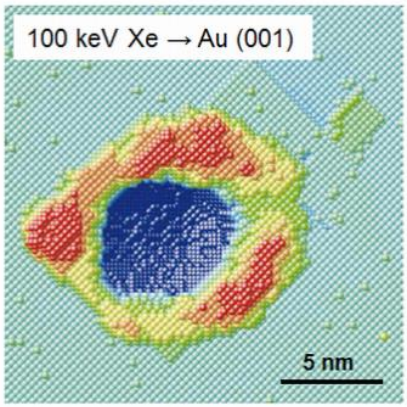

Fig. 54. Sputter crater formed by 100 keV Xe incident on Au(001) at a polar angle of incidence of 25° with respect to the surface normal, and an azimuthal angle of 25° with respect to the [100] direction, as obtained for molecular dynamics simulation. The angles have been chosen to avoid channeling. (After ref.[167])

Moreover, the observation of the sputter crater renders the analytical models of thermal spike sputtering questionable, as the sputtering might result from some collective ejection of the material rather than from evaporation at the surface only, which is implied in eq. (196).

Molecular dynamics simulations of inelastic thermal spikes (see, e.g. ref.[168]) suffer from the uncertainty of the electron mean free diffusional pathlength, as do the predictions from the analytical thermal spike model (see above).

9.3 Preferential Sputtering of Compounds

The sputtering yield from a multicomponent system is composed from the partial yields of the individual components $Y_{s,i}$ according to

$$Y_s = \sum_i Y_{s,i} \tag{199}$$

However, the partial yields are in general not proportional to the respective surface atomic fractions, which is known as preferential sputtering[169-171]. Preferential sputtering may arise from different surface binding energies of the components. In the picture of the linear cascade, it may also depend on the collisional development of the cascade, in particular if the components exhibit widely different atomic masses. The energy transfer in primary collisions between the incident ions and the target atoms is most efficient for target masses being close to the ion mass. Also during the subsequent evolution of the cascade, the energy transfer is most efficient between partners of the same species, so that cascades of the different species can, very roughly, be considered to develop independently. Consequently, even at similar surface binding energies, a preferential sputtering of the species with best mass fit to the ion is expected. This, however, may additionally be influenced by the energy loss and the scattering of the cascade atoms.

This complicated interaction of different collisional processes is combined with the dynamic alteration of the surface composition at increasing ion fluence, which naturally results from preferential sputtering. Thereby, any analytical description of preferential sputtering phenomena is subjected to strong limitations.

The partial sputtering yields can be written as

$$Y_{s,i} = q_{s,i} Y_{c,i} \tag{200}$$

where $q_{s,i}$ and $Y_{c,i}$ denote the atomic fractions at the surface and the so-called "component" yields, respectively. Applying eq. (200) to only one component i ($q_{s,i} = 1$) shows that the component yields are identical to the sputtering yields of the pure components. The definition of preferential sputtering implies that the component yield of at least one component is different from the others. As this is the regular situation, preferential sputtering must be considered as a standard phenomenon during the irradiation of multicomponent materials.

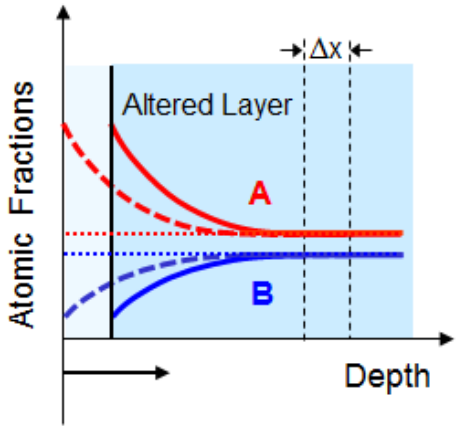

Fig. 55. Stationary state due to preferential sputtering in an initially homogeneous binary compound. Component B is assumed to be preferentially sputtered, by which the surface is enriched in A. Prolonged irradiation moves the altered layer further into the bulk with a stationary depth profile in the limit of large fluence. The thin dotted lines indicate the initially homogeneous composition before irradiation

As stated above, preferential sputtering alters the surface composition at increasing ion fluence. For simplicity, an initially homogeneous two-component material is assumed which contains the components *A* and *B*, with *B* being sputtered preferentially. The surface concentration of *A*, and thereby the partial sputtering yield of *A*, will then increase, which counteracts the initially enhanced sputtering of *B*, so that the system develops towards a stationary state (see Fig. 55). In the stationary state (upper index ∞), mass conservation requires that the relative amounts of sputtered species reflect the bulk composition of the material with the atomic fractions q_i, i.e.

$$\frac{Y_{s,A}^{\infty}}{Y_{s,B}^{\infty}} = \frac{q_A}{q_B} \tag{201}$$

With eq. (200) written for both the initial (upper index 0) and the stationary state, this yields

$$\frac{q_{s,A}^{\infty}}{q_{s,B}^{\infty}} = \frac{q_A}{q_B}\frac{Y_{c,B}}{Y_{c,A}} = \left(\frac{q_A}{q_B}\right)^2 \frac{Y_B^0}{Y_A^0} \tag{202}$$

so that the component sputter yields or the initial partial sputtering yields determine the final surface composition.

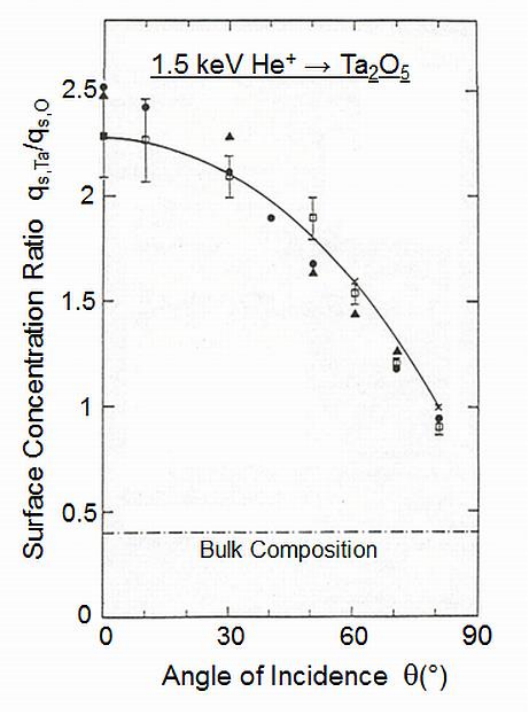

Fig. 56. Stationary surface composition in the limit of large ion fluence for low-energy He irradiation of Ta_2O_5. Solid symbols are from experimental data, open squares from TRIDYN[93] simulation. The line is drawn to guide the eye. (After ref.[173])

An example is given in Fig. 56 for the preferential sputtering of Ta_2O_5 by helium ions[172,173]. The primary energy transfer to oxygen atoms is larger than to tantalum atoms. In addition, for the low-energy light-ion bombardment, the threshold effect becomes important in particular for tantalum, which additionally favors the sputtering of oxygen. (Eq. (191) yields a helium threshold energy of about 100 eV for the sputtering of pure tantalum.) Thus, tantalum is strongly enriched at the surface. For a wide range of angles of incidence, the experimental values are in good agreement with eq. (202) (not shown). However, the pronounced dependence of the stationary surface composition on the angle of incidence, as seen in Fig. 56, is surprising, since a similar $\cos^{-1}\theta$ dependence (see eq. (190)) of the partial sputtering yields would be naively expected for both components.

Dynamic BCA computer simulation (see subsection 6.1.4) can be considered as an ideal tool for the treatment of preferential sputtering, if collisional phenomena dominate and the influence of any physicochemical effects such as thermal diffusion or surface segregation is negligible. However, the definition of the surface binding energies of the individual components requires special consideration [31,92,93]. A dependence of the surface binding energies of the individual components, $U_{s,i}$, on the surface composition (and thereby on the ion fluence) cannot be excluded. The influence of the surroundings of each sputtered atom can be approximated in a regular solution ansatz according to

$$U_{s,i} = \sum_j U_{ij} q_{s,j} \tag{203}$$

Simple recipes for the definition of the matrix elements U_{ij} can be based on thermophysical data as described in ref.[102]. For components which form a solid in the pure state, the diagonal elements are obviously equal to the surface binding energies of the pure substances, i.e. $U_{ii} = \Delta H_i$, where ΔH_i denotes the sublimation enthalpy (see subsection 9.1.1). For simplicity restricting to a two-component solid-solid compound $A_n B_m$, conservation of energy requires for the stoichiometric compound

$$nU_{s,A} + mU_{s,B} = n\Delta H_A + m\Delta H_B + \Delta H_f \tag{204}$$

where ΔH_f denotes the enthalpy of fusion of the compound. The non-diagonal matrix elements describe the interaction between atom *A* and *B*, and are therefore assumed to be symmetric. Then, applying eq. (203) to the stoichiometric compound with $q_{s,A} = n/(n+m)$ and $q_{s,B} = m/(n+m)$, the combination yields

$$U_{AB} = U_{BA} = \frac{1}{2}\left(\Delta H_A + \Delta H_B\right) + \frac{n+m}{2nm}\Delta H_f \tag{205}$$

For a solid-gas compound consisting of a solid constituent *A* and a diatomic gas constituent *B*, the analogue to eq. (204) reads

$$nU_{s,A} + mU_{s,B} = n\Delta H_A + \Delta H_f + \frac{m}{2}\Delta H_m \tag{206}$$

with ΔH_m denoting the molecular binding energy of the gas. As the gaseous atoms will normally be surrounded by the solid component and only weakly interact which each other, one may assume $U_{BB} \approx 0$. This results in

$$U_{AB} = U_{BA} = \frac{1}{2}\Delta H_A + \frac{n+m}{2nm}\Delta H_f + \frac{n+m}{4n}\Delta H_m \tag{207}$$

For specific compounds, however, more specific data for the surface binding energies are available (see, e.g., ref.[174]).

The result of TRIDYN[93,103] dynamic BCA computer simulations is also included Fig. 56, with excellent agreement with the experimental results. This suggests that the atomic transport, which establishes the composition profile in the altered subsurface layer, is of purely collisional nature. A closer inspection of the collisional mechanisms by means of the computer simulation reveals that the observed angular dependence of the stationary surface composition is due to details of the collision sequences which cause sputtering. The heavy tantalum atoms are little influenced by the presence of oxygen. In contrast, oxygen atoms may be significantly scattered by

tantalum, which results in a weaker dependence of the partial oxygen yield on the angle of incidence. This demonstrates the ability of computer simulations to understand detailed and complicated mechanisms which would not become clear otherwise.

9.4 Sputter-controlled Implantation Profiles

Implantation profiles at high fluence may be significantly influenced by sputtering. As schematically indicated in Fig. 57, the deposition profile of previously implanted atoms is shifted towards the surface at increasing ion fluence. Simultaneously, additional ions are implanted at the deep edge of the profile, which causes a profile broadening. Finally, when a surface layer has been sputtered off which is thick compared to the projected range, a stationary profile is established with a high concentration at the surface. Then, the ingoing ion flux becomes balanced by the partial sputtered flux of the implanted species.

For simplicity, let us assume a Gaussian range distribution according to

$$f_R(x) = \frac{1}{\sqrt{2\pi}\sigma_p} \exp\left(-\frac{\left(x - \bar{R}_p\right)^2}{2\sigma_p^2} \right) \tag{208}$$

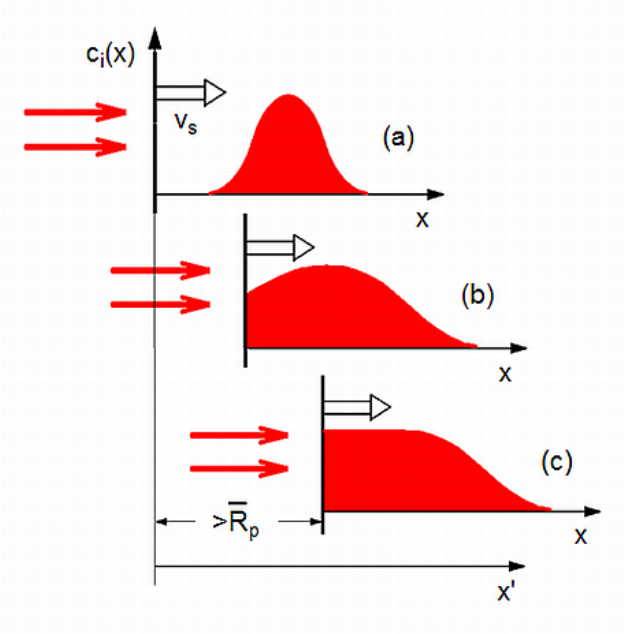

Fig. 57. Schematic representation of the formation of sputter-controlled implantation profiles with an implant concentration $c_i(x)$ versus depth x. With the surface moving with a velocity v_s due to sputtering, the initial low-fluence profiles which reflect the range distribution (a) are gradually broadened (b) and approach a stationary state (c) when the sputtered depth becomes larger than the mean projected range $\bar{R}_p$. x' denotes the depth axis with respect to the original position of the surface

where x represents the depth in the system of the moving surface. At a given time t, the depth-dependent atomic density of the implant, $n_i(x,t)$, result from the superposition of the previous range distributions. If the surface is continuously eroded by sputtering with a velocity υ_s, only certain large-depth fractions from the previous implantation still contribute. This is expressed by the accumulation integral

$$n_i(x,t) = j_i \int_0^t f_R\left(x + \upsilon_s(t - t')\right) dt' \tag{209}$$

where j_i denotes the ion flux. By variable transformation this results in

$$n_i(x,t) = \frac{j_i}{\upsilon_s} \int_x^{x+\upsilon_s t} f_R(\xi)\, d\xi \tag{210}$$

into which eq. (208) is inserted for integration. If any swelling due to the implanted atoms, as well as their contribution to sputtering, is neglected, the removal rate in terms of host areal density is

$$n\upsilon_s = j_i Y_s \tag{211}$$

by definition of the sputtering yield, where *n* denotes the atomic density of the host. Then, the integration results in

$$n_i(x,t) = \frac{n}{Y_s}\left[erf\left(\frac{x+\upsilon_s t - \overline{R}_p}{\sigma_p} \right) - erf\left(\frac{x-\overline{R}_p}{\sigma_p} \right) \right] \tag{212}$$

where $erf(\xi)$ denotes the Gaussian error function. Towards infinite time, the stationary implantation profile becomes

$$n_i(x, t\to\infty) = \frac{n}{Y_s}\left[\frac{1}{2} - erf\left(\frac{x-\overline{R}_p}{\sigma_p} \right) \right] \tag{213}$$

which, for a sufficiently narrow range distribution with $\sigma_p \ll \overline{R}_p$, results in the stationary surface concentration

$$n_i(x=0, t\to\infty) = \frac{n}{Y_s} \tag{214}$$

so that the relative surface concentration is roughly given by the inverse of the sputtering yield.

In the above simplified treatment, it has been implicitly assumed that the sputtering yield is independent of time. In reality, it might be significantly influenced by the presence of the implanted species. Thus, eqs. (213) and (214) are strictly valid only for small concentrations of the implant. This requires a sputtering yield which is significantly larger than one.

Without the above simplifications, sputter-controlled implantation profiles can be predicted from dynamic BCA simulations. Fig. 58 shows the retained amount and a sequence of implantation profiles for sulfur ions implanted into molybdenum. The implantation becomes increasingly inefficient at fluences above ~$2\cdot10^{16}$ cm^{-2}, as indicated by the retention curve. The depth profile at the lowest fluence, which reflects the range profile, becomes significantly distorted at the higher fluences. Stationarity is obtained at a fluence around $1.5\cdot10^{17}$ cm^{-2}, after erosion of about 20 nm, which is approximately 2.5 times the mean projected range. Compared to the simple error-functional shape predicted by eq. (213), there is a concentration drop at the surface due to preferential sputtering (see the previous subsection). Nevertheless, the stationary profiles exhibit a nearly flat top with an atomic fraction of about 0.4, corresponding to a relative S/Mo concentration of 0.67. The sputtering yield for 10 keV sulfur ions incident on molybdenum is 2 according to the Sigmund formula, eq. (190). Thereby, the stationary concentration from the simple analytical result of eq. (214) is about 30% smaller. Another example of a BCA simulation of sputter-controlled implantation is shown in Fig. 37(b). Here, the nitrogen concentration has been artificially limited to the stoichiometric value of Si_3N_4 so that the profiles become similar to the local saturation profiles (Fig. 37(a,c)). Additional features are found close to the surface which are attributed to preferential sputtering.

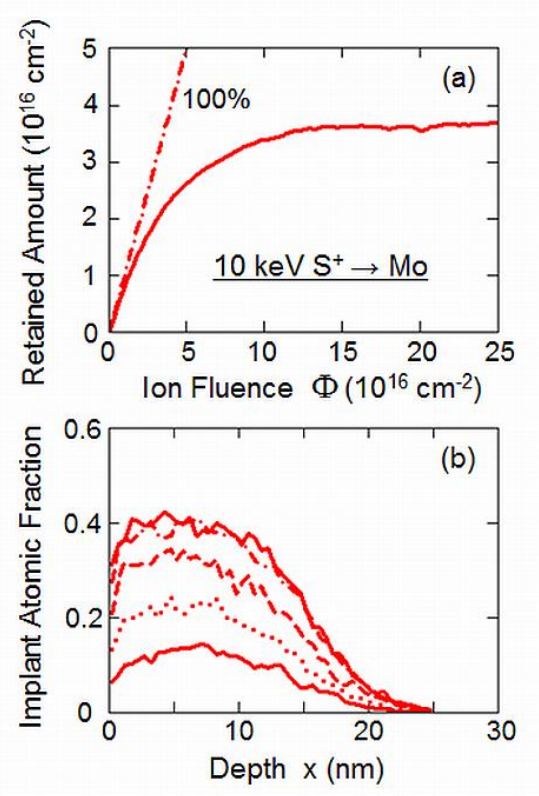

Fig. 58. Sputter-controlled implantation profile for 10 keV sulfur in molybdenum from TRIDYN[93] computer simulation. (a) Retained amount vs. ion fluence, with the hypothetical 100% retention in the absence of ion reflection and sputtering being indicated. (b) Corresponding implantation profiles at fluences of $1.5 \cdot 10^{16}$ cm^{-2} (solid line), $3 \cdot 10^{16}$ cm^{-2} (dotted line), $6 \cdot 10^{16}$ cm^{-2} (dashed line), $1.2 \cdot 10^{17}$ cm^{-2} (dashed-dotted line) and $2.4 \cdot 10^{17}$ cm^{-2} (solid line). At the final fluence, a surface layer of 27.5 nm has been sputtered off

10 Damage

The following section will address atomic relocations ("displacements") in the subsurface bulk of the irradiated material which remain after the thermalization of the cascade or spike[17-19,175]. In an ideal lattice, an individual atomic displacement forms a so-called Frenkel pair consisting of a generated interstitial atom and a vacancy which is left behind at the original location of the atom. This may be considered as the elementary process of irradiation damage. In contrast to sputtering, where the relocation into the vacuum is inherently permanent, bulk relocations are not necessarily stable, as the generated defects might thermally diffuse, resulting in, e.g., recombination, clustering or annihilation at the surface. Such post-cascade or post-spike effects will not be in the scope of the present contribution. Further, the topic will be restricted to damage which results from atomic motion, rather than being directly generated by electronic excitation, such as it is common in insulators[176,177].

10.1 Linear Cascade Damage

10.1.1 Analytical Treatment

The formation of defects in a linear cascade has been first addressed for hard-sphere collisions by Kinchin and Pease[178]. In order to produce a "stable" Frenkel pair in the above sense, the distance between the generated interstitial atom and the vacancy has to be sufficiently large so that an immediate recombination due to elastic forces in the lattice and/or due to directed atomic bonds is prevented. Therefore, the initial energy transfer to the recoil, E_0, has to exceed a "dis-

placement threshold" energy U_d . This minimum energy transfer depends on the crystalline direction into which the recoil is set into motion[179]. Therefore, it is understood as an average over different knock-on directions. The displacement threshold energy must be larger than the Frenkel pair formation enthalpy since kinetic energy is dissipated during the slowing down of the recoil. In metals and semiconductors, Frenkel pair formation enthalpies are in the range 5…10 eV, whereas the displacement threshold energies range from about 15 to 80 eV. It should be emphasized that these values relate to isolated defects in a perfect crystal. The displacement threshold may become significantly lowered in case of a material with a significant amount of defects, such as arising from high-fluence energetic ion bombardment (see sect. 11).

For a primary recoil generated in a nuclear collision between the fast ion and a target atom, the total number of generated Frenkel pairs in the associated subcascade is then given by

$$N_F(T) = \int_{U_d}^{T} F(T, E_0) P_d(E_0) dE_0 \tag{215}$$

where T denotes the energy transfer in the primary collision, $F(T,E_0)$ the recoil density (see eq. (170)), and $P_d(E_0)$ the probability that a recoil of start energy E_0 is being displaced. For the probability function, the simplest model would be a sharp threshold with P_d vanishing below U_d and being equal to 1 above. However, this would ignore the mechanism of replacement collision sequences. In particular a low-energy recoil may replace a target atom, which in turn may replace another one. In crystals, such sequences may propagate along low-index directions, being focused by the neighboring strings of atoms. Thus, several recoils are involved which are all counted in the recoil density, whereas only one Frenkel pair results with the interstitial at the end of the sequence. Thus, $P_d = 1$ is an overestimate at low energies, which dominate the recoil density (see sect. 8.1). To account for this (although somewhat arbitrary), P_d is assumed to linearly increase from 0 to 1 between U_d and $2U_d$, i.e.

$$P_d(E_0) = \begin{cases} 0 & ; \quad E_0 < U_d \\ \dfrac{E_0 - U_d}{U_d} & ; \quad U_d < E_0 < 2U_d \\ 1 & ; \quad E_0 > 2U_d \end{cases} \tag{216}$$

For sufficiently large T, eq. (215) then results in

$$N_F(T) = \frac{6\ln 2}{\pi^2} \frac{\nu_D(T)}{U_d} = 0.42 \frac{\nu_D(T)}{U_d} \tag{217}$$

With eq. (169), this is only little different from the original Kinchin-Pease formula which had been derived for hard-sphere collisions

$$N_F(T) = \frac{T}{2U_d} \tag{218}$$

Formally, eqs. (217) and (218) allow for subthreshold damage, too (c.f. the corresponding remarks for sputtering in subsection 9.1.1). Therefore, the so-called “modified” Kinchin-Pease formula is often employed according to[180]

$$N_F(T)=\begin{cases}0 & ;\quad T<U_d\\ 1 & ;\quad U_d<T<2.5\,U_d\\ 0.4\dfrac{\nu_D(T)}{U_d} & else\end{cases} \tag{219}$$

Looking now at the generation of damage along the trajectory of an incident ion, a damage cross section σ_D can be introduced, so that the number of generated Frenkel pairs per unit path-length of the ion can be written as

$$\frac{dY_{FP}}{ds}=n\sigma_D \tag{220}$$

Attributing the local generation of damage to the primary energy transfers in nuclear collisions, the damage cross section results from the probability of nuclear collisions, $n\int d\sigma_n(T)$, as

$$\sigma_D(E')=\int_{U_d}^{\gamma E'} N_F(T)\frac{d\sigma_n(E',T)}{dT}\,dT \tag{221}$$

where γ denotes the energy transfer factor according to eq. (7) and E' the instantaneous energy of the ion. The total yield of Frenkel pairs for an ion of energy E results then from the integration of eq. (220) along the ion trajectory, according to

$$Y_{FP}(E)=\int_{U_d/\gamma}^{E}\frac{\sigma_D(E')}{S(E')}dE' \tag{222}$$

where the trajectory integral has been transformed into an energy integral by means of the total stopping cross section $S(E')=S_e(E')+S_n(E')$ (see eq. (52)).

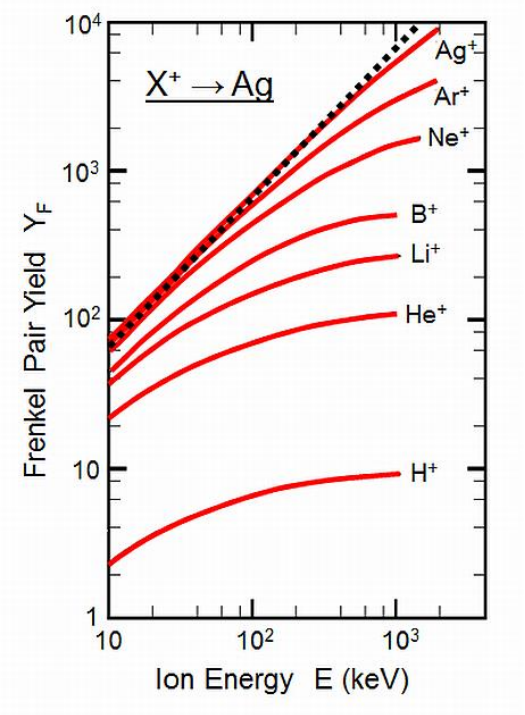

Fig. 59. Frenkel pair production from the linear cascade for different ions incident on silver (solid lines; after ref.[180])., from a rigorous evaluation of eq. (222) (see text) a displacement threshold energy of 39 eV for Ag. The dotted line reproduces the simple Kinchin-Pease formula (eq. (223)).

Fig. 59 displays the energy dependence of the Frenkel pair yield for different ions incident on silver, as obtained from a detailed evaluation[180] of eq. (222), using eq. (119) with a specific calculation of the damage energy $\nu_D(T)$. At higher energies, the influence of electronic energy loss becomes increasingly important, so that the curves bend over from a linear increase with energy. Electronic stopping also increasingly dominates for lighter ions, so that the Frenkel pair generation spans over up to three orders of magnitude for different ions at identical energy.

For a simplified evaluation of eq. (222), the original Kinchin-Pease formula (eq. (218)) is inserted, and an average energy transfer is assumed which is large compared to the displacement threshold energy. Then, according to eq. (51), the inner integral can in good approximation be replaced by the nuclear stopping cross section. For such a "dense" cascade, which occurs for large nuclear energy deposition, the electronic stopping is small so that $S(E') \approx S_n(E')$. Further, for sufficiently large energy, $E \gg \gamma U_d$, the lower limit of the outer integral can be set to zero. The result then becomes

$$Y_{FP}(E) = \frac{E}{2U_d} \tag{223}$$

which means that the Kinchin-Pease formula can be directly evaluated for the incident ion energy in case of dominant nuclear stopping. This rough prediction is also included in Fig. 59, and found to be well acceptable for ions with $Z_1 > 20$ at energies up to 100 keV.

Alternatively, for light ions with small primary energy transfers, it can be assumed that the defect production is mainly due to primary recoils, which corresponds to $N_F(T) = 1$. At keV ion energies, the scattering cross section can be evaluated for a power-law potential with the exponent s = 2 (see Fig. 6), resulting in $d\sigma(E,T)/dT \propto E^{-1/2}T^{-3/2}$ according to eq. (47). The contribution of nuclear stopping to the total stopping is assumed to be negligible. Further inserting velocity-proportional electronic stopping according to eq. (66), the evaluation of eq. (222) yields[181]

$$Y_{FP}(E) = \frac{2C_2}{k_e\sqrt{U_d}}\left[\ln\left(\frac{\gamma E}{U_d}\right) - 2\left(1 - \sqrt{\frac{U_d}{\gamma E}}\right)\right] \tag{224}$$

As shown in Fig. 60, this prediction is in good agreement with experimental data obtained after low-temperature bombardment of different metals with hydrogen ions.

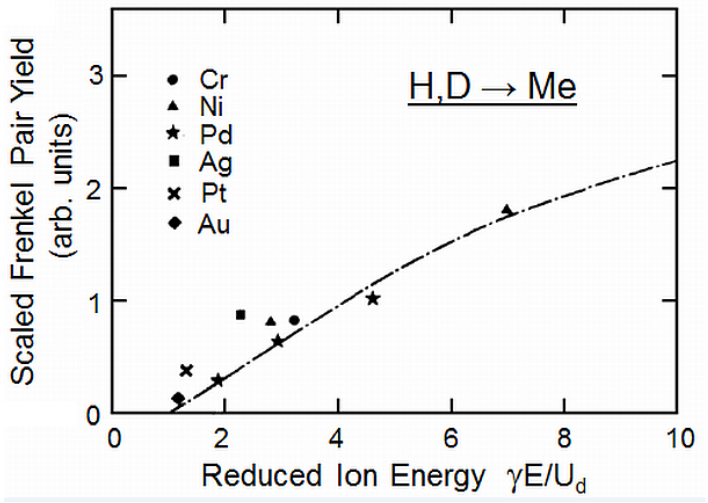

Fig. 60. Frenkel pair production under proton and deuteron irradiation of different metals at incident energies up to 10 keV. The experimental data (points) are compared to the prediction of eq. (224) (line). Note that all data have been normalized to remove the dependence of the prefactor of eq. (224) on the ion and target atomic numbers and masses. The maximum absolute yield is 1.25 for protons on Ni at an energy of 10 keV. (After ref.[181])

In the frame of analytical theory, the depth distribution $f_{FP}(x,E)$ of generated defects is most conveniently identified with the 1-dimensional damage function (see sect. 8.1 and eq. (182)), so that

$$f_{FP}(x,E) = C_D\, f_D(x,E) \tag{225}$$

with a normalization constant C_D that fulfills $\int f_{FP}(x,E)dx = Y_{FP}(E)$. Alternatively, the Frenkel pair distribution can be approximated by the local damage cross section (see eq. (221)) according to

$$f_{FP}(x,E) \approx n\sigma_D(x,E) \tag{226}$$

which, in view of the pathlength integration of eq. (222), holds strictly if the ion trajectory can be identified with a straight line at sufficiently high energy and/or ion mass, and if the *x* coordinate is taken along the direction of ion incidence.

10.1.2 Computer Simulation

The study of radiation damage has been the primary goal of the earliest computer simulations involving energetic particles. BCA simulations (see sect. 6.1) allow a convenient and detailed calculation of the local distributions of generated Frenkel pairs from the protocol of the generated recoils whose start energy exceeds the displacement threshold. A vacancy is then generated at the original site of the recoil, whereas the location of the corresponding interstitial results as the endpoint of the trajectory of the recoil.

TRIM[47,69] offers two routes for the generation of defect distributions. The full-cascade option traces all recoils and constructs the vacancy and interstitial distributions from the start and end positions of the recoils, respectively. This has been chosen for the low-energy vacancy distribution given in Fig. 33(b). In an alternative fast option, only the primary collisions are treated, and the modified Kinchin-Pease formula, eq. (219), is used to calculate the local vacancy production from the energy transfer to the primary recoil. This procedure is adequate if the recoil pathlengths are small compared to the ion range, such as at high ion energy (see Fig. 33(d)). The simulated vacancy distributions reflect the shape of the damage function. As mentioned in sect. 8.1, they peak at a smaller depth than the ion range distributions, and exhibit a significant asymmetry towards the surface at sufficiently high ion energy.

For certain applications, the net defect distribution, i.e. the local excess of interstitials or vacancies, is important. The underlying idea is the recombination of close interstitial-vacancy pairs at sufficiently high defect concentration either during implantation (see also sect. 10.3) or subsequent thermal annealing, so that only the excess point defects of either kind remain. Their concentration can also be obtained from full-cascade TRIM simulation, by merely subtracting vacancy and interstitial distributions which have been collected at sufficient statistical quality. An example is shown in Fig. 61[182]. Due to the forward momentum of the incident ions, the recoils move in average slightly in forward direction (which is neglected in linear cascade theory by the assumption of isotropy). This results in a slight excess of vacancies closer to the surface and of interstitials towards the bulk. (The number of excess interstitials or vacancies is 3-4 orders of magnitude below the number of initially generated Frenkel pairs.) The crossover depth is slightly below the mean projected range in the present example. During thermal annealing, the the excess vacancy distribution will shrink due to diffusion to the surface and recombination with excess interstitials, thus leaving a vacancy distribution which is centered around half of the mean projected range. Therefore, correspondingly observed vacancy-type defects have often been denoted as "$R_p/2$" defects[183].

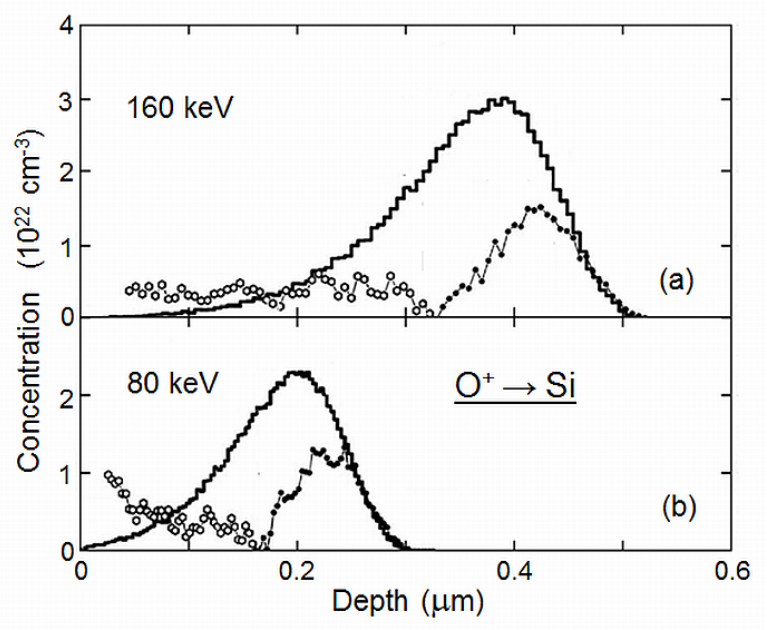

Fig. 61. Depth profiles of implanted ions (histograms), excess vacancies (open circles) and interstitials (dots) for oxygen implantations into silicon at 160 keV, $5.3 \cdot 10^{17}$ cm^{-2} (a) and 80 keV, $3 \cdot 10^{17}$ cm^{-2} (b), as obtained from TRIM binary collision simulation. The total number of generated Frenkel defects is ~920 and ~1320 per implanted ion at 80 keV and 160 keV, respectively. (After ref.[182])

10.2 Damage and Thermal Spikes

In contrast to the above case of light ion irradiation (see Fig. 60), the linear cascade prediction significantly overestimates the damage production by heavy ions. A damage efficiency ξ_D can be defined as the ratio of the experimentally observed Frenkel pair yield and the one predicted by linear cascade theory, i.e.

$$Y_{FP}^{\exp} = \xi_D Y_{FP} \tag{227}$$

In Fig. 62, the damage efficiency is plotted versus a characteristic energy transfer in primary collision, $T_{1/2}$, being implicitly defined by eq. (221) as the upper limit of the integral, for which 50% of the total Frenkel pair yield is obtained[184]. $T_{1/2}$ can be regarded as a qualitative measure of the subcascade density. Whereas the cascade efficiency for hydrogen is close to 1 (the deviation is within the theoretical and experimental uncertainty), it drops to about 0.3 for the heaviest ions under the present conditions.

Fig. 62. Damage efficiency vs. the characteristic energy transfer in primary collisions (see text), from low-temperature irradiation of copper with different ions and subsequent resistivity measurements (data points). The line is drawn to guide the eye. A damage efficiency of 1 corresponds to the linear cascade prediction of eq. (222). (After ref.[184])

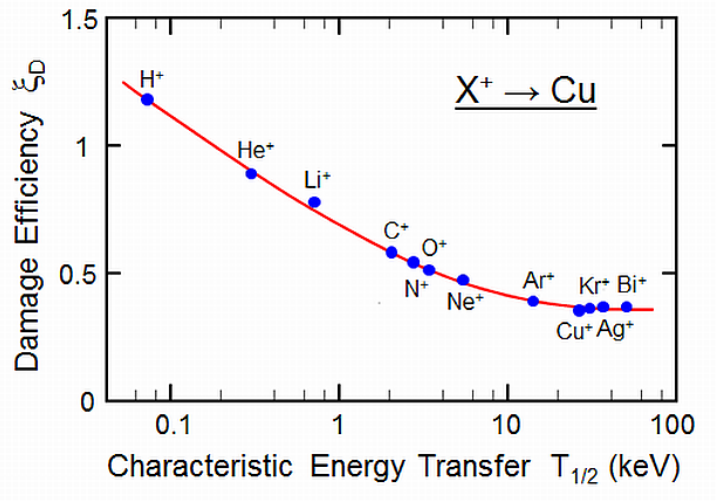

This is attributed to an influence of elastic thermal spikes[184]. In this picture, the net defect production results from generation in the cascade and dynamic annealing in the thermal spike. Recalling the discussion at the beginning of sect. 8, also the linear cascade is finally dissipated in a spike. Only the heaviest ions can induce elastic thermal spikes which result in sputtering as discussed in sect. 9, at temperatures which allow the surface binding energy of ~5 eV to be overcome. However, much lower activation energies are required for the atomic rearrangement of metastable configurations like Frenkel pairs in metals. Interstitial atoms are known to migrate already at a temperature of a few ten K. Thus, it is well conceivable that the activation even in a sub-eV thermal spike may cause a significant reduction of the Frenkel pair yield by transient interstitial diffusion and annihilation with vacancies. This explains qualitatively the reduced damage efficiency even for rather light ions (see. Fig. 62).

In principle, it cannot be excluded that elastic thermal spikes at sufficiently high nuclear energy deposition could enhance the defect production as for sputtering, in particular in materials with poor thermal diffusivity. This, however, would require an unrealistically high deposited energy density in view of the large displacement threshold energy as compared to the surface binding energy in sputtering. In addition, simultaneous dynamic annealing might obscure the effect. Consequently, an enhancement of defect production by an elastic thermal spike has not been reported.

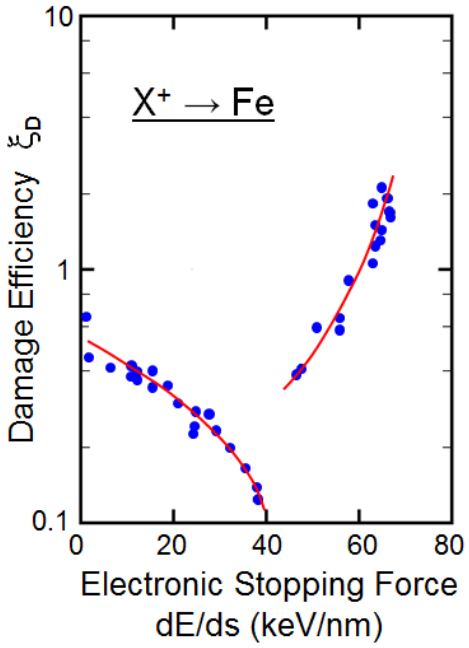

Fig. 63. Damage efficiency vs. electronic stopping force for different swift heavy ions incident on iron at energies between 0.1 and 4.5 GeV, after ref.[185]. The data result from low-temperature resistivity measurements after irradiation. The lines are drawn to guide the eye.

The reduction of damage production in metals has also been confirmed for high-energy swift ion irradiation. An example is shown in Fig. 63[185]. At an electronic stopping force lower than 40 keV/nm, the defect production continuously decreases. This can be explained by dynamic annealing in an inelastic thermal spike[186], which acts in a similar way as the elastic thermal spike above. However, a clearly distinct second regime is entered at higher electronic stopping force, with a prominent increase of the damage production. This can again be attributed to the inelastic thermal spike, the temperature of which, however, becomes sufficiently high to locally melt the material[186]. As the volume of the melt increases at increasing electronic energy deposition, recrystallisation may lead to an increasing amount of remaining extended defects around the ion trajectory. (Physically, the definition of the damage efficiency, which moreover attains values exceeding 1, is then no longer meaningful.)

Damage induced by single swift heavy ions is also manifested by the appearance of cylindrical nanometric “ion tracks”, within which the material is structurally transformed. Such tracks have

been found in many different materials (see reviews by Fleischer et al.[187], Toulemonde et al.[188] and Klaumünzer[189]). Early models of the track formation have invoked the mechanism of "Coulomb explosion". Ionization by the incident ion generates a high density of fast electrons, which are transported away from the ion trajectory and thus leave a highly ionized core, in which the atomic cores could be radially accelerated. However, this picture had to be discarded in view of the femtosecond electronic relaxation times which do not leave time for a significant atomic relocation. Instead, the presently preferred interpretation is the inelastic thermal spike model as described in subsection 8.2.2, assuming that the structural transformation results from local melting in the track. However, a unified and generally accepted picture, which would be valid for the variety of all materials, has not been established up to date. It should also be noted that the inelastic thermal spike model is subjected to considerable uncertainties and inconsistencies[189].

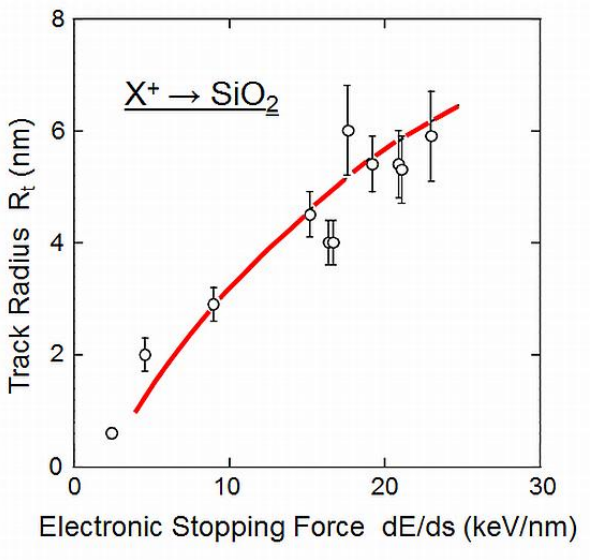

Fig. 64. Radii of amorphous ion tracks for different swift heavy ions incident on crystalline quartz vs. electronic stopping. The line results from inelastic thermal spike calculations according to eqs. (177) and (178) with an electronic mean diffusional pathlength of 3.8 nm as fitting parameter. (After ref.[163])

Fig. 64 shows an example for the irradiation of crystalline quartz[163]. A good fit is obtained from the inelastic thermal spike model with best available thermophysical data from literature, and the mean free diffusional pathlength of the electrons as fit parameter. Another recent example (see Fig. 65) is given for the irradiation of vitreous silica with gold ions in a wide range of energies[190]. Here, the nuclear energy deposition has been included into the thermal spike modeling by adding a corresponding source term to eq. (178). A good fit is again obtained over the energy range where data are available, demonstrating the synergism of track generation by both elastic and inelastic thermal spikes.

It should be mentioned that Szenes[191,192] has formulated a simple "analytical" thermal spike model for track formation which is based on eq. (179) and thus turns the total deposited energy directly into atomic motion. Additional semi-empirical parameters are introduced with useful trends to predict the track formation in different materials. However, any additional physical understanding of the mechanism of track formation is not provided.

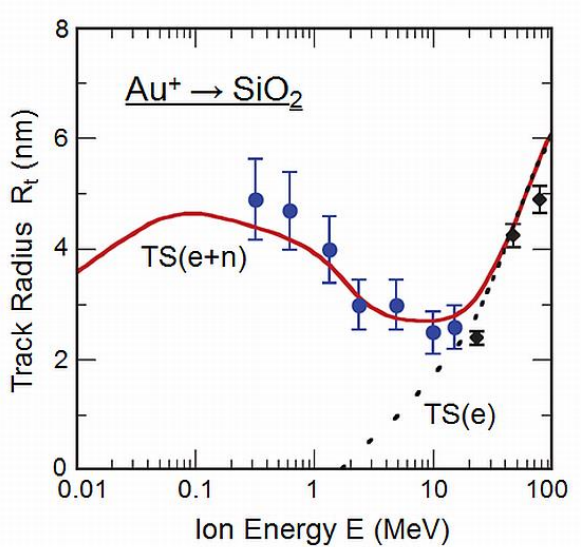

Fig. 65. Track radii of structural modification induced by energetic gold ions incident on vitreous SiO_2. The data (symbols) have been obtained indirectly by the determination of the damage cross section σ_D from irradiations at increasing fluence (see sect. 10.3), and deriving the track radius according to $R_t = \sqrt{\sigma_D/\pi}$. The dotted and solid lines show the predictions from the elastic thermal spike model, eqs. (177) and (178), for electronic energy deposition alone (TS(e)) and including nuclear energy deposition (TS(e+n)), respectively, with an electronic mean diffusional pathlength of 3 nm as fitting parameter. The electronic stopping data have been taken from SRIM[69] (2008 version) with reciprocity corrections according to Sigmund[74] (see subsection 4.5.2). (After ref.[190])

As for sputtering, molecular dynamics simulations are in particular helpful for the description of spike phenomena. An example is shown in Fig. 66[193] which shows a number of different features with respect to damage generation. On a time scale of a few ps, a strongly disordered zone is created with an initial liquid-like appearance (Fig. 66(a,b)) with core temperatures exceeding 6000 K. Subsequently, a cavity develops in the center which is surrounded by a densified liquid (Fig. 66(b,c)). This confirms the early picture of Brinkman[194] that the cascade forms a vacancy-rich core and interstitials preferentially in its outer region. Fig. 66(b) also indicates the emission of a focused collision sequence as well as some shock waves. During the cooling-down phase of several 10 ps, the system returns first to a liquid core, and finally leaves mainly extended defects such as dislocations in the bulk, with numerous vacancy-like defects. In addition, the re-solidification results in a protrusion at the surface, which largely compensates the bulk vacancies, as only four sputtered atoms have been recorded for this simulated event. Thus, the presence of the surface is of significant influence on the generation of radiation damage at sufficiently low ion energy. In the specific event, only three isolated interstitials are found to remain. This is qualitatively consistent with the low damage efficiency as described above, and confirms the dynamic annealing in the elastic thermal spike. (It should also be noted that any sputter crater is not observed at the present energy of 10 keV, in contrast to Fig. 54, which was obtained at 100 keV. This is consistent with the significantly lower sputter yield here.)

10.3 Damage Accumulation

Under irradiation, target atoms are continuously displaced, and repeatedly displaced at sufficiently high ion fluence. If crystalline effects are neglected, the total number of displacements per unit volume, c_D, increases linearly with the ion fluence. Looking at a sufficiently thin irradiated slab of matter so that energy loss can be neglected, the number of total displacements per atom of the irradiated volume can be written as (see eq. (226))

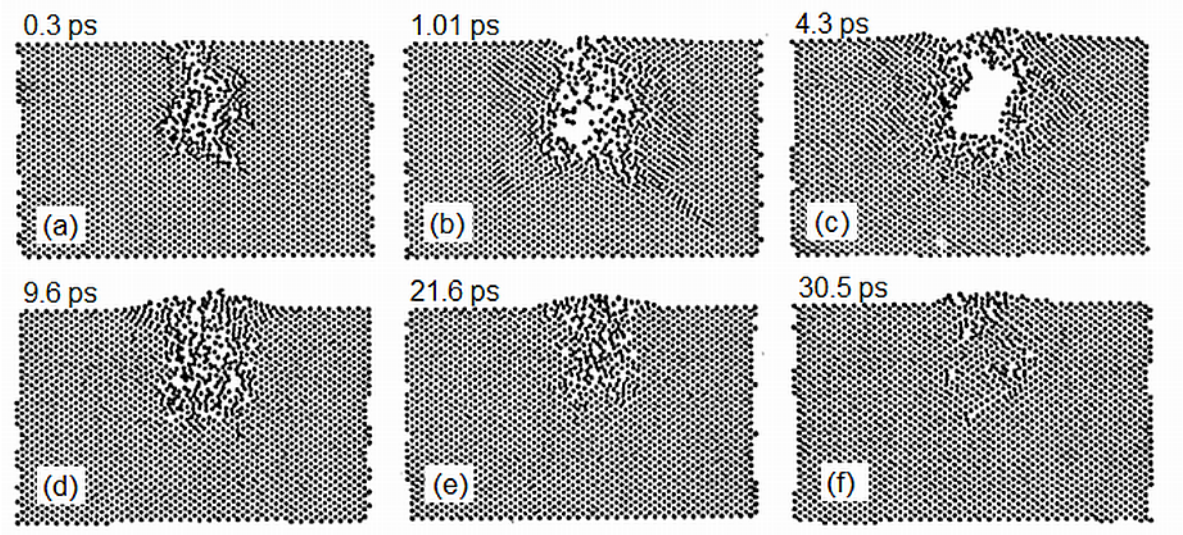

Fig. 66. Snapshots of the development of atomic motion after incidence of a 10 keV Au ion onto an Au(001) surface, as generated by molecular dynamics computer simulation. The angles of incidence were chosen to avoid channeling, with a polar angle of 20° with respect to the surface normal, and an azimuthal angle of 160° with respect to the <100> direction. The frames (a-f) show a cross-sectional slab of one atomic layer thickness, viewed along the <100> direction, at the indicated times after ion incidence. (After ref.[193])

$$q_D(\Phi) = \frac{c_D(\Phi)}{n} = \frac{\Phi}{n} f_{FP} = \Phi \sigma_D \tag{228}$$

From this, the ion fluence is often expressed in units of displacements per atom (dpa), i.e. $\Phi_{dpa} = \Phi \sigma_D$ with $\Phi_{dpa} = 1\,\text{dpa}$ if each atom has been displaced once in average.

However, at increasing fluence newly generated interstitials increasingly recombine with previously accumulated vacancies and vice versa. Thus, the increase of the volume concentration of Frenkel pairs, c_{FP}, saturates according to[184]

$$\frac{\partial c_{FP}(\Phi)}{\partial \Phi} = n\sigma_D\left(1 - 2V_r c_{FP}(\Phi)\right) \tag{229}$$

where V_r denotes the recombination volume. For an initially undamaged material, the solution is

$$c_{FP}(\Phi) = \frac{1}{2V_r}\left[1 - \exp\left(-2V_r n \sigma_D \Phi\right)\right] \tag{230}$$

which saturates at a maximum concentration of $(2V_r)^{-1}$, which depends on the specific material.

The maximum defect concentration in pure metals is typically a few percent. Other materials, like crystalline semiconductors, accumulate damage up to full amorphization. In a simple model, amorphization may be defined by the condition that each atom in the irradiated volume has been displaced once. Assuming a homogeneous damage function with the affected depth being approximately equal to the mean projected ion range, the fluence which is necessary for amorphization can be estimated by

$$\Phi_{am}(E) = \frac{n\bar{R}_p(E)}{Y_{FP}(E)} \approx \frac{2nU_d\bar{R}_p(E)}{E} \tag{231}$$

where eq. (223) has been used. This predicts rather well the critical fluence of amorphization of silicon under irradiation at room temperature or below, although the detailed mechanism of amorphization is much more complicated than a simple accumulation of point defects (for a recent review, see ref.[195]).

For ion implantation into single crystals, the accumulation of defects may alter the range distribution at increasing fluence. This becomes in particular visible for the irradiation under channeling conditions, where the dechanneling at defects becomes increasingly significant. This is demonstrated in Fig. 34(b), where the channeling tail, which is formed at low fluence in the initially perfect crystal, remains essentially unaltered at higher fluences. In turn, dechanneling at defects results in an increasing amount of random trajectories, so that at the highest fluence more than 95% of the implant distribution resembles the range distributions in the amorphous material.

11 Ion Mixing

In an inhomogeneous multicomponent substance, the relocation of atoms due to ion irradiation results in "mixing" of the atoms[196-198]. Prototypes of such materials are a thin marker of foreign atoms in an otherwise homogeneous material, which is broadened under irradiation, or a stack of two homogeneous layers of different materials, the interface of which is blurred under irradiation. First restricting to a marker system, the relocation of the marker atoms can be described by a relocation cross section $d\sigma(x,z)$, which describes the displacement of a marker atom from its original depth *x* by a depth increment *z* along the depth axis. For ion irradiation with a fluence Φ, ion mixing becomes a process of multiple relocation. The mean displacement of the marker is given by

$$< \Delta x >= \Phi \int_z z d\sigma(x,z) \tag{232}$$

for sufficiently small relocations so that the cross section does not change markedly, i.e. if the relative energy loss of the impinging ions in the region of interest is sufficiently small. The variance of the relocation distribution results as

$$\Omega_m^2 = < \left(\Delta x - < \Delta x >\right)^2 >= \Phi \int_z z^2 d\sigma(x,z) \tag{233}$$

The integral on the right-hand side is often denoted as mixing parameter

$$M = \int_z z^2 d\sigma(x,z) \tag{234}$$

With eqs. (232) and (233), a Gaussian marker distribution centered around $< \Delta x >$ and with the standard deviation Ω_m can be constructed in first order.

In case of a bilayer system, the mixing profile is correspondingly error-functional. However, as atoms of the upper layer are mixed into the lower one and vice versa, the standard deviation of the error function becomes $\sqrt{2}\Omega_m$ if symmetric mixing is assumed.

In literature, ion mixing is often quantified in analogy to diffusional broadening or intermixing with a diffusion coefficient *D*, which, for an irradiation time *t*, exhibits a variance of $2Dt$ or $4Dt$

for a marker system and a bilayer system, respectively, with respective mixing parameters $M = 2Dt/\Phi$ and $M = 4Dt/\Phi$.

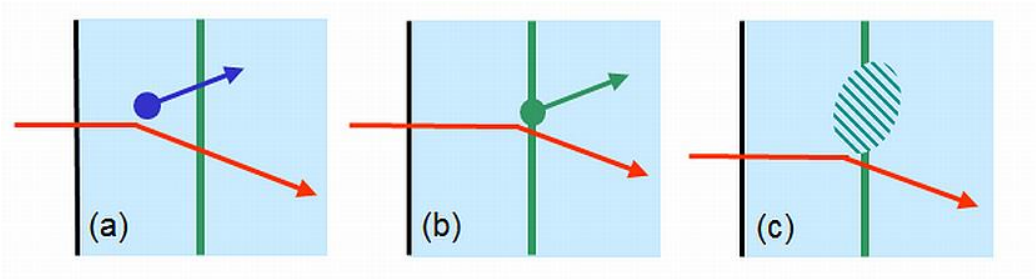

Fig. 67. Mechanisms of ion mixing in a marker layer system: Matrix relocation (a), marker relocation (b) and cascade mixing of the marker (c)

11.1 Collisional Mixing

In the collisional picture, ion mixing turns out to be a rather complicated process[199]. Basically, there are three mechanisms as indicated in Fig. 67 for a marker system. Matrix atoms can be relocated by primary collisions into or beyond the marker, which results in marker broadening and a shift towards the surface (Fig. 67(a)). Marker atoms, which are relocated by primary collisions towards larger depth, form a tail of the marker profile, and thereby contribute to broadening and a shift towards the bulk (Fig. 67(b)). Finally, collision cascades initiated by sufficiently large primary energy transfers to marker atoms are more or less isotropic and cause mainly a broadening of the marker (Fig. (67(c)). These processes interact in a complicated way.

For cascade mixing, the cascades mainly develop by matrix atoms, as the number of marker atoms is small. Collisions with the marker atoms thus cause the latter to be relocated. In the notation of sects. 8.1 and 9.1.1 for the cascade atoms, the relocation cross section is given by[199]

$$\begin{aligned}\frac{d\sigma(x,z)}{dz} = \int dE_0 \int d\Omega_0 \int d\vec{f}\, \frac{1}{4\pi} F(E,\vec{\eta},E_0,\vec{r})\vec{\eta}_0 \\ \times \frac{1}{\cos\theta_0} \int d\sigma_M(E_0,\vec{\eta}_0,T,\vec{\eta}')\, f_R(T,\vec{\eta}',z)\end{aligned} \tag{235}$$

Here, the first line denotes the flux of matrix cascade atoms through the marker plane at depth *x*. The second line contains the probability of collisions $d\sigma_M$ with marker atoms, which receive an energy transfer *T* at a direction $\vec{\eta}'$. The cosine term reflects the increased collision probability at an inclined direction of the matrix atoms. f_R denotes the projected range distribution of the marker recoil atoms. Similarly as for the treatment of sputtering (see subsection 9.1.1), the area integral of the cascade function *F* can be written as

$$\int d\vec{f}\, \frac{1}{4\pi} F(E,\vec{\eta},E_0,\vec{r})\vec{\eta}_0 = \frac{6}{4\pi^3} \frac{f_D(E,\eta,x)}{E_0 n S_n(E_0)} |\cos\theta_0| \tag{236}$$

For power law scattering, again with $s \to \infty$, the evaluation yields together with eq. (234)

$$M = \frac{2\gamma}{\pi^2} S_n(\bar{E}) \frac{\left(\bar{R}_p(U_m)\right)^2}{U_m} \tag{237}$$

where $S_n(\bar{E})$ denotes the nuclear stopping cross section of the incident ions, taken at their mean energy at the depth of the marker, U_m a relocation threshold energy for the marker atoms, and $\bar{R}_p(U_m)$ their mean projected range at the threshold energy.

The definition of the threshold energy is questionable to some extent. It can be assumed to be significantly smaller than the damage threshold energy U_d, as replacement sequences may influence the relocation more than the Frenkel pair formation. Further, in contrast to the formation of isolated Frenkel pairs for which U_d is defined, ion mixing is a high-fluence phenomenon, so that the material can be assumed to be already heavily damaged. Stable relocation might then result from much smaller initial recoil energies than stable Frenkel pair formation in an undisturbed lattice. In the absence of better knowledge, $U_m \approx 8\,\text{eV}$ is recommended from experience with dynamic BCA simulations in comparison to experiments[102].

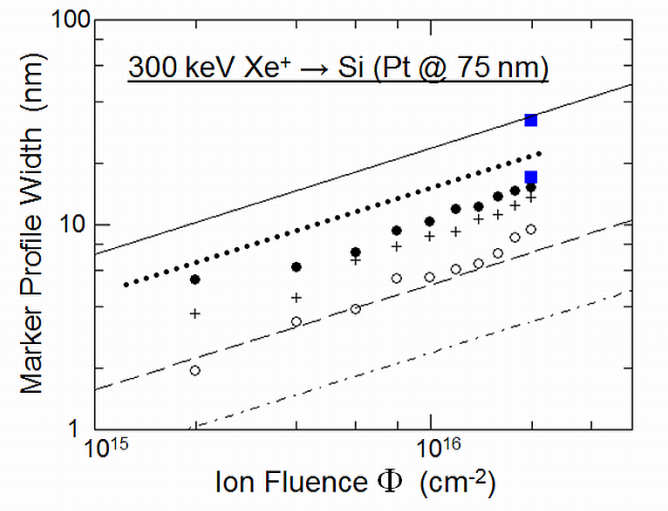

Fig. 68. Theoretical predictions and computer simulation results for ion mixing of a thin Pt marker in Si by 300 keV Xe irradiation. The thin lines display results from linear cascade theory[199] for multiple matrix relocation (solid line; root-mean-square (RMS) data), multiple marker relocation (dashed line; RMS data) and cascade mixing (dashed-dotted line; half-width-at-half-maximum (HWHM) data). For the latter, a relocation threshold energy of 7.83 eV and an associated mean projected range of 0.3 nm have been assumed (see eq. (237)). The small symbols show HWHM results from TRIDYN BCA computer simulation with relocation threshold energies of 4 eV (full dots), 8 eV (crosses) and 25 eV (open dots). Squares are from different experimental HWHM data. The dotted line represents a fit through experimental RMS data obtained at a marker depth of 50 nm. (After ref.[200]; for the experimental data, see references therein)

Although the choice of U_m sets another input parameter with some associated uncertainty, dynamic BCA simulations have proven to be a powerful tool for ion mixing calculations (see, e.g., refs.[102,200-203]). Fig. 68 shows an early comparison[200] of TRIDYN results with analytical predictions and experimental data The analytical prediction of eq. (237)[199] underestimates the experimental data significantly, as it only covers isotropic cascade mixing. For matrix and marker relocation, the analytical theory provides only root-mean-square results which probably largely overestimate the half-width of the distributions. The TRIDYN results obtained with the lower displacement thresholds are in rather good agreement with the experimental data.

11.2 Chemical Effects on Ion Mixing

Even if the quantitative prediction of collisional ion mixing remains unsatisfactory as described above, collisional mixing in systems involving similar atomic masses would be expected to be of similar magnitude. In contrast, experiments in particular with metallic bilayer systems clearly demonstrate additional effects (see refs.[196,197] and references therein) which are attributed to chemical interaction of the atoms during the dissipation of the collision cascade. At mean energies in the eV regime, interaction forces between atoms of the same or different species come into play which influence the local configuration after thermalization, and thereby the average transport which results in intermixing. The interaction of the atoms in a compound can be described by the enthalpy of mixing, ΔH_{mix}, which denotes the heat of formation of the compound from its constituents (taken as negative for an exothermic reaction). Further, the cohesive energy ΔH_{coh} of the compound is of influence which represents the average enthalpy of sublimation of the compound. Qualitatively, it would thus be expected that ion mixing increases at decreasing enthalpy of mixing and increasing cohesive energy, which is indeed observed experimentally (see refs.[204,205], respectively).

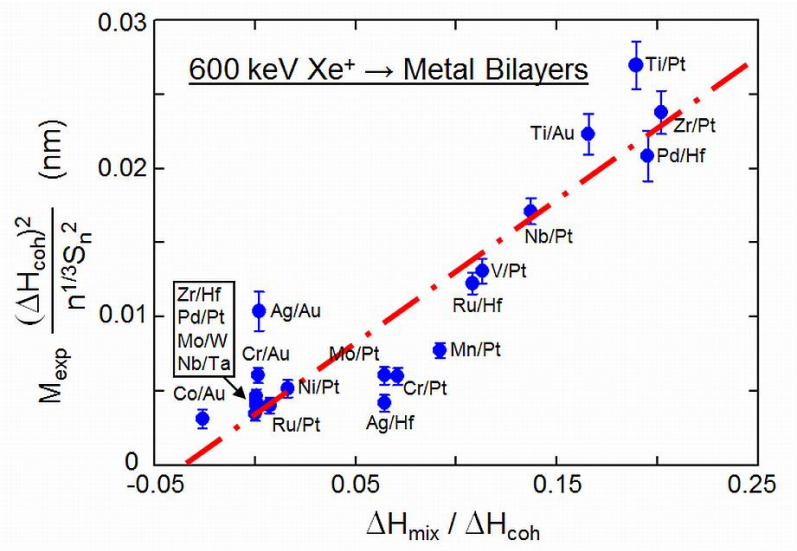

Fig. 69. Universal description of the influence of chemical driving forces on collisional mixing. The data points represent experimental mixing parameters M_{exp} for numerous bilayer systems which have been irradiated with 600 keV Xe ions. The ordinate is scaled according to eq. (238), the line represents the corresponding fit. ΔH_{mix} and ΔH_{coh} denote the mixing enthalpy and the cohesive energy, respectively, n the average atomic density and S_n the nuclear stopping cross section. (After ref.[196]; see refs.[196,206] and references therein)

Based on a standard model of diffusion under chemical driving forces, Johnson et al.[206] proposed a semi-empirical formula for the mixing parameter in a bilayer system according to

$$M = K_1 n^{1/3} \left(\frac{S_n(\bar{E})}{\Delta H_{coh}} \right)^2 \left(1 + K_2 \frac{\Delta H_{mix}}{\Delta H_{coh}} \right) \qquad (238)$$

where n denotes the average atomic density of the bilayer materials, and with constants $K_1 = 0.0037$ nm and $K_2 = 27$ which show universal validity for many metallic elemental bilayer pairs. This is confirmed in Fig. 69.

11.3 Thermal Spike Mixing

The above evidence of the effect of chemical driving forces on collisional ion mixing already implies the role of a low-energy (~eV) elastic thermal spike within which transient diffusion results in atomic transport. There is also clear evidence of the role of inelastic thermal spikes for swift heavy ion irradiation in the electronic stopping regime.

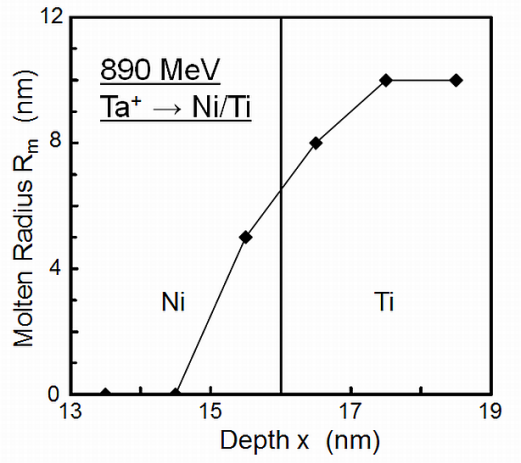

Fig. 70. Molten track formation in a bilayer stack of 16 nm Ni and 14 nm Ti on Si under irradiation with 890 MeV Ta ions, as obtained from inelastic thermal spike calculations. (After ref.[208])

As an example, the mixing in Ni-Ti bilayer and trilayer systems has been investigated in detail by Leguay et al.[207]. Their data were later interpreted by Wang et al.[208] on the basis of the inelastic thermal spike model (section 8.2.2), by attributing the mixing to interdiffusion in the molten track around the ion. An example from the thermal spike calculations is shown in Fig. 70 for the irradiation of a Ni/Ti bilayer. Under the given experimental conditions and with the thermophysical properties of the metals, a molten track will not form in pure Ni but in pure Ti, as the initial electronic energy density is significantly higher in Ti. The transfer of electronic energy across the interface due to the electron temperature gradient, and the subsequent electron-phonon interaction enables melting in the Ni interface region as well.

Fig. 71. Mixing parameter versus the electronic stopping force in the top layer, for irradiation of three different oxides on SiO_2. The lines are from linear fits with corresponding threshold stopping forces. (After ref.[209])

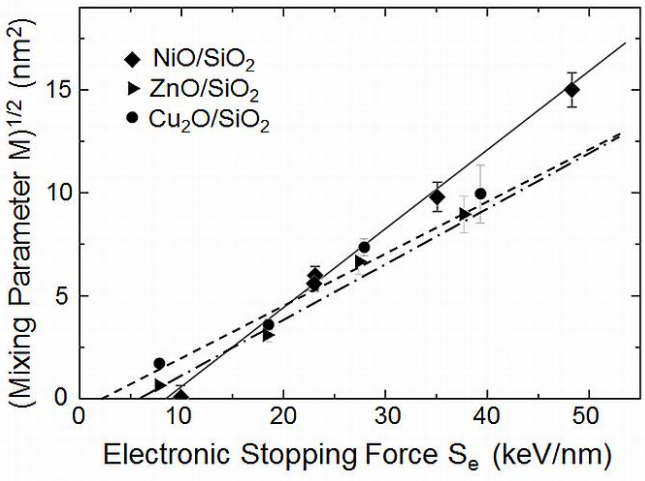

The correlation of ion beam mixing with the formation of a molten track across the interface has also been established for covalent and ionic compounds (see ref.[209] and references therein). For the examples of Fig. 71, the mixing is critically determined by the stopping in the top oxide layers as the SiO_2 backing is more easily liquefied. The mixing parameter scales quadratically with the stopping force above a certain threshold which is characteristic for the material, and which is associated with the formation of the molten track.

References

1. Rutherford, E.: The Scattering of alpha and beta particles by matter and the structure of the Atom. Philos Mag **21**, 669-688 (1911)

2. Thomson, J.J.: Ionization by moving electrified particles. Philos Mag **23**, 449-457 (1912)

3. Bohr, N.: On the theory of the decrease of velocity of moving electrified particles on passing through matter. Philos Mag **25**, 10-31 (1913)

4. Bohr, N.: On the decrease of velocity of swiftly moving electrified particles in passing through matter. Philos Mag **30**, 581-612 (1915)

5. Born, M.: Quantum mechanics in impact processes. Z Phys **38**, 803-840 (1926)

6. Bethe, H.: The theory of the passage of rapid neutron radiation through matter. Ann Phys-Berlin **5**, 325-400 (1930)

7. Bothe, W.: Theory of the diffusion of alpha-rays on small angles. Z Phys **4**, 300-314 (1921)

8. Bohr, N.: Scattering and stopping of fission fragments. Phys Rev **58**, 654-655 (1940)

9. Bohr, N.: Velocity-range relation for fission fragments. Phys Rev **59**, 270-275 (1941)

10. Bohr, N.: The penetration of atomic particles through matter. Matematisk-fysiske Meddelelser, vol. **18**,8 (1948)

11. Lindhard, J., Nielsen, V., Scharff, M.: Approximation methods in classical scattering by screened Coulomb fields (Notes on atomic collisions, I). Matematisk-fysiske Meddelelser, vol. **36**,10 (1968)

12. Lindhard, J., Scharff, M., Schiøtt, H.E.: Range concepts and heavy ion ranges (Notes on atomic collisions, II). Matematisk-fysiske Meddelelser, vol. **33**,14 (1963)

13. Lindhard, J., Nielsen, V., Scharff, M., Thomsen, P.V.: Integral equations governing radiation effects (Notes on atomic collisions, III). Matematisk-fysiske Meddelelser, vol. **33**,10 (1963)

14. Gibson, J.B., Goland, A.N., Milgram, M., Vineyard, G.H.: Dynamics of radiation damage. Phys Rev **120**, 1229-1253 (1960)

15. Robinson, M.T., Torrens, I.M.: Computer simulation of atomic-displacement cascades in solids in binary-collision approximation. Phys Rev B **9**, 5008-5024 (1974)

16. Carter, G., Grant, W.A.: Ion implantation of semiconductors. Contemporary electrical engineering. Arnold, London (1976)

17. Seitz, F., Koehler, J.S.: Displacement of atoms during irradiation. Solid State Physics - Advances in Research and Applications **2**, 305-448 (1956)

18. Thompson, M.W.: Defects and radiation damage in metals. Cambridge monographs on physics. Cambridge Univ. Press, Cambridge (1969)

19. Peterson, N.L., Harkness, S.D. (eds.): Radiation damage in metals. American Society for Metals, Metals Park, Ohio (1976)

20. Sigmund, P.: Theory of sputtering I. Sputtering yield of amorphous and polycrystalline targets. Phys Rev **184**, 383-416 (1969)

21. Torrens, I.M.: Interatomic potentials. Acad. Press, New York NY (1972)

22. Sigmund, P.: Collision theory of displacement damage, ion ranges and sputtering I. Rev Roum Phys **17**, 823-870 (1972)

23. Sigmund, P.: Collision theory of displacement damage, ion ranges and sputtering II. Rev Roum Phys **17**, 969-1000 (1972)

24. Sigmund, P.: Collision theory of displacement damage, ion ranges and sputtering III. Rev Roum Phys **17**, 1079-1106 (1972)

25. Sigmund, P.: Stopping of heavy ions: a theoretical approach. Springer tracts in modern physics, vol. 204. Springer, Berlin (2004)

26. Sigmund, P.: Particle penetration and radiation effects: general aspects and stopping of swift point charges. Springer series in solid-state sciences, vol. 151. Springer, Berlin (2006)

27. Behrisch, R. (ed.): Physical sputtering of single-element solids. Sputtering by Particle Bombardment, vol. 1. Springer, Berlin (1981)

28. Behrisch, R. (ed.): Sputtering of alloys and compounds, electron and neutron sputtering, surface topography. Sputtering by Particle Bombardment, vol. 2. Springer, Berlin (1983)

29. Behrisch, R. (ed.): Characteristics of sputtered particles, technical applications. Sputtering by Particle Bombardment, vol. 3. Springer, Berlin (1991)

30. Behrisch, R., Eckstein, W. (eds.): Sputtering by particle bombardment: experiments and computer calculations from threshold to MeV energies. Topics in applied physics, vol. 110. Springer, Berlin (2007)

31. Eckstein, W.: Computer simulation of ion-solid interactions. Springer series in materials science, vol. 10. Springer, Berlin (1991)

32. Smith, R. (ed.): Atomic and ion collisions in solids and at surfaces: theory, simulation and applications. Cambridge Univ. Press, Cambridge (1997)

33. Nastasi, M., Mayer, J.W., Hirvonen, J.K.: Ion solid interactions: fundamentals and applications. Cambridge solid state science series. Cambridge Univ. Press, Cambridge (1996)

34. Sigmund, P. (ed.): Ion beam science: solved and unsolved problems Pt. 1. Matematisk-fysiske Meddelelser, vol. **52**,1 (2006)

35. Sigmund, P. (ed.): Ion beam science: solved and unsolved problems Pt. 2. Matematisk-fysiske Meddelelser, vol. **52**,2 (2006)

36. Bernas, H. (ed.): Materials science with ion beams. Topics in applied physics, vol. 116. Springer, Berlin (2010)

37. Thomas, L.H.: The calculation of atomic fields. P Camb Philos Soc **23**, 542-548 (1927)

38. Fermi, E.: A statistical method for determining some properties of the atoms and its application to the theory of the periodic table of elements. Z Phys **48**, 73-79 (1928)

39. Gombas, P.: Statistische Behandlung des Atoms. In: Fluegge, S. (ed.) Handbuch der Physik, Band XXXVI. Berlin (1959)

40. Moliere, G.: Theorie der Streuung schneller geladener Teilchen 1. Z Naturforsch A **2**, 133-145 (1947)

41. Lenz, W.: About the applicability of the statistical method to ion lattice. Z Phys **77**, 713-721 (1932)

42. Jensen, H.: The charge distribution in ions and the lattice constant of rubidium by the static method. Z Phys **77**, 722-745 (1932)

43. Firsov, O.B.: Interaction energy of atoms for small nuclear separations. Sov Phys JETP-USSR **5**, 1192-1196 (1957)

44. Firsov, O.B.: Calculation of the interaction potential of atoms. Sov Phys JETP-USSR **6**, 534-537 (1958)

45. Wilson, W.D., Haggmark, L.G., Biersack, J.P.: Calculations of nuclear stopping, ranges, and straggling in low-energy region. Phys Rev B **15**, 2458-2468 (1977)

46. Wilson, W.D., Bisson, C.L.: Inert gases in solids - interatomic potentials and their influence on rare-gas mobility. Phys Rev B **3**, 3984-1992 (1971)

47. Ziegler, J.F., Biersack, J.P., Littmark, U.: The Stopping and range of ions in solids. The Stopping and ranges of ions in matter, vol. 1. Pergamon Press, New York, NY (1985)

48. Lindhard, J.: Influence of crystal lattice on motion of energetic charged particles. Matematisk-fysiske Meddelelser, vol. **34**,14 (1965)

49. Winterbon, K.B., Sigmund, P., Sanders, J.B.: Spatial distribution of energy deposited by atomic particles in elastic collisions. Matematisk-fysiske Meddelelser, vol. **37**,14 (1970)

50. Loftager, P., Besenbacher, F., Jensen, O.S., Sorensen, V.S.: Experimental-study of effective inter-atomic potentials. Phys Rev A **20**, 1443-1447 (1979)

51. Sigmund, P.: Stopping power: Wrong terminology. ICRU News **1** (2000)

52. Matsunami, N., Yamamura, Y., Itikawa, Y., Itoh, N., Kazumata, Y., Miyagawa, S., Morita, K., Shimizu, R.: A semi-empirical formula for the energy-dependence of the sputtering yield. Radiat Eff Lett **57**, 15-21 (1980)

53. Bohr, N., Lindhard, J.: Electron capture and loss by heavy ions penetrating through matter. Matematisk-fysiske Fys Meddelelser, vol. **28**,7 (1954)

54. Northcliffe, L.C.: Passage of heavy ions through matter. Ann Rev Nucl Sci **13**, 67-102 (1963)

55. Betz, H.D., Hortig, G., Leischner, E., Schmelzer, C., Stadler, B., Weihrauch,J.: Average charge of stripped heavy ions. Phys Lett **22**, 643-644 (1966)

56. Betz, H.D.: Charge states and charge-changing cross-sections of fast heavy-ions penetrating through gaseous and solid media. Rev Mod Phys **44**(3), 465-539 (1972)

57. Brandt, W., Kitagawa, M.: Effective stopping-power charges of swift ions in condensed matter. Phys Rev B **25**, 5631-5637 (1982)

58. Nikolaev, V.S., Dmitriev, I.S.: On equilibrium charge distribution in heavy element ion beams. Phys Lett A **28**, 277-278 (1968)

59. Shima, K., Ishihara, T., Mikumo, T.: Empirical formula for the average equilibrium charge state of heavy ions behind various foils. Nuclear Instruments & Methods in Physics Research **200**, 605-608 (1982)

60. Schiwietz, G., Czerski, K., Roth, M., Staufenbiel, F., Grande, P.L.: Femtosecond dynamics - snapshots of the early ion-track evolution. Nucl Instrum Meth B **225**, 4-26 (2004)

61. Fermi, E., Teller, E., Weisskopf, V.: The decay of negative mesotrons in matter. Phys Rev **71**, 314-315 (1947)

62. Lindhard, J., Scharff, M.: Energy dissipation by ions in keV region. Phys Rev **124**, 128-130 (1961)

63. Firsov, O.B.: A qualitative interpretation of the mean electron excitation energy in atomic collisions. Sov Phys JETP-USSR **9**, 1076-1080 (1959)

64. Hvelplund, P., Fastrup, B.: Stopping cross section in carbon of 0.2-1.5-MeV atoms with 21<Z<39. Phys Rev **165**, 408-414 (1968)

65. Oen, O.S., Robinson, M.T.: Computer studies of reflection of light ions from solids. Nucl Instrum Methods **132**, 647-653 (1976)

66. Fano, U.: Penetration of Protons, Alpha Particles, and Mesons. Ann Rev Nucl Sci **13**, 1-66 (1963)

67. Lindhard, J.: On the properties of a gas of charged particles. Matematisk-fysiske Meddelelser, vol. **28**,8 (1954)

68. Lindhard, J., Winther, A.: Stopping power of electron gas and equipartition rule. Matematisk-fysiske Meddelelser, vol. **34**,4 (1964)

69. SRIM is available at http://www.srim.org (2011)

70. Andersen, H.H., Ziegler, J.F.: Hydrogen: stopping powers and ranges in all elements. The stopping and ranges of ions in matter, vol. 3. Pergamon Press, New York (1977)

71. Ziegler, J.F.: Helium: stopping powers and ranges in all elemental matter. The stopping and ranges of ions in matter, vol. 4. Pergamon Press, New York (1977)

72. Littmark, U., Ziegler, J.F.: Ranges of energetic ions in matter. Phys Rev A **23**, 64-72 (1981).

73. Herman, F., Skillman, S.: Atomic structure calculations. Prentice-Hall, Englewood Cliffs, NJ (1963)

74. Sigmund, P.: Reciprocity in the electronic stopping of slow ions in matter. Eur Phys J D **47**, 45-54 (2008)

75. Bragg, W.H., Elder, M.A.: On the alpha particles of radium, and their loss of range in passing through various atoms and molecules. Philos Mag **10**, 318-340 (1905)

76. Piercy, G.R., Mccargo, M., Brown, F., Davies, J.A.: Experimental evidence for increase of heavy ion ranges by channeling in crystalline structure. Phys Rev Lett **10**, 399-400 (1963)

77. Lutz, H., Sizmann, R.: Super ranges of fast ions in copper single crystals. Phys Lett **5**, 113-114 (1963)

78. Morgan, D.V.: Channeling: theory, observation and applications. Wiley, London (1973)

79. Feldman, L.C., Mayer, J.W., Picraux, S.T.: Materials analysis by ion channeling: submicron crystallography. Academic Press, New York (1982)

80. Jiang, W., Grötzschel, R., Pilz, W., Schmidt, B., Möller, W.: Random and channeling stopping powers and charge-state distributions in silicon for 0.2-1.2 MeV/u positive heavy ions. Phys Rev B **59**, 226-234 (1999)

81. Bredov, M.M., Lang, I.G., Okuneva, N.M.: On the problem of penetration of medium-energy ions into matter. Sov Phys-Tech Phys **3**, 228-229 (1958)

82. Robinson, M.T., Oen, O.S.: The channeling of energetic atoms in crystal lattices. Appl Phys Lett **2**, 30-32 (1963)

83. Currie, W.M.: A Monte Carlo programme for Doppler shift analysis. Nucl Instrum Methods **73**, 173-185 (1969)

84. Möller, W., Pospiech, G., Schrieder, G.: Multiple-scattering calculations on ions passing through thin amorphous foils. Nucl Instrum Methods **130**, 265-270 (1975)

85. Biersack, J.P., Haggmark, L.G.: A Monte-Carlo computer-program for the transport of energetic ions in amorphous targets. Nucl Instrum Methods **174**, 257-269 (1980)

86. Hobler, G.: Monte-Carlo simulation of 2-dimensional implanted dopant distributions at mask edges. Nucl Instrum Meth B **96**, 155-162 (1995)

87. Schiettekatte, F.: Fast Monte Carlo for ion beam analysis simulations. Nucl Instrum Meth B **266**, 1880-1885 (2008)

88. Ziegler, J.F., Ziegler, M.D., Biersack, J.P.: SRIM - The stopping and range of ions in matter (2010). Nucl Instrum Meth B **268**, 1818-1823 (2010)

89. Hautala, M.: Nuclear stopping in polycrystalline materials - range distributions and Doppler-shift attenuation analysis. Phys Rev B **30**, 5010-5018 (1984)

90. Posselt, M.: Computer-simulation of channeling implantation at high and medium energies. Nucl Instrum Meth B **80-1**, 28-32 (1993)

91. Hobler, G., Fehlmann, G.: A study of ultra-shallow implanted dopant profiles in silicon using BC and MD simulations. Radiat Eff Defect S **141**, 113-125 (1997)

92. Biersack, J.P., Eckstein, W.: Sputtering studies with the Monte-Carlo program TRIM.SP. Appl Phys A **34**, 73-94 (1984)

93. Möller, W., Eckstein, W., Biersack, J.P.: TRIDYN - binary collision simulation of atomic collisions and dynamic composition changes in solids. Comput Phys Commun **51**, 355-368 (1988)

94. Möller, W., Eckstein, W.: TRIDYN - a TRIM simulation code including dynamic composition changes. Nucl Instrum Meth B **2**, 814-818 (1984)

95. Roush, M.L., Andreadis, T.D., Goktepe, O.F.: EVOLVE, a time-dependent Monte-Carlo code to simulate the effects of ion-beam-induced atomic mixing. Radiat Eff Defect S **55**, 119-129 (1981)

96. Chou, P.S., Ghoniem, N.M.: Collisional aspects of preferential sputtering using the Monte-Carlo method. J Nucl Mater **141**, 216-220 (1986)

97. Schönborn, A., Hecking, N., te Kaat, E.H.: Dynamic Monte-Carlo simulation of high-dose effects during ion bombardment. Nucl Instrum Meth B **43**, 170-175 (1989)

98. Biersack, J.P., Berg, S., Nender, C.: T-DYN Monte-Carlo simulations applied to ion assisted thin-film processes. Nucl Instrum Meth B **59**, 21-27 (1991)

99. Klein, K.M., Park, C.H., Tasch, A.F.: Modeling of cumulative damage effects on ion-implantation profiles. Nucl Instrum Meth B **59**, 60-64 (1991)

100. Jaraiz, M., Arias, J., Bailon, L.A., Barbolla, J.J.: Detailed computer-simulation of damage accumulation in ion irradiated crystalline targets. Vacuum **44**, 321-323 (1993)

101. Posselt, M.: Dynamic simulation of damage accumulation during implantation of BF2+ molecular ions into crystalline silicon. Nucl Instrum Meth B **102**, 167-172 (1995)

102. Möller, W., Posselt, M.: TRIDYN_FZR user manual. Wissenschaftlich-Technische Berichte, Forschungszentrum Rossendorf **FZR-317** (2001)

103. TRIDYN is available from Helmholtz-Zentrum Dresden-Rossendorf, Germany, through http://www.hzdr.de/db/Cms?pNid=310&pOid=21578 (2011)

104. Erginsoy, C., Englert, A., Vineyard, G.H.: Dynamics of radiation damage in body-centered cubic lattice. Phys Rev A-Gen Phys **133**, A595-A606 (1964)

105. Gay, W.L., Harrison, D.E.: Machine simulation of collisions between copper atom + copper lattice. Phys Rev A-Gen Phys **135**, A1780-A1790 (1964)

106. Beeler, J.R.: Radiation effects computer experiments. Defects in crystalline solids, vol. 13. North-Holland, Amsterdam (1983)

107. Verlet, L.: Computer experiments on classical fluids I. Thermodynamical properties of Lennard-Jones molecules. Phys Rev **159**, 98-103 (1967)

108. Nordlund, K.: Molecular dynamics simulation of ion ranges in the 1-100 keV energy range. Comp Mater Sci **3**, 448-456 (1995)

109. Lennard-Jones, J.E.: On the forces between atoms and ions. P R Soc Lond A **109**, 584-597 (1925)

110. Morse, P.M.: Diatomic molecules according to the wave mechanics I: Electronic levels of the hydrogen molecular ion. Phys Rev **33**, 932-947 (1929)

111. Daw, M.S., Baskes, M.I.: Embedded-atom method - derivation and application to impurities, surfaces, and other defects in metals. Phys Rev B **29**, 6443-6453 (1984)

112. Daw, M.S., Foiles, S.M., Baskes, M.I.: The Embedded-atom method - a review of theory and applications. Mater Sci Rep **9**, 251-310 (1993)

113. Finnis, M.W., Sinclair, J.E.: A simple empirical n-body potential for transition-metals. Philos Mag A **50**, 45-55 (1984)

114. Ackland, G.J., Thetford, R.: An improved n-body semiempirical model for body-centered cubic transition-metals. Philos Mag A **56**, 15-30 (1987)

115. Stillinger, F.H., Weber, T.A.: Computer-simulation of local order in condensed phases of silicon. Phys Rev B **3**, 5262-5271 (1985)

116. Tersoff, J.: Empirical interatomic potential for carbon, with applications to amorphous-carbon. Phys Rev Lett **61**, 2879-2882 (1988)

117. Tersoff, J.: Empirical interatomic potential for silicon with improved elastic properties. Phys Rev B **38**, 9902-9905 (1988)

118. Tersoff, J.: Modeling solid-state chemistry - interatomic potentials for multicomponent systems. Phys Rev B **39**, 5566-5568 (1989)

119. Brenner, D.W.: Empirical potential for hydrocarbons for use in simulating the chemical vapor-deposition of diamond films. Phys Rev B **42**, 9458-9471 (1990)

120. Erhart, P., Juslin, N., Goy, O., Nordlund, K., Müller, R., Albe, K.: Analytic bond-order potential for atomistic simulations of zinc oxide. J Phys-Condens Mat **18**, 6585-6605 (2006)

121. Uberuaga, B.P., Smith, R., Cleave, A.R., Montalenti, F., Henkelman, G., Grimes, R.W., Voter, A.F., Sickafus, K.E.: Structure and mobility of defects formed from collision cascades in MgO. Phys Rev Lett **92**, 115505 (2004)

122. Hallil, A., Tetot, R., Berthier, F., Braems, I., Creuze, J.: Use of a variable-charge interatomic potential for atomistic simulations of bulk, oxygen vacancies, and surfaces of rutile TiO2. Phys Rev B **73**, 165406 (2006)

123. Srivastava, D., Garrison, B.J., Brenner, D.W.: Anisotropic spread of surface dimer openings in the initial stages of the epitaxial growth of Si on Si(100). Phys Rev Lett **63**, 302-305 (1989)

124. Berendsen, H.J.C., Postma, J.P.M., Vangunsteren, W.F., Dinola, A., Haak, J.R.: Molecular-dynamics with coupling to an external Bath. J Chem Phys **81**, 3684-3690 (1984)

125. Schiøtt, H.E.: Range-energy relations for low-energy ions. Matematisk-fysiske Meddelelser, vol. **35**,9 (1966)

126. Weissmann, R., Sigmund, P.: Sputtering and backscattering of keV light ions bombarding random targets. Radiation Effects **19**, 7-14 (1973)

127. Littmark, U., Ziegler, J.F.: Handbook of range distributions for energetic ions in all elements. The stopping and ranges of ions in matter, vol. 6. Pergamon Press, New York (1980)

128. Biersack, J.P.: Calculation of projected ranges - analytical solutions and a simple general algorithm. Nucl Instrum Methods **182**, 199-206 (1981)

129. Raineri, V., Privitera, V., Galvagno, G., Priolo, F., Rimini, E.: Channeling implants in silicon-crystals. Mater Chem Phys **38**, 105-130 (1994)

130. Posselt, M., Schmidt, B., Feudel, T., Strecker, N.: Atomistic simulation of ion implantation and its application in Si technology. Mat Sci Eng B-Solid **71**, 128-136 (2000)

131. Yang, S.H., Morris, S.J., Tian, S.Y., Parab, K.B., Tasch, A.F.: Monte Carlo simulation of arsenic ion implantation in (100) single-crystal silicon. IEEE T Semiconduct M **9**, 49-58 (1996)

132. Möller, W., Eckstein, W.: Effects of target crystallinity on the range distribution of hydrogen ions in metals. Nuclear Instruments & Methods in Physics Research **194**, 121-124 (1982)

133. Posselt, M., Heinig, K.H.: Comparison of BC-simulations and MD-simulations of low-energy ion-implantation. Nucl Instrum Meth B **102**, 236-241 (1995)

134. Nordlund, K., Kuronen, A.: Molecular dynamics simulation of ion ranges at keV energies. Nucl Instrum Meth B **115**, 528-531 (1996)

135. Hobler, G., Betz, G.: On the useful range of application of molecular dynamics simulations in the recoil interaction approximation. Nucl Instrum Meth B **180**, 203-208 (2001)

136. Gärtner, K., Stock, D., Weber, B., Betz, G., Hautala, M., Hobler, G., Hou, M., Sarite, S., Eckstein, W., Jimenez-Rodriguez, J.J., Perez-Martin, A.M.C., Andribet, E.P., Konoplev, V., Gras-Marti, A., Posselt, M., Shapiro, M.H., Tombrello, T.A., Urbassek, H.M., Hensel, H., Yamamura, Y., Takeuchi, W.: Round-Robin Computer-simulation of ion transmission through crystalline layers. Nucl Instrum Meth B **102**, 183-197 (1995)

137. Sigmund, P., Matthies, M.T., Phillips, D.L.: Energy deposition and penetration depth of heavy ions in the electronic stopping region. Radiation Effects **11**, 39-49 (1971)

138. Winterbon, K.B.: Calculations of implanted-ion range and energy-deposition distributions - B-11 in Si. Radiat Eff Defect S **30**, 199-206 (1976)

139. Hou, M., Pan, Z.Y.: Cascade statistics in the binary collision approximation and in full molecular-dynamics. Nucl Instrum Meth B **102**, 93-102 (1995)

140. Sigmund, P.: Energy density and time constant of heavy-Ion induced elastic-collision spikes in solids. Appl Phys Lett **25**, 169-171 (1974)

141. Sigmund, P., Claussen, C.: Sputtering from elastic-collision spikes in heavy-ion-bombarded metals. J Appl Phys **52**, 990-993 (1981)

142. Toulemonde, M., Dufour, C., Meftah, A., Paumier, E.: Transient thermal processes in heavy ion irradiation of crystalline inorganic insulators. Nucl Instrum Meth B **166**, 903-912 (2000)

143. Meftah, A., Costantini, J.M., Khalfaoui, N., Boudjadar, S., Stoquert, J.P., Studer, F., Toulemonde, M.: Experimental determination of track cross-section in Gd3Ga5O12 and comparison to the inelastic thermal spike model applied to several materials. Nucl Instrum Meth B **237**, 563-574 (2005)

144. Gervais, B., Bouffard, S.: Simulation of the primary stage of the interaction of swift heavy ions with condensed matter. Nucl Instrum Meth B **88**, 355-364 (1994)

145. Waligorski, M.P.R., Hamm, R.N., Katz, R.: The radial distribution of dose around the path of a heavy ion in liquid water. Nucl Tracks Rad Meas **11**, 309-319 (1986)

146. Sigmund, P. (ed.): Fundamental processes in sputtering of atoms and molecules (SPUT92). Matematisk-fysiske Meddelelser vol. 43 (1993)

147. Sigmund, P.: Sputtering by ion bombardment: Theoretical concepts. In: Behrisch, R. (ed.) Physical sputtering of single-element solids. Sputtering by Particle Bombardment, vol. 1. Springer, Berlin (1981)

148. Thompson, M.W.: Energy spectrum of ejected atoms during high energy sputtering of gold. Philos Mag **18**, 377-414 (1968)

149. Bohdansky, J.: A universal relation for the sputtering yield of monatomic solids at normal ion incidence. Nucl Instrum Meth B **2**, 587-591 (1984)

150. Eckstein, W.: Sputtering yields. In: Behrisch, R., Eckstein, W. (eds.) Sputtering by particle bombardment: experiments and computer calculations from threshold to MeV energies. Topics in applied physics, vol. 110. Springer, Berlin (2007)

151. Eckstein, W., Garcia-Rosales, C., Roth, J., Ottenberger, W.: Sputtering data. Report IPP **9**(82), Max-Planck Institute of Plasma Physics, Garching (1993)

152. Yamamura, Y., Tawara, H.: Energy dependence of ion-induced sputtering yields from monatomic solids at normal incidence. Atom Data Nucl Data **62**, 149-253 (1996)

153. Betz, G., Kirchner, R., Husinsky, W., Rudenauer, F., Urbassek, H.M.: Molecular-dynamics study of sputtering of Cu(111) under Ar ion-bombardment. Radiat Eff Defect S **130**, 251-266 (1994)

154. Urbassek, H.M.: Sputter theory. In: Sigmund, P. (ed.) Ion beam science: solved and unsolved problems Pt. 2. Matematisk-fysiske Meddelelser, vol. 52,2 (2006)

155. Urbassek, H.M.: Results of molecular dynamics calculations. In: Behrisch, R., Eckstein, W. (eds.) Sputtering by particle bombardment: experiments and computer calculations from threshold to MeV energies. Topics in applied physics, vol. 110. Springer, Berlin (2007)

156. Harrison, D.E., Kelly, P.W., Garrison, B.J., Winograd, N.: Low-energy ion impact phenomena on single-crystal surfaces. Surf Sci **76**, 311-322 (1978)

157. Smith, R., Harrison, D.E., Garrison, B.J.: keV particle bombardment of semiconductors - a molecular-dynamics simulation. Phys Rev B **40**, 93-101 (1989).

158. Wehner, G.K.: Controlled sputtering of metals by low-energy Hg ions. Phys Rev **102**, 690-704 (1956)

159. Andersen, H.H., Bay, H.L.: Nonlinear effects in heavy-ion sputtering. J Appl Phys **45**, 953-954 (1974)

160. Andersen, H.H., Bay, H.L.: Heavy-ion sputtering yields of gold - further evidence of nonlinear effects. J Appl Phys **46**, 2416-2422 (1975)

161. Andersen, H.H., Brunelle, A., Della-Negra, S., Depauw, J., Jacquet, D., Le Beyec, Y., Chaumont, J., Bernas, H.: Giant metal sputtering yields induced by 20-5000 keV atom gold clusters. Phys Rev Lett **80**, 5433-5436 (1998)

162. Assmann, W., Toulemonde, M., Trautmann, C.: Electronic sputtering with swift heavy ions. In: Behrisch, R., Eckstein, W. (eds.) Sputtering by particle bombardment: experiments and computer

calculations from threshold to MeV energies. Topics in applied physics, vol. 110. Springer, Berlin (2007)

163. Toulemonde, M., Assmann, W., Trautmann, C., Gruner, F., Mieskes, H.D., Kucal, H., Wang, Z.G.: Electronic sputtering of metals and insulators by swift heavy ions. Nucl Instrum Meth B **212**, 346-357 (2003)

164. Toulemonde, M., Assmann, W., Trautmann, C., Gruner, F.: Jetlike component in sputtering of LiF induced by swift heavy ions. Phys Rev Lett **88**, 057602 (2002)

165. Arnoldbik, W.M., Tomozeiu, N., Habraken, F.H.P.M.: Electronic sputtering of thin SiO2 films by MeV heavy ions. Nucl Instrum Meth B **203**, 151-157 (2003)

166. Schou, J.: Sputtering of frozen gases. Nucl Instrum Meth B **27**, 188-200 (1987)

167. Bringa, E.M., Nordlund, K., Keinonen, J.: Cratering-energy regimes: From linear collision cascades to heat spikes to macroscopic impacts. Phys Rev B **64**, 235426 (2001)

168. Mookerjee, S., Beuve, M., Khan, S.A., Toulemonde, M., Roy, A.: Sensitivity of ion-induced sputtering to the radial distribution of energy transfers: A molecular dynamics study. Phys Rev B **78**, 045435 (2008)

169. Betz, G., Wehner, G.K.: Sputtering of multicomponent materials. In: Behrisch, R. (ed.) Sputtering of alloys and compounds, electron and neutron sputtering, surface topography. Sputtering by Particle Bombardment, vol. 2. Springer, Berlin (1983)

170. Andersen, H.H.: Ion-bombardmend induced composition changes in alloys and compounds. In: Williams, J.S., Poate, J.M. (eds.) Ion implantation and beam processing. Acad. Press, Sydney (1984)

171. Sigmund, P., Lam, N.Q.: Alloy and isotope sputtering. In: Sigmund, P. (ed.) Fundamental processes in sputtering of atoms and molecules (SPUT92). Matematisk-fysiske Meddelelser, vol. 43 (1993)

172. Baretzky, B., Möller, W., Taglauer, E.: Collisional processes in preferential sputtering of tantalum oxide. Nucl Instrum Meth B **18**, 496-500 (1987)

173. Baretzky, B., Möller, W., Taglauer, E.: Collision dominated preferential sputtering of tantalum oxide. Vacuum **43**, 1207-1216 (1992)

174. Kelly, R.: On the problem of whether mass or chemical bonding is more important to bombardment-induced compositional changes in alloys and oxides. Surf Sci **100**, 85-107 (1980)

175. Averback, R.S., de la Rubia, T.D.: Displacement damage in irradiated metals and semiconductors. Solid State Phys **51**, 281-402 (1998)

176. Mazzoldi, P., Arnold, G.W.: Ion beam modification of insulators. Beam modification of materials, vol. 2. Elsevier, Amsterdam (1987)

177. Itoh, N., Stoneham, A.M.: Materials modification by electronic excitation. Cambridge University Press, Cambridge (2001)

178. Kinchin, G.H., Pease, R.S.: The displacement of atoms in solids by radiation. Rep Prog Phys **18**, 1-51 (1955)

179. Jung, P., Chaplin, R.L., Fenzl, H.J., Reichelt, K., Wombache.P: Anisotropy of threshold energy for production of Frenkel pairs in copper and platinum. Phys Rev B **8**, 553-561 (1973)

180. Averback, R.S., Benedek, R., Merkle, K.L.: Efficiency of defect production in cascades. J Nucl Mater **69-70**, 786-789 (1978)

181. Bernas, H., Traverse, A.: Atomic displacements in metals due to low-energy light-ion implantation. Appl Phys Lett **41**, 245-246 (1982)

182. Kögler, R., Ou, X., Skorupa, W., Möller, W.: The origin of the energy-dose window in separation-by-implanted-oxygen materials processing. Appl Phys Lett **92**, 181906 (2008)

183. Agarwal, A., Christensen, K., Venables, D., Maher, D.M., Rozgonyi, G.A.: Oxygen gettering and precipitation at MeV Si+ ion implantation induced damage in silicon. Appl Phys Lett **69**, 3899-3901 (1996)

184. Averback, R.S.: Ion-Irradiation Studies of Cascade Damage in Metals. J Nucl Mater **108**, 33-45 (1982)

185. Dunlop, A., Lesueur, D., Legrand, P., Dammak, H.: Effects induced by high electronic excitations in pure metals - a detailed study in iron. Nucl Instrum Meth B **90**, 330-338 (1994)

186. Dufour, C., Wang, Z.G., Paumier, E., Toulemonde, M.: Transient thermal process induced by swift heavy ions: Defect annealing and defect creation in Fe and Ni. B Mater Sci **22**, 671-677 (1999)

187. Fleischer, R.L., Price, P.B., Walker, R.M.: Nuclear tracks in solids. Principles and applications. Univ. of California Press, Berkeley (1975)

188. Toulemonde, M., Assmann, W., Dufour, C., Meftah, A., Studer, F., Trautmann, C.: Experimental phenomena and thermal spike model description of ion tracks in amorphisable inorganic insulators. In: Sigmund, P. (ed.) Ion beam science: solved and unsolved problems Pt. 1, Matematisk-fysiske Meddelelser, vol. 52,1 (2006)

189. Klaumunzer, S.: Thermal-spike models for ion track physics. A critical examination. In: Sigmund, P. (ed.) Ion beam science: solved and unsolved problems Pt. 1. Matematisk-fysiske Meddelelser, vol. 52,1 (2006)

190. Toulemonde, M., Weber, W.J., Li, G.S., Shutthanandan, V., Kluth, P., Yang, T.F., Wang, Y.G., Zhang, Y.W.: Synergy of nuclear and electronic energy losses in ion-irradiation processes: The case of vitreous silicon dioxide. Phys Rev B **83**, 054106 (2011)

191. Szenes, G.: General features of latent track formation in magnetic insulators irradiated with swift heavy-ions. Phys Rev B **51**, 8026-8029 (1995)

192. Szenes, G.: Thermal spike analysis of ion-induced tracks in semiconductors. Nucl Instrum Meth B **269**, 2075-2079 (2011)

193. Ghaly, M., Averback, R.S.: Effect of viscous flow on ion damage near solid surfaces. Phys Rev Lett **72**, 364-367 (1994)

194. Brinkman, J.A.: On the nature of radiation damage in metals. J Appl Phys **25**, 961-970 (1954)

195. Williams, J.S., de M. Azevedo, G., Bernas, H., Fortuna, F.: Ion-beam-induced amorphization and epitaxial crystalliazation of silicon. In: Bernas, H. (ed.) Materials science with ion beams. Topics in applied physics, vol. 116. Springer, Berlin (2010)

196. Cheng, Y.-T.: Thermodynamic and fractal geometric aspects of ion-solid interactions. Mater Sci Rep **5**, 45-97 (1990)

197. Nastasi, M., Mayer, J.W.: Ion-beam mixing in metallic and semiconductor-materials. Mat Sci Eng R **12**, 1-52 (1994)

198. Bolse, W.: Mechanisms of ion beam induced atomic mixing in solids. Mat Sci Eng A-Struct **253**, 194-201 (1998)

199. Sigmund, P., Gras-Marti, A.: Theoretical aspects of atomic mixing by ion beams. Nucl Instrum Methods **182**, 25-41 (1981)

200. Möller, W., Eckstein, W.: Ion mixing and recoil implantation simulations by means of TRIDYN. Nucl Instrum Meth B **7-8**, 645-649 (1985)

201. Fassbender, J., von Borany, J., Mücklich, A., Potzger, K., Möller, W., McCord, J., Schultz, L., Mattheis, R.: Structural and magnetic modifications of Cr-implanted Permalloy. Phys Rev B **73**, 184410 (2006)

202. Fassbender, J., Mücklich, A., Potzger, K., Möller, W.: Mixing and subsequent amorphization of ultrathin Ni81Fe19/Ta bilayers by 30 keV Ni implantation. Nucl Instrum Meth B **248**, 343-346 (2006)

203. Bracht, H., Radek, M., Kube, R., Knebel, S., Posselt, M., Schmidt, B., Haller, E.E., Bougeard, D.: Ion-beam mixing in crystalline and amorphous germanium isotope multilayers. J Appl Phys **110**, 093502 (2011)

204. Cheng, Y.T., Vanrossum, M., Nicolet, M.A., Johnson, W.L.: Influence of chemical driving forces in ion mixing of metallic bilayers. Appl Phys Lett **45**, 185-187 (1984)

205. Van Rossum, M., Cheng, Y.T., Nicolet, M.A., Johnson, W.L.: Correlation between cohesive energy and mixing rate in ion mixing of metallic bilayers. Appl Phys Lett **46**, 610-612 (1985)

206. Johnson, W.L., Cheng, Y.T., Van Rossum, M., Nicolet, M.A.: When is thermodynamics relevant to ion-induced atomic rearrangements in metals. Nucl Instrum Meth B **7-8**, 657-665 (1985)

207. Leguay, R., Dunlop, A., Dunstetter, F., Lorenzelli, N., Braslau, A., Bridou, F., Corno, J., Pardo, B., Chevallier, J., Colliex, C., Menelle, A., Rouviere, J.L., Thome, L.: Evidence for atomic mixing induced in metallic bilayers by electronic energy deposition. Nucl Instrum Meth B **122**, 481-502 (1997)

208. Wang, Z.G., Dufour, C., Euphrasie, S., Toulemonde, M.: Electronic thermal spike effects in intermixing of bilayers induced by swift heavy ions. Nucl Instrum Meth B **209**, 194-199 (2003)

209. Bolse, W.: Interface modification by swift heavy ions. Radiat Meas **36**, 597-603 (2003)

HZDR
HELMHOLTZ
ZENTRUM DRESDEN
ROSSENDORF

Bautzner Landstraße 400
01328 Dresden, Germany
Tel. +49 351 260-2245
Fax +49 351 260-12245
w.moeller@hzdr.de
http://www.hzdr.de